DOCTORAL THESIS

INDIAN INSTITUTE OF TECHNOLOGY GUWAHATI

Development of a Laser Scanning Confocal Microscope with Programmably Switchable Vector Beam Illumination

Thesis submitted in partial fulfillment of the requirements for the degree of

Doctor of Philosophy

of the

Indian Institute of Technology Guwahati.

by

Ranjan Kalita

Thesis Supervisor: **Prof. Bosanta R. Boruah**

Optical Imaging Laboratory, Department of Physics,
Indian Institute of Technology Guwahati,
Guwahati-781039, Assam, India.

2020

Dedicated To My Beloved Family

Declaration

Mr Ranjan Kalita
Roll No.: 146121029
Department of Physics,
Indian Institute of Technology Guwahati,
Guwahati-781039, Assam, India.
E-mail: ranjan.kalita@iitg.ac.in

I hereby declare that the results embodied in this thesis is the result of experiments carried out by me at the Department of Physics, Indian Institute of Technology Guwahati, Guwahati, India under the supervision of Prof Bosanta Ranjan Boruah. This thesis has not been submitted to any university/ institute or elsewhere for the award of any degree, diploma or associateship.

Ranjan Kalita

Date:

Certificate

Prof Bosanta Ranjan Boruah
Department of Physics,
Indian Institute of Technology Guwahati,
Guwahati-781039, Assam, India.
Phone: (+91) 361-258-2725 (O)
E-mail: brboruah@iitg.ac.in

This is to certify that the work contained in the thesis entitled **'Development of a Laser Scanning Confocal Microscope with Programmably Switchable Vector Beam Illumination'** by **Ranjan Kalita** (Roll No. 146121029), a student of Department of Physics, Indian Institute of Technology Guwahati, for the award of degree of Doctor of Philosophy, has been carried out under my supervision.

The present thesis or any part thereof has not been submitted elsewhere for award of any other degree, diploma or associateship.

Bosanta R. Boruah

Date:

Acknowledgments

First and foremost, I would like to express my deepest gratitude to my thesis supervisor Prof. Bosanta R. Boruah, for his continuous guidance and motivation throughout my Ph.D. work. His valuable suggestions helped me a better understanding of the research topic and in sorting out each of the technical issues faced while performing the experiments.

My gratitude also goes to my Doctoral committee members: Dr. Ashwini Kumar Sarma (Chairman), Dr. Gagan Kumar, and Dr. A. S. Achalkumar for their valuable time and insightful remarks and suggestions at every point of time.

My sincere thanks to the former (during the tenure of my Ph.D.) and present HoDs of the Department of Physics, IIT Guwahati: Prof. Saurabh Basu, Prof. Poulose Poulose, and Prof. Subhradip Ghosh for providing me the opportunity to utilize different resources of the department to carry out my research work. I would also like to thank all the technical and administrative staff of the department who helped me in multiple ways during my Ph.D. period.

I gratefully acknowledge the Department of Science and Technology (DST), Government of India, and Ministry of Human Resource and Development (MHRD), Government of India, for providing me financial support during my Ph.D.

I take this opportunity to thank all the past, and present members of the optical imaging laboratory (OIL) and computer generated holography (CGH) laboratory: Dr. Abijit Das, Dr. Md. Gaffar, Dr. Biswajit Pathak, Dr. Santanu Konwar, S. S. Goutam Buddha, Karuna S. Malik, Nagendra Kumar, Akanshu Chauhan, and Needup Sherpa for the stimulating discussions, and for the quality time we had during the tenure of my Ph.D. work. Particularly I would like to acknowledge Goutam for his valuable help in developing the necessary electronics and microprocessor program to perform some of the experimental work.

I am fortunate enough to have a great friend circle in IIT Guwahati with whom I shared wonderful times that helps me the necessary distraction from stressful situations. I would also like to thank all my close friends for being with me in all the thicks and thins of my life.

Finally, I would like to thank my family members: my parents Mr. Baneswar Kalita and Mrs. Sashi Kalita, my brothers Dr. Abhijit Kalita and Mr. Nabajit Kalita, my sister-in-laws Mrs. Gayatri Borah Kalita and Mrs. Anjali Kalita, my

wife Mrs. Tarangini Sonowal Kalita; for their infallible love and constant concern about my well-being.

Abstract

The laser scanning confocal microscope (LSCM) is an important imaging tool for a wide range of investigations, particularly in biological and biomedical sciences, due to the ability of imaging thin slices of the specimen. Use of polarization profile of the illumination beam in an LSCM as one of the parameters can extract information such as on molecular organizations in the specimen, which is otherwise not possible. Many polarization measurements in LSCM require capturing images with more than one polarizations, for instance, with two orthogonal linear or circular polarizations in the case of linear dichroism. In such measurements, usually, the change in polarization takes place at the end of one complete image frame, which leads to a delay of at least equal to the acquisition time of one full-frame image, between the illuminations with two different polarizations. Such an amount of delay may create issues for applications, for instance, imaging specimens which are not static. Besides, some applications require special illumination beams such as cylindrical vector beams. Therefore, the polarization based applications of LSCM require the setup to be equipped with a robust mechanism to generate illumination beams with arbitrary polarization profiles. Further, the system requires to be capable of switching the illumination beam between different polarization profiles quickly. However, the conventional LSCMs do not have such mechanisms to generate and quickly switch between various user-defined polarization profiles of the illumination beam.

In this thesis, we propose a robust and flexible scheme using a single liquid crystal spatial light modulator (LCSLM) to generate arbitrary and user-defined vector beams with the highest average-power possible with an LCSLM based method. We carry out experiments to verify the working of the vector beam forming unit. We develop a galvanometer based laser scanning microscope employing the vector beam forming unit to design the illumination beam and introduce a scheme to switch the polarization of the illumination beam after every line scanned, in contrast to every full-frame image as in the conventional case. We implement polarization switching in both reflectance and fluorescence mode of the LSCM. We then introduce a holographic scanning confocal microscope working in both reflection and fluorescence modes that can provide better beam positioning accuracy than a galvanometer based setup. We also implement a polarization switching scheme in the holographic scanning confocal microscope.

Acronyms

ADC	-	Analog-to-digital conversion
AOI	-	Area of interest
CCD	-	Charge-coupled Device
CGH	-	Computer generated hologram
CMOS	-	Complementary metal oxide semiconductor
DAQ	-	Data acquisition
DBS	-	Dichroic beam splitter
DVI	-	Digital visual interface
FELCSLM	-	Ferroelectric liquid crystal spatial light modulator
FFT	-	Fast Fourier transform
fps	-	Frames per second
FWHM	-	Full width at half maximum
ID	-	Iris diaphragm
LC	-	Liquid crystal
LCSLM	-	Liquid crystal Spatial Light Modulator
LD	-	Linear dichroism
LSCM	-	Laser scanning confocal microscope
MO	-	Microscope objective
NA	-	Numerical aperture
NLCSLM	-	Nematic liquid crystal spatial light modulator
PC	-	Personal computer
PEM	-	Photoelastic modulator
PMT	-	Photomultiplier Tube
PSF	-	Point spread function
SLM	-	Spatial light modulator
SNR	-	Signal to noise ratio
SXGA	-	Super extended graphics array
TNLCSLM	-	Twisted-nematic liquid crystal spatial light modulator
TTL	-	Transistor-transistor logic
USB	-	Universal serial bus
WUXGA	-	Widescreen ultra extended graphics array
WXGA	-	Wide extended graphics array

Contents

List of Figures

List of Tables

Chapter 1

General introduction and thesis overview

1.1 General Introduction

Over the decades, the laser scanning confocal microscope (LSCM) has become a powerful imaging tool to obtain high contrast optically sectioned images. The optical sectioning property is achieved by keeping a pinhole at a plane conjugate to the illumination spot in the specimen plane to obstruct the out of focus light from the volume of a thick specimen [1, 2, 3]. One may also capture images of a large number of thin slices of a thick specimen to build an impressive three-dimensional view of the specimen, using a confocal microscope. The ability of the confocal microscope in the fluorescence mode to image deep inside the tissue in a noninvasive manner has made the microscope extremely popular for biological applications, such as fluorescence imaging of living cells and tissues [4, 5]. Owing to enhanced imaging capabilities, the LSCM finds applications in diverse areas such as the precise diagnosis of brain tumor [6], real-time imaging of retina [7, 8], the studies of crystal morphology [9], study of material deformation [10], studies of food product quality [11, 12], and so on.

The polarization property of the illumination beam is often exploited in optical microscopy to extract additional information on molecular organization in the specimen. This relies on the fact that, upon illuminating the specimen, the excitation or absorption efficiency of the molecules depends on the angle between the molecular dipole moment and the excitation electric field [13]. Thus the amount of fluorescence from a molecule varies based on this angle, and the same gives an indication of the molecular orientation relative to the excitation field. On the other hand, when a light beam is focused by a lens, the electric field orientation at the focus directly depends on the polarization profile of the beam at the entrance pupil of the lens

[14, 15]. Therefore, in a confocal microscope, the orientation of the electric field that excites the molecules in the specimen can be controlled by modifying the polarization profile of the illumination beam at the entrance pupil of the microscope objective (MO) lens. Polarization based microscopy has found applications in the studies of structures of biological macromolecules [16], fiber orientation of ocular tissues [17], protein structures and functions [18], exciton fine structure of nanocrystals [19], properties of fluorescent nanoemitters [20], topological defects in liquid crystal materials [21], and so on. In general, the polarization based measurements involve capturing at least two images of the specimen using illumination beams with orthogonal polarizations. The difference of the two images yields a two-dimensional mapping of the anisotropic optical organization of molecules in the specimen. Therefore, for a complete exploration of the three-dimensional spatial orientation of the molecules, one needs to image the specimen with three mutually orthogonally polarized illumination beam. Thus the polarization microscopy based studies require a mechanism to switch the illumination beam between different polarization states of the illumination beam at the entrance pupil, many such polarization profiles may be non conventional.

In the last few decades, several techniques have been proposed to modulate the polarization of the illumination beam in an optical microscope. Many of these techniques use an electro-optic modulator such as Pockels cell [22, 23, 24], or magneto-optic modulator such as Faraday rotator [25] to modulate the polarization of the illumination beam using different classical polarization states, which are plane polarized, circularly polarized, and elliptically polarized. A universal compensator made up of liquid crystal (LC) variable retarders [26, 27, 28, 29] can be used to produce a two-dimensional spatial distribution of polarization of the illumination beam. However, in a microscope, employing the above mentioned methods, the polarization modulation of the illumination beam occurs only at the end of the acquisition of one complete image frame. This technique thus leads to a delay equal to at least the acquisition time of one complete image frame, between the imagings with two different polarizations. Such kind of delay may create an issue while imaging a specimen which is in a dynamic environment. There are only a few techniques that enable to switch the polarization of the illumination beam in a microscope after every line scanned [23, 30, 31], where polarization modulation is achieved by using Pockels cell or photoelastic modulators (PEM). But the techniques can generate and alter the polarization of the illumination beam among the classical polarization states only.

The programmability of a liquid crystal spatial light modulator (LCSLM) can be utilized to generate a user-defined two-dimensional spatial polarization profile in a light beam, called an arbitrary vector beam. The LCSLM based techniques uses two [32] or three LCSLMs [33], or one LCSLM along with a Wollaston prism [34, 35], or double pass beam through a single LCSLM [36], to achieve the dynamic control over the vector beam. However, until now, in a microscope that uses LCSLM based scheme to modulate the polarization profile of the illumination beam employs the switching of polarization of the illumination beam after every image frame only.

The LCSLM based vector beam forming schemes usually involve two successive incidences on one or two LCSLM display panels [32, 33, 36]. Thus the incident beam undergoes two diffraction losses after each incidence on the LCSLM. The energy in the final vector beam is thus decided by the maximum power of the beam that corresponds to the first incidence. However, all commercial LCSLMs have a fixed damage threshold in so far as the incident power is concerned [37]. Therefore the maximum power of the vector beam generated using an LCSLM based scheme is limited by the damage threshold of the device. Such scheme if employed in a confocal microscope will not be suitable for applications needing a high power vector beam to illuminate the specimen.

Usually to capture the full-frame image of the specimen, the confocal microscope uses a galvanometer mirror scanner to scan the laser beam all over the imaging area in a raster fashion [38]. However, high-speed operation of such scanners can lead to temperature variations [39], thereby affecting the stability and accuracy of the scanner [40]. These issues may affect applications, especially those involving weak signals from the specimen [41], thereby requiring long time acquisition [42] or those involving a time-lapsed study of the specimen [43].

Considering the above mentioned issues, the present thesis discusses the development of a division of wavefront-based LCSLM assembly for the generation of an arbitrary and user-defined vector beam. The generation of the desired arbitrary vector beam is a result of the coherent addition of two orthogonally polarized beams. The two said beams are generated using computer generated holograms (CGH) in such a way that the complex amplitude profiles of the beams represent the two orthogonally polarized pupil planes corresponding to the desired vector beam. The proposed setup has an additional advantage in terms of the generation of higher average-power vector beams.

This thesis proposes a laser scanning confocal microscope using the LCSLM

based arbitrary vector beam forming unit in conjunction with a galvanometer based scanning unit, a detector unit, and a microprocessor baser synchronization unit. The LCSLM assembly, along with other units, facilitates intraframe polarization switching; that is, the illumination beam polarization profile is switched at the end of each line scanned, thereby considerably reducing the time in illuminating a particular portion of the specimen with two different polarizations. We propose a few schemes depending on the number of different illumination beam polarization to be generated and the switching manner of the polarization profile to scan the specimen.

We then further develop the proposed microscope capable of intraframe polarization switching of the illumination beam to achieve imaging using fluorescence light. A hologram written on a liquid crystal spatial light modulator can act as a programmable diffraction grating [44, 45, 46] to achieve beam steering with superior stability and repeatability. In this thesis, such a computer generated hologram based beam scanning scheme is exploited to implement a scanning microscope that works in both the reflection and fluorescence mode that provides superior beam repeatability relative to galvanometer based scanning. We also implement programmable polarization switching of the illumination beam in such a holographic scanning confocal microscope working in the fluorescence mode.

1.2 Thesis overview

Below, a chapter-wise overview of the thesis is provided.

Chapter 2 gives a brief description of the principle and operation of the laser scanning confocal microscope. The importance of the polarization profile of the illumination beam in an optical microscope is also discussed. A few polarization based microscopy techniques relevant to the thesis work is included followed by discussion on some limitations of present polarization based microscopy techniques. It then provides a detail description of the important hardware components required to build a basic laser scanning microscope for the purpose of the experimental work related to the thesis.

Chapter 3 introduces computer generated holography and discusses the optical properties of the liquid crystal spatial light modulator which are used to implement computer generated holograms. The basic operations of two LCSLMs relevant to the thesis work are explained followed by an elaboration on the design of CGH to

generate a beam with user-defined complex amplitude profile. Finally, the chapter describes the implementation of CGH in an optical arrangement to generate an arbitrary vector beam.

Chapter 4 introduces the division of wavefront-based scheme using a single LC-SLM to generate an arbitrary vector beam. The working of the proposed scheme is confirmed by generating a few important vector beams. The chapter also describes the displacement theorem and demonstrates its successful implementation to record the three-dimensional focal volume intensity distribution of vector beams without the use of any translation stage. The experimental results are presented to validate the additional capability of the vector beam forming scheme to have precise control over the phase profile of the beam.

In chapter 5, the proposed laser scanning confocal microscope comprising the division of wavefront-based vector beam forming unit as the illumination beam generation assembly is introduced . We briefly explain three schemes for intraframe polarization switching depending on the number of polarized profiles and the switching manner of the polarization profile to scan the specimen. The polarization switching of the illumination beam is achieved at the end of each line scanned. We conclude the chapter presenting a proof of principle experiment to demonstrate the working of the proposed microscope in the reflection mode utilizing two of the schemes to switch the polarization of the illumination beam after each line scanned.

Chapter 6 presents the implementation of the proposed intraframe polarization switching in the confocal microscope working in the fluorescence mode. A proof of principle experiment is presented to demonstrate the capability of the microscope in polarization switching of the illumination beam among different user-defined scalar and vector beams. The chapter then presents the implementation of a holographic scanning confocal microscope in the reflection as well as in the fluorescence mode. Programmable polarization switching of the illumination beam is also achieved in the holographic scanning microscope to demonstrate how the issue of wobble in the galvo scan mirrors can be addressed, for applications involving polarization measurements.

Chapter 7 summaries the thesis along with a discussion on some future prospects of thesis work.

* * *

Chapter 2

Laser scanning confocal microscopy and the role of polarization

2.1 Introduction

This thesis concerns the development of a laser scanning confocal microscope facilitating polarization switching of the illumination beam. Therefore the present chapter begins with a brief description of the basic principle and the operation of a laser scanning confocal microscope. Then the chapter discusses the importance and the use of polarization of the illumination beam in an optical microscope. A differential polarization laser scanning microscopy and cylindrical vector beam based microscopy, relevant to the thesis work, are also described. The chapter is concluded with a description of some of the essential components used in the experimental work related to the thesis.

2.2 Basic principle of laser scanning confocal microscope

Marvin Minsky pioneered the concept of confocal microscopy in a patent [47] filed in 1957. In Minsky's embodiment of the confocal microscope, a pinhole is used for producing a point source of light. The image of the point source is projected onto the specimen to illuminate a small patch in the specimen. A second pinhole is used in the detector plane placed confocally to the illumination spot in the specimen plane to restrict the out of focus light from the specimen volume. Minsky placed the specimen on a stage to perform the scanning under the static illumination point.

The principle of imaging the specimen using a point detector is later incorporated in a laser illumination scanning optical microscope by Davidovits and Egger [48] in 1969.

In the last few decades, there is a growing popularity on the use of a laser scanning microscope based on the confocal principle, commonly known as laser scanning confocal microscope. The confocal principle offers the ability to create a sharp image of a thin cross-section of the specimen volume [1, 2], referred to as the optically sectioned image of the specimen. Also, there is a marginal enhancement in the lateral resolution compared to that of a wide-field microscope. Below, the role of the pinhole to achieve the optical sectioning property and marginal improvement in lateral resolution, in a confocal microscope, is briefly discussed.

The use of the pinhole to reject light coming from out of focus planes in the specimen is illustrated in figure 2.1(a). Here, we showed the principle of optical sectioning property in case of an epi-illumination mode (where a single lens is used to illuminate the specimen and also to collect the light coming from the specimen) confocal microscope. The pinhole obstructs light reaching the detector coming from points that are in the out of focus planes. As an example, light from point S' and S'' indicated by the dashed-line and the solid-line in red are mostly blocked by the pinhole as shown in figure 2.1(a), whereas, light from the point S (indicated by solid-line in green) located in the focal plane is allowed to pass completely towards the detector. In addition, the pinhole also rejects light coming from off-axis points such as S' and S'' as shown in figure 2.1(b). A laser as the illumination source allows additional advantage in illuminating a tiny diffraction-limited volume of the specimen, where the confocal signal falls off extremely sharply for planes away from the in-focus confocal plane.

Wilson and Sheppard (1984) provided the necessary theory to describe the performance of a confocal system. The response of an imaging system to a point source or point object is referred to as a point spread function (PSF). Depending on whether the field or intensity is used to measure the response, it is termed as amplitude PSF or intensity PSF. In case of a conventional confocal microscope in reflection or transmission mode, the intensity in the detector plane (considering a point detector) is given by the convolution of the amplitude in the specimen (t) and the product of the illumination PSF (h_1) with the detection PSF (h_2) such that

$$I = \left|(h_1 h_2) \circledast t\right|^2 , \tag{2.1}$$

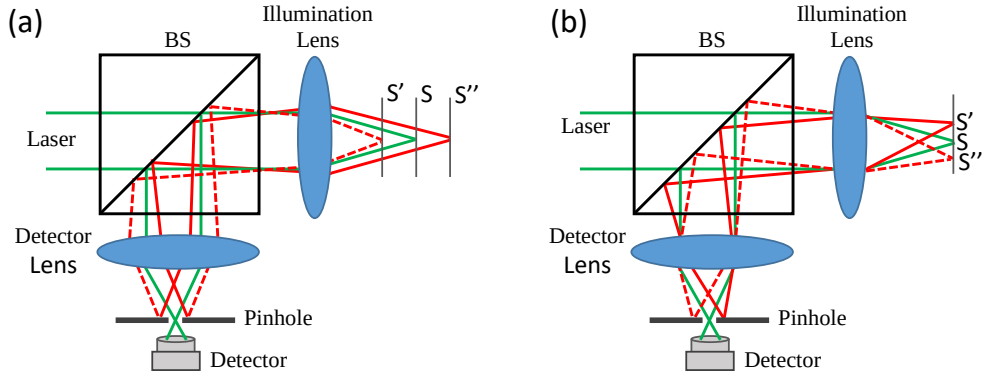

Figure 2.1: Illustratation of the role of pinhole to reject light from (a) points (S' and S'') in the out of focus planes, and (b) off-axis points (S' and S'') in the focal plane. The light from the point lying on the optical axis in the focal plane (S) is allowed by the pinhole to enter the detector.

where, $\circledast$ represents the convolution operation. If the illumination and detection lenses in a confocal microscope are identical and circular, then the intensity in the image plane due to a point object according to equation 2.1 is

$$I(v) = |h|^4 , \tag{2.2}$$

where we have $h_1 = h_2 = h$. Also $v = krn\sin(\alpha)$ is the normalized optical coordinate, $k = \frac{2\pi}{\lambda}$ is the wave number of the illumination light with wavelength λ, r is the radial coordinate in the detector plane, n is the reflective index of the medium around the specimen, and α is the angular semi-aperture of the lens. Using scalar diffraction theory [49] one can get the expression of $h = \left(\frac{2J_1(v)}{v}\right)$, so that

$$I(v) = \left(\frac{2J_1(v)}{v}\right)^4 , \tag{2.3}$$

where, J_1 represents the Bessel function of the first kind. The equation 2.3 therefore describes the PSF of the confocal microscope in the transverse direction. Similar expressions of the PSF can also be derived [50], in the axial direction and the same can be written as

$$I(u) = \left(\frac{\sin(u/4)}{(u/4)}\right)^4 , \tag{2.4}$$

where, $u = 4kzn\sin^2(\alpha/2)$ is the normalized axial optical coordinate with z as the axial distance.

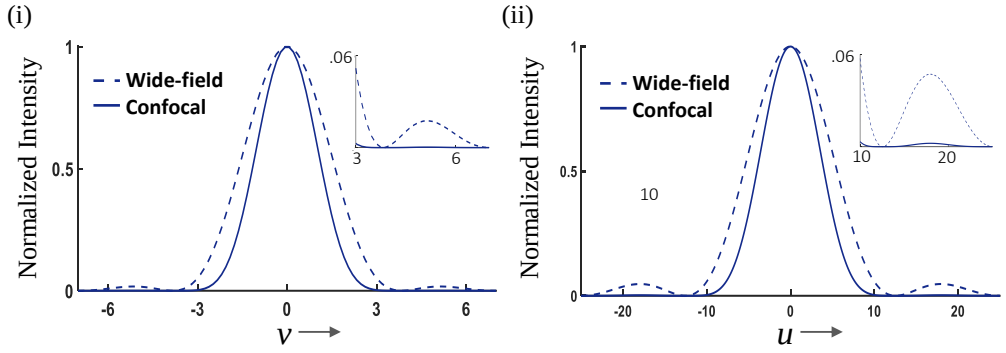

Figure 2.2: Plots of normalized intensity in the PSF due to a wide-field and a confocal microscope (a) in the transverse direction, (b) along the optical axis. The inset in each figure shows the zoomed version of the side-lobe on the right.

Therefore the two expressions $I(v)$ and $I(u)$ represent the confocal signal due to a point object when it is scanned laterally and axially, respectively. To be noted that in the case of a conventional wide-field microscope, the imaging equation similar to equation 2.1 is

$$I = |h \circledast t|^2 , \tag{2.5}$$

where h is the PSF of the wide-field microscope.

Figures 2.2(i) and 2.2(ii) show the normalized intensities along the transverse and axial directions, respectively, of the PSFs due to a conventional wide-field microscope as well as a confocal microscope. In case of a confocal microscope, it is found that the full width at half maxima ($v_{FWHM} = 2.32, u_{FWHM} = 8.02$) is narrower by a factor of about 1.4 [51] compared to that of a conventional wide-field microscope ($v_{FWHM} = 3.23, u_{FWHM} = 11.13$), accompanied by a noticeable reduction in the side-lobes [52] as indicated in the inset of the figures 2.2(i) and (ii). The narrower FWHM describes the marginal enhancement in the resolution achieved in the confocal microscope.

2.3 Laser scanning confocal setup

To image the desired area of the specimen, it is convenient to scan the illumination beam across the static specimen (a scheme commonly known as beam scanning) rather than moving the specimen (a scheme commonly known as stage scanning). The former technique has the advantage in terms of reducing scanning time and flexibility of the scanning process. The schematic diagram of a typical beam scanning LSCM working in epi-illumination mode is shown in figure 2.3. The beam from

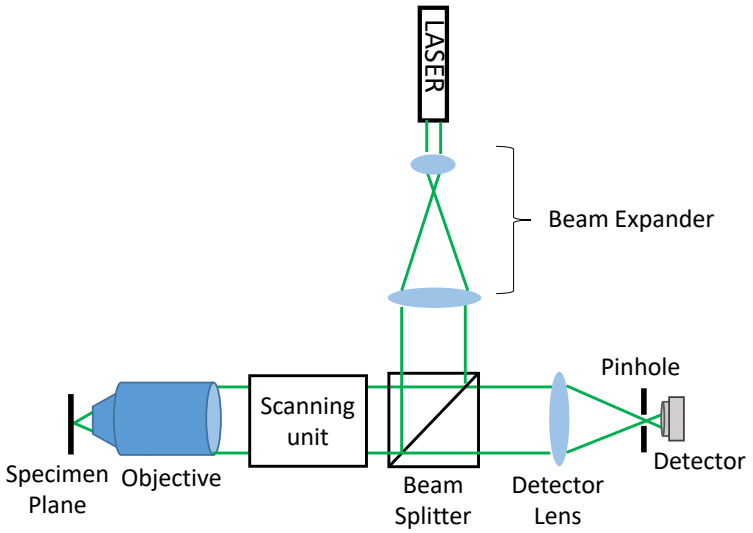

Figure 2.3: Schematic diagram of a typical beam scanning LSCM working in epi-illumination mode.

the laser source is expanded and collimated using a combination of lenses. The collimated laser beam is reflected by the beam splitter to be incident on the scanning unit. The beam after scanning enters the objective lens used to illuminate a tiny spot in the specimen. The beam splitter is either a 50:50 beam splitter for imaging in reflectance mode or a dichroic beam splitter (DBS) for imaging in fluorescence mode. The reflected or emitted fluorescence light from the specimen is collected by the same objective lens. The returned light is then de-scanned by the scanning unit before getting transmitted by the beam splitter to be incident on the detector lens. The detector lens focuses the reflected light onto the pinhole. The pinhole acts as the point detector by allowing the light mostly from the illumination point in the specimen plane to enter the detector. To position the pinhole optically conjugate to the illumination point in the specimen plane, a $4f$-relay unit is introduced in between the scanning unit and the objective lens. A $4f$ relay system comprising two lenses of focal length f image the plane P onto the plane P' as shown in figure 2.4, so that a pair of parallel rays within the segment MN in plane P also enters the segment $M'N'$ in plane P' as parallel rays, irrespective of the direction of the rays inside the relay system.

The fluorescence microscopy has emerged as an important tool in the biological and biomedical sciences. The phenomenon of fluorescence can be understood with the help of an energy level diagram introduced by Alexander Jablonski in 1930, known as the Jablonski diagram. When a molecule in the ground state absorbs a

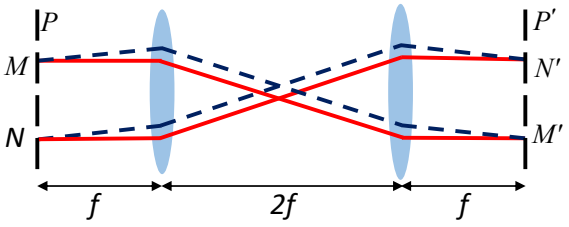

Figure 2.4: Illustration of a $4f$ relay system to image plane P onto the plane P'.

photon of the right energy, it gets excited electronically to a higher energy state (excited state). The molecule then relaxes vibrationally to a lower vibrational state and eventually undergoes spontaneous emission to one of the vibrational states of the lower energy ground state, as shown in figure 2.5(a). Fluorescence is the sum of such spontaneous emissions of light by a molecule, typically of longer wavelength than that of the light used for excitation. The transition to the excited state occurs very rapidly (10^{-15} s), whereas the vibrational relaxation occurs in picosecond time (10^{-12} s) [53]. The fluorescence emission occurs within nanosecond time (10^{-9} s). The difference of the excitation wavelength and the emission wavelength is known as the Stokes shift, as shown in figure 2.6 (Source: Spectra viewer, Chroma Technology Corp.).

The fluorescence approach in a laser scanning confocal microscope provides a powerful way of creating an impressive three-dimensional view of microscopic structures, even deep inside the tissue in a noninvasive manner. The fluorescence microscope is even capable of revealing the precise location of a single molecule. Besides, the availability of thousands of fluoroprobes allows the simultaneous identification of several target molecules. As mentioned already, the basic requirement in an LSCM

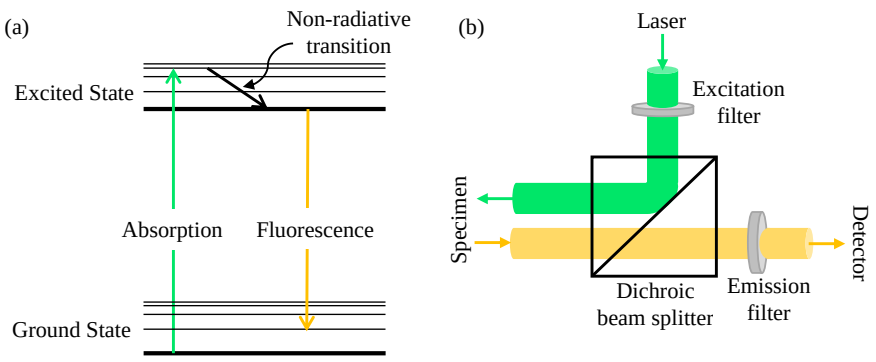

Figure 2.5: (a) The Jablonski diagram, (b) arrangement of dichroic beam splitter accompanied by excitation and emission filters.

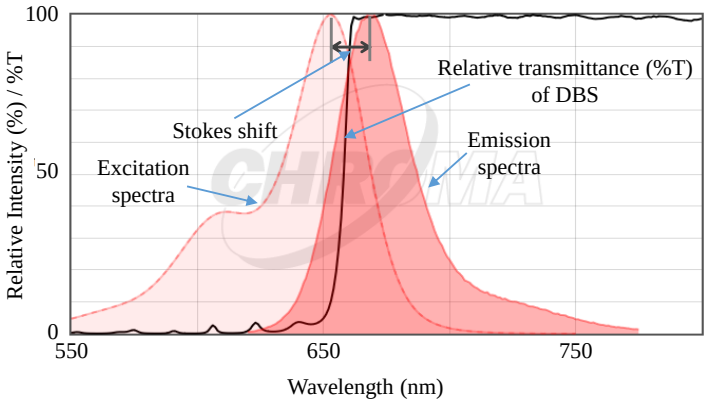

Figure 2.6: Excitation and emission spectra of fluorophore Alexa Fluor 647. Relative transmitted intensity of a suitable DBS (T660Ipxr, Chroma) for the fluorophore is shown as a solid dark plot. (Source: Spectra viewer, Chroma Technology Corp.)

working in epi-illumination fluorescence mode is the dichroic beam splitter replacing the 50:50 beam splitter. The DBS reflects incident light of wavelength shorter than a certain cut off wavelength specific to a particular DBS and transmits light of longer wavelengths. Such a DBS is often used in conjunction with an excitation and emission filter to get the best performance in fluorescence imaging. Figure 2.5(b) shows a DBS arrangement accompanied by excitation and emission filters. The laser beam spectrally filtered by the excitation filter is reflected by the DBS towards the specimen. The Stokes shifted fluorescence signal from the specimen is transmitted by the DBS. The emission filter in the path of the transmitted fluorescence signal blocks any signal at the excitation wavelength to reach the detector. The choice of DBS is such that it offers high reflectivity and transitivity in the excitation and emission wavelengths, respectively, for a given fluorophore as decided by the excitation and emission spectra of such as in figure 2.6.

2.4 Use of polarization in optical microscopes

So far we have not discussed about the polarization state of the illumination beam and whether it plays any role in the image formation or in the image analysis. In the past decades there had been a growing interest in exploiting the polarization property of the illumination beam in an optical microscope. Light matter interaction is often dependent on the relative orientation of the electric field. Adding polarization of the illumination beam as one of the parameters can provide for

the extraction of additional information on molecular organization in the specimen. For instance, the absorption or excitation efficiency of molecules in the illuminated specimen varies in accordance with the angle (θ) between the molecular dipole moment and the excitation electric field (as $\sim \cos^2\theta$) as illustrated in figure 2.7. Thus the molecule will excite with the highest probability (P_{ex}) when the absorption dipole moment and the excitation field are parallel and with the lowest probability when they are orthogonal. On the other hand, as mentioned already, the electric field orientation of a light beam at the focus of a lens directly depends on the polarization profile of the beam at the entrance pupil of the lens. Therefore, controlling the polarization profile of the illumination beam in a microscope (commonly known as polarization based microscope), it is possible to modify the orientation of the electric field to excite the molecules in the specimen, thereby enabling extraction of information on molecular orientation in the specimen. Owing to this property, the polarization based measurement is adopted in many imaging and microscopic techniques that finds applications in a diverse area. Below, two types of polarization based microscopy relevant to the thesis work are discussed .

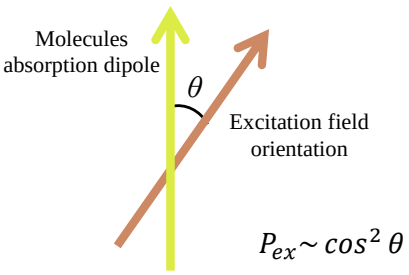

Figure 2.7: Illustration of the dependence of excitation efficiency of molecules on the angle between the molecule's absorption dipole moment and the excitation electric field.

2.4.1 Differential polarization laser scanning microscope

Differential polarization laser scanning microscope (DP-LSM) is one of the most popular polarization based microscopy techniques for the study of the anisotropic optical organization of molecules in the specimen. It finds applications in different areas such as study of root tissues [54], microscopic orientation in living cell membrane [55], anisotropic architecture of human amyloid [56], extinction cross-section of nanoparticles [57], and so on. It involves imaging of the specimen with two orthogonal linearly or circularly polarized light beams [29, 30]. The difference between the two images corresponding to the two orthogonal polarizations of the illumination beam is the measure of the linear dichroism (LD). The linear dichroism provides the

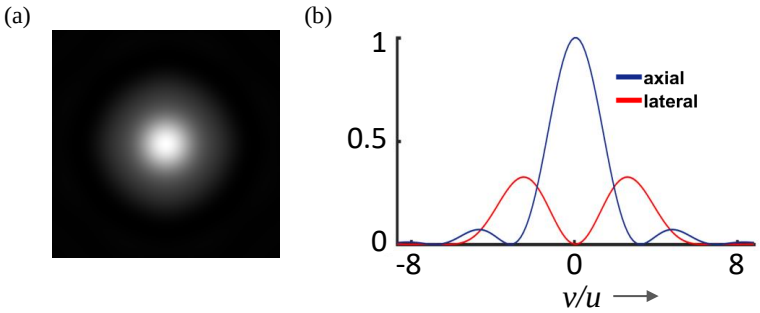

Figure 2.8: (a) Total intensity distribution at the focal plane obtained numerically due to a radially polarized beam under tight focusing (NA=1.4), covering an area $-\lambda \rightarrow \lambda$. (b) Intensity plots of the axially polarized component and laterally polarized component along a line passing through the focus.

mapping of the two-dimensional orientation of the molecules in the specimen.

2.4.2 Cylindrical vector beam based microscopy

The cylindrical vector beams have a non-homogeneous and axially symmetric polarization profile over the beam cross-section. In the last couple of decades, these beams have gained a lot of interest in the field of imaging and microscopy [58, 59]. The most significant role is perhaps played by the radial polarized beam (RPB) due to its unique property under tight focusing conditions. When focused with a high numerical aperture (NA) lens, an RPB produces a strong non-propagating axially polarized field along the optical axis near the focus. This unique property enables RPB find applications such as the study of the orientation of single molecules in three dimensions [15] as well as resolution enhancement in a microscope [60, 61]. Figure 2.8(a) shows the total intensity distribution in the focal plane obtained numerically for an oil immersion lens with NA=1.4. From the figure 2.8(b), it is clear that the axially polarized field component is stronger near the focus compared to the laterally polarized field component. The azimuthally polarized beam, another important member of the cylindrical vector beam, has also found application in resolution enhancement in a microscope [62].

2.5 Some limitations of the present polarization based microscopy techniques

In the previous chapter we discussed about some of the limitations of the existing polarization based measurements in microscopy.

The polarization of the illumination beam can be changed from one state to other, for instance, between two orthogonal plane polarization states by rotating a half wave plate placed in the beam path. To change from plane polarized beam to circularly polarized beam a quarter wave plate needs to be inserted in the beam path. As stated already, there are also active devices, for instance, electro-optic modulators such as Pockels cell [63], magneto-optic modulators such as Faraday rotator [64], that can be used to modulate or switch polarization in the illumination beam. However, it is to be ensured during polarization change that there is no physical disturbance to the beam. Besides, the applications may require the generation of not just classical polarization states but also arbitrary and user-defined polarization states in the illumination beam. This makes it necessary that the polarization based microscope is equipped with a robust and flexible polarization modulation capability without mechanically disturbing the beam.

Many polarization measurements in microscopy require capturing images with more than one polarization, such as in the method called linear dichroism [65]. Usually, change in polarization takes place at the end of an image frame. Therefore to illuminate a given location in the specimen plane with two different polarizations, it takes a time interval, which must be at least the acquisition time of one image frame. This delay will create issues while imaging specimens which are not at rest completely. Ideally, one would like to change the polarization state on a pixel to pixel basis or after every line scanned. Unfortunately, the available beam scanning confocal microscopes are not equipped with such beam forming optics enabling polarization switching after every pixel or every line scanned and between various user-defined polarization states.

In addition to the polarization profile in the entrance pupil of the lens, the phase profile of the illumination beam may also need to be modified. One important reason for dynamic control over the illumination beam phase profile is to correct the beam from the system introduced, and the specimen introduced aberrations [66]. Besides, some applications may utilize various polarization states of some special beams such

as vortex beam or helical beam [67].

The primary objective of this thesis is to come up with a robust and flexible scheme to switch the illumination beam between two or more user-defined polarization profiles, which will also permit dynamic control over the phase of the beam. The scheme will be employed in a confocal system that will enable polarization switching at the end of every line scanned, without disturbing the beam mechanically. The proposed confocal system should work in both reflectance and fluorescence modes so that a large number of applications can be covered.

2.6 Important components of the basic confocal system developed in this thesis

As stated in section 2.3, apart from the intermediate optical components, a laser scanning confocal microscope has a number of important building blocks such as a laser, objective lens, scanning unit, and photo-detector. Below, each important component of the basic confocal setup developed this thesis work is briefly described.

2.6.1 The laser

The laser provides the source of light for illumination in a scanning confocal microscope. In choosing a laser in LSCM, the crucial parameters that are to be considered comprise the spatial mode profile, the power stability, and the spectral bandwidth. Most of the applications require laser having TEM_{00} output mode with stable power and narrow spectral bandwidth. In this thesis, two lasers were used, one is a Helium-Neon (He-Ne) laser (Make: Melles Griot, Model: 05-LHP-991) and another is a diode-pumped solid-state (DPSS) laser (Make: Spectra-Physics, Model: Excelsior-532-200-CDRH). The specifications of the two lasers are given in a tabular form (Table 2.1).

2.6.2 The objective lens

The objective lens in an optical microscope is the component closest to the object (specimen) being imaged and plays the most crucial role in determining the quality of the image that the microscope can produce. For the optimum performance of the microscope, the aberration by the objective lens should be minimum. The resolution

Table 2.1: Laser specifications

	05-LHP-991	Excelsior-532-200-CDRH
Wavelength	632.8 nm	532 nm
Spatial Mode	TEM_{00}	TEM_{00}
Beam Quality (M^2)	< 1.05	< 1.1
Output Power	10mW	200 mW
Beam diameter ($1/e^2$)	0.65 mm	0.32 ± 0.02
Beam Divergence	1.24 mrad (Full Width)	< 2.5 mrad (Collimated)
Operation Temperature Range	$-20^o \rightarrow 40^o$	$10^o \rightarrow 40^o$

of an LSCM is mostly affected by spherical aberration and axial chromatic aberration. The least expensive objective lenses are the **achromatic** objectives. Such objectives are corrected for axial chromatic aberrations at two extreme wavelengths and spherical aberration in an intermediate wavelength. **Plan achromat** objectives are the achromatic objectives that extends the correction for the flatness of the field by removing the field curvature. **Semi-apochromats** are the objective lenses that offer the next higher level of correction. These objective lenses correct chromatic aberrations for three wavelengths and spherical aberration for two wavelengths. In addition, such objectives have improved transmission characteristics in the ultraviolet spectral region. Objective lenses that have the highest level of corrections for chromatic and spherical aberrations are called **apochromats**, where the chromatic aberration is corrected for three wavelengths and spherical aberration for two or three wavelengths. In addition to the correction for spherical aberrations as that of apochromats, **super-apochromats** objective lenses offer near-perfect correction for chromatic aberration such that near-infrared (near-IR) field can focus at the same focal plane as that of visible light. In our experiment, we use three objective lenses (Make: Olympus), the details of which are given in table 2.2.

Table 2.2: The specifications of the objective lens used in the experiments

Product Name	UPLFLN10X2	LUCPLFLN40X	UPLSAPO100XO
Magnification	10X	40X	100X
Numerical aperture	0.30	0.60	1.4
Immersion Medium	Air/Dry	Air/Dry	Oil
Correction Level	Semi-apochromat	Semi-apochromat	Super-Apochromat

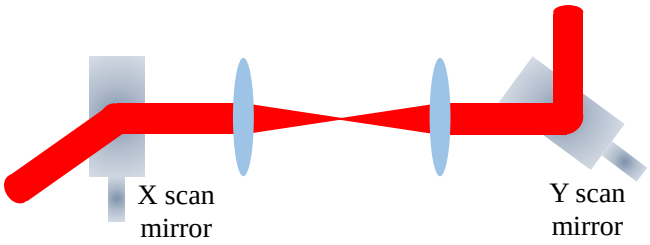

Figure 2.9: Use of $4f$ relay to image the X scan mirror onto the Y scan mirror.

2.6.3 The scanning unit

In general, the beam scanning in a laser scanning confocal microscope is achieved using two rotating mirrors mounted on galvanometers. The two mirrors are used to scan the laser beam across the specimen in a raster fashion, where one is the fast scanning mirror that scans in the horizontal direction (x-axis), and the other slowly scans in the vertical direction (y-axis). In state of the art galvanometer based scanning, a controller unit coordinates the movement of the mirrors about the two scan axes. The controller unit receives the user-define command sent through a personal computer (PC) interface, and then it generates the appropriate electrical signal to be sent to the servo driver attached to the galvanometer. When commanded in a single step, the mirror is rotated to a given angular position by a positioning actuator. A position detector then senses the actual position of the actuator and reports to the closed-loop servo system. The servo driver connected to the respective mirror demodulates the position detector's signal, compares it with the commanded position signal, and then drives the actuator to bring the mirror to the desired position [68]. This closed-loop procedure enables the scan mirrors to send the laser beam precisely to the commanded position.

In some of the experiments related to this thesis, the beam scanning is achieved by using two moving magnet closed-loop galvanometer based scanning mirrors (Make: Cambridge Technology, Model: 6231HM44A) equipped with EC1000 control board and two servo drivers (Made: Micromax, Model: 671231H14-HP). For the best imaging performance in two-axes steered-beam systems, the two mirrors are positioned optically conjugate to each other by using a $4f$ relay system in between them. The use of a relay optics to image the X scan mirror onto the Y scan mirror is shown in figure 2.9. Use of such relay optics ensures that there is no wobble in the beam cross-section at the entrance pupil of the objective lens, as the beam is scanned.

2.6.4 The detector

The detector plays the role of converting the light coming from the specimen into the electrical signal to be read and stored by the PC. The charge-coupled device (CCD) and the complementary metal-oxide-semiconductor (CMOS) are two important photo-detectors used in most of the imaging applications. Both the devices comprise a two-dimensional array of photo sensitive pixels that converts incident light into electrons. In the case of CCD detector, the photoelectrons are converted into voltage at one location each array of pixels, whereas the conversions take place at each pixel in case of CMOS detector. Because the conversion takes place parallelly at each pixel instead of serially as in the case of CCD detector, the CMOS detector offers a fast acquisition rate in an imaging system. Also, CMOS detectors are cost-effective and consume less power. On the other hand, CCD sensors are more light sensitive than that of the CMOS sensors and provide better image quality due to high signal to noise ratio (SNR). A photomultiplier tube (PMT) is another photo-detector that is suitable where the amount of light reaching the detector is very less. In the case of PMT, photons striking a photo-cathode at the entrance window lead to emission of electrons, which are multiplied using a series of dynodes by secondary emission. These multiplied electrons then strike on the anode to eventually get converted into an electronic signal. The primary advantages of the PMT include fast response, high SNR and low dark current.

In our experiments, we use a CMOS camera (Make: Thorlab Inc., Model: DCC3240), a CCD camera (Make: Basler vision technologies, Model: A631f) and a PMT (Make: Hamamatsu photonics, Model: H11462-032) as photo-detectors. The CMOS camera used has a resolution of 1280 $\times$ 1024 pixels with a pixel pitch of $5.3\mu m$. It provides a maximum frame rate of 60 Hz in free-run mode and of 56.9 Hz in trigger mode. The camera can easily connect to a PC via a universal serial bus (USB) 3.0 interface and provides 10-bit pixel value resolution (8-bit resolution in case of USB 2.0 interface). The CCD camera has a pixel pitch of $4.65\mu m$ and a resolution of 1392×1040 pixels. At full resolution, the maximum frame rate achievable is 18.7 frames per second (fps). The camera has the provision of long exposure mode and programmable selection of area of interest (AOI). The AOI feature facilitates enhancement in the frame rate if number of active rows is reduced. The PMT used here is a voltage output type photosensor module with an effective area of $4 \times 20mm$. The PMT gain can be adjusted (between $7{*}10^4$ and $3{*}10^7$) by regulating an external

control voltage (between $0.5V$ and $1.2V$), where a voltage divider or a potentiometer circuit is used to regulate the control voltage. The radiant sensitivity of the cathode is $90mA/W$, and that of the anode is $85.5V/nW$, both at $+1V$ control voltage and at wavelength $400nm$ corresponding to peak sensitivity. A data acquisition (DAQ) card (Make: National Instruments, Model: NI 6133) is used to perform the analog-to-digital conversion (ADC) of the PMT output voltage. The DAQ card has eight analog input channels with a 14-bit resolution ADC. Each channel can convert the incoming signal at a maximum sampling rate of 2.5 mega samples per second, while the sampling can be synchronized with an external trigger.

2.7 Conclusion

In this chapter, a brief introduction to the laser scanning confocal microscope has been provided. It has included a discussion on the importance and use of the polarization profile of the illumination beam in an optical microscope. Polarization based microscopic techniques relevant to the thesis work has been also discussed. The chapter has then discussed some limitations of the present polarization based measurement techniques using the confocal microscope and stated the basic objective of the thesis work. The important components required to build a laser scanning confocal microscope for the purpose of the experimental work related to the thesis have also been briefly described.

* * *

Chapter 3

Computer Generated Holography to Produce Arbitrary Scalar and Vector Beams

3.1 Introduction

As already mentioned, the primary objective of the thesis work involves the vector beam illumination in a laser scanning confocal microscope. A laser beam with user-defined complex amplitude and polarization profile over the cross-section of the beam can be termed as an arbitrary vector beam. In this chapter, we introduce computer generated holography, followed by a discussion on the liquid crystal spatial light modulator, a device used to write computer generated holograms in a dynamic fashion. The chapter then describes the use of computer generated holography to generate an arbitrary scalar beam, where scalar beam refers to a light beam with a user-defined complex amplitude profile irrespective of the polarization. It concludes with a discussion on the implementation of computer generated holography in an optical arrangement to generate arbitrary vector beam profiles.

3.2 The principle of computer generated holography

Holography is a two-step process to record the complex amplitude profile of a light beam from an object and to reproduce it at any later time even without the object [69]. In the first step, the interference pattern produced by a reference beam (usually a plane wave) and a mutually coherent light beam scattered by the object (termed the object beam) is recorded on a photographic plate. The reference

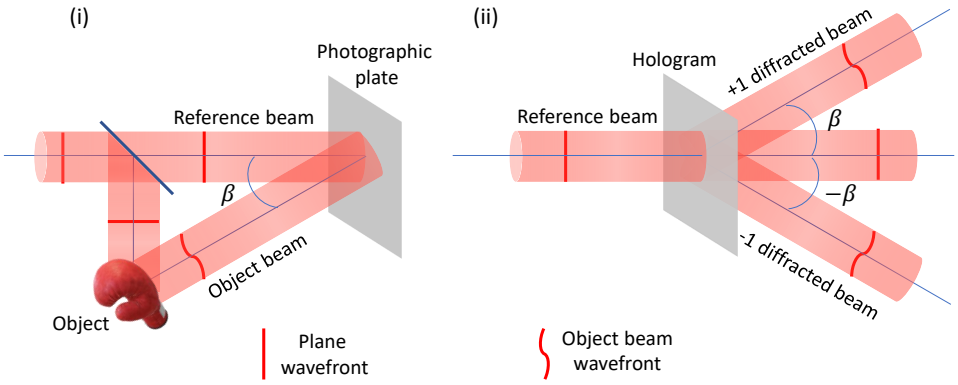

Figure 3.1: Illustration of (i) recording of hologram, (ii) reconstruction of the object beam in the +1 diffracted order.

beam and the beam used to illuminate the object are derived from the same source, usually using a division of amplitude method, so that the two beams are mutually coherent. The record of the interference pattern is termed the hologram, which has a transmittance function proportional to the interference pattern. The second step is the reconstruction of the complex amplitude profile of the object beam by illuminating the hologram with the same reference beam in a manner similar to the previous step. We consider that the reference beam and the object beam meet at the interference plane at an angle β, as seen in the figure 3.1(i). During reconstruction, assuming the reference beam to have a constant amplitude, the hologram diffracts the reference beam into three beams, two beams making angles β and $-\beta$ with respect to the direction of the reference beam, and the undiffracted beam in the same direction as the reference beam, as seen in the figure 3.1(ii). Considering a plane wave as the reference beam, the diffracted beam that makes an angle β, termed the +1 diffracted order beam, retains the complex amplitude profile of the object beam. The diffracted beam that makes an angle $-\beta$ retains the conjugate of the complex amplitude profile of the object beam and is termed the -1 diffracted order beam. The undiffracted beam replicates the reference beam and is termed the 0 order beam. Thus it is noticed that the complex amplitude profile of the object beam can be reconstructed precisely in the +1 order diffracted beam by fabricating a hologram that has a transmittance function proportional to the interference between the object beam and the reference beam. Thus knowing the two dimensional function representing the interference, one may reconstruct the object beam from the reference beam, even without the physical construction process. This is the principle of computer generated hologra-

phy [70, 71], where interference pattern between a reference beam and the object beam is first computed to later fabricate the corresponding hologram.

In addition to the three diffracted beams, on reconstruction, the hologram may diffract the incident reference beam into more beams depending on whether the transmittance function of the hologram correctly represents the interference between the reference beam and the object beam. A hologram is called a sinusoidal hologram if the transmittance function of the hologram comprises sinusoidal gray level values corresponding to each interference fringe. The hologram is called a binary amplitude hologram if the transmittance function of the hologram has two values, one value representing 100% and the other value representing 0% transmittance of the light incident on the hologram. Such binarization is achieved by thresholding the sinusoidal interference pattern. If a binary hologram is designed in such a way that the two transmittance values of the hologram represent the introduction of a phase delay of 0 or π into the incident beam, then the hologram is called a binary phase hologram. Unlike the sinusoidal hologram, the binary holograms give rise higher order diffracted beams in addition to the ± 1 order beams. Besides an ideal binary phase hologram does not give rise to the 0 oder beam. However in all the cases the $+1$ oder beam carries the complex amplitude profile of the object beam in a similar manner. More elaborate discussion on the implementation of binary holograms is provided in the later sections of the chapter.

In this thesis, we make use of programmable liquid crystal spatial light modulator to implement the computer generated holograms. The LCSLM facilitates writing of holograms in a reconfigurable manner and in real time. Here we implement binary amplitude hologram for efficient and accurate implementation of CGH using the LCSLM. In the later part of the thesis, we will call such binary amplitude hologram as a binary hologram (by dropping the "amplitude" term).

3.3 Liquid crystal spatial light modulator

A spatial light modulator (SLM) is a device that can modulate the phase or amplitude profile of an incident light beam in real-time. There exists different types of spatial light modulators such as magneto-optic SLMs, deformable mirror SLM, acousto optic SLMs, and liquid crystal SLMs that can perform the modulation of the complex amplitude profile of an incident light beam. However, we will confine our discussion on the basic principle of LCSLM only, as the same is used in this thesis.

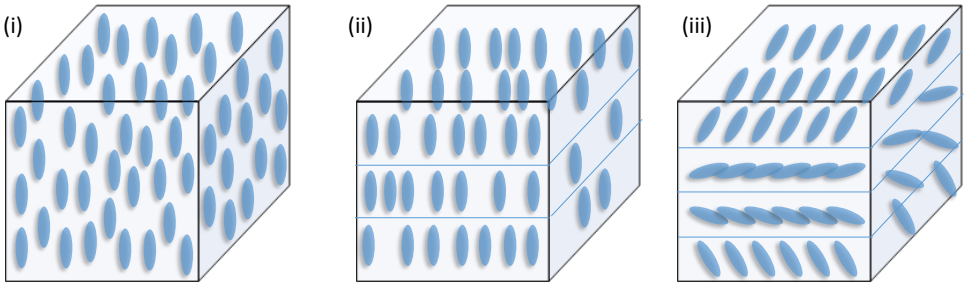

Figure 3.2: Arrangements of the LC molecules in the case of (i) nematic liquid crystal, (ii) smectic liquid crystal and (iii) cholesteric liquid crystal.

An LCSLM comprises a two-dimensional array of liquid crystal cells or pixels. The liquid crystal is a state intermediate between crystalline solid and isotropic liquid [49]. The LC molecules are elongated in shape along one axis, termed as the single long axis, about which the shape is circularly symmetric. The molecule can have a certain amount of rotation or translation without affecting its form, under the application of external force such as the action of an electrical field, thereby the molecules exhibiting the properties of a liquid. However, the LC molecules show the property of long-range orientational order associated with a solid. The most important and widely used liquid crystals are thermotropic, where the physical properties such as dielectric constant, refractive index, etc. are temperature dependent. Depending on the organization of the LC molecules, the thermotropic liquid crystals are divided into three different classes, namely nematic, smectic, and cholesteric. For nematic liquid crystals, the molecules are aligned with the long axes parallel to each other over the entire volume with randomly located centers, as shown in figure 3.2(i). Figure 3.2(ii) shows the arrangements of LC molecules in the case of smectic liquid crystal, where the molecules are again aligned parallel to each other over the entire volume, but the centers lie in parallel layers. In the case of cholesteric liquid crystal, like the smectic one, the centers of the molecules lie in parallel layers, whereas the orientation of the molecules from layer to layer undergo a helical rotation about an axis, as shown in figure 3.2(iii).

Figure 3.3(i) shows the schematic of an electrically controlled LC cell. Here, the liquid crystal molecules are kept in a small volume (side length of few μm) enclosed by two glass plates. The electric field is applied via two transparent conductors made by coating (for example, with indium tin oxide) the inside of the glass plates. The transparent conductors are covered with two alignment layers to achieve the alignment of the LC molecules at the interface. The molecules adjacent to the align-

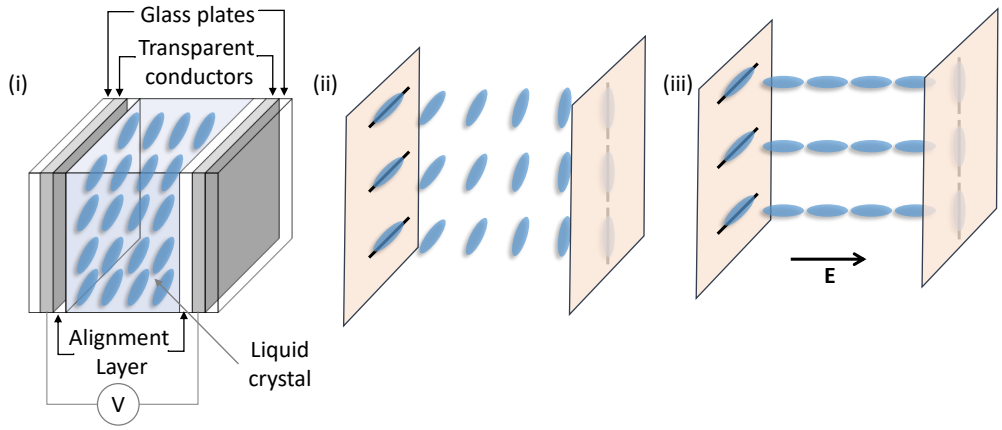

Figure 3.3: (i) Schematic of an electrically controlled LC cell. Illustration of the molecular orientation in a twisted nematic liquid crystal cell (ii) in the absence of electric field, and (iii) in the presence of applied electric field across the cell. Solid lines in black show the scratch marks in the alignment layers.

ment layer are constrained to orient parallel to the unidirectional scratch mark made on the alignment layer. On the other hand a molecule also tends to have the same orientation as its adjacent molecule. The elongated shape and the parallel alignment of the molecules enable the liquid crystal material to exhibit the property of optical birefringence. The LC molecules provide a higher refractive index to light polarized parallel to the long axis of the molecule than to light polarized perpendicular to the long axis. However, on application of an electric field, an electric dipole is induced in some material such as nematic, making the LC molecule orient itself in the direction of the electric field. Such change in orientation due to an applied electric field also takes place in LC molecules which have a permanent dipole moment. Therefore the effective refractive index offered by an LC cell can be altered by controlling the electric field applied across the cell. The liquid crystal based SLMs exploit this property to achieve the modulation of the complex amplitude profile of the incident beam. The commercial LCSLMs are mostly based on the nematic liquid crystal and the ferroelectric liquid crystal, which is a special class of smectic liquid crystal (termed as smectic-C*). Below, we will discuss these two types of LCSLMs and how they can be used to implement binary holograms.

3.3.1 Nematic liquid crystal spatial light modulator

Nematic liquid crystal spatial light modulator (NLCSLM) comprises a two-dimensional array of nematic liquid crystal cells or pixels. The nematic LC molecules have an in-

herent tendency to remain aligned to their nearby molecules, whereas the molecules near the alignment layers tend to align parallel to the scratch marks. Now, if the two alignment layers on either side of an LC cell enclosing the molecules are scratched in mutually perpendicular directions, the molecules near the layers will be constrained to align along the direction of scratch marks while the intermediate molecules will try to follow their nearby molecules, thus forming a twist as shown in figure 3.3 (ii). The liquid crystal SLM made up of such nematic LC cells is termed as twisted-NLCSLM (TNLCSLM). On the application of an electric field of sufficient strength across the two transparent conductors, the induced electric dipole will make the molecules (except the ones near the alignment layers) to align parallel to the direction of the electric field. Figure 3.3 (iii) illustrates the application of the electric field to align the intermediate molecules of twisted-nematic LC cells parallel to the direction of the applied field. Let us consider a laser beam to be passed through such an LC cell with its polarization parallel to the scratch mark made on the entrance face. In the absence of an electric field, as the beam passes through the cell of a definite width, the polarization of the light beam follows the molecular twist to undergo a rotation of 90^o as it comes out of the cell. In the presence of the electric field across the cell, the laser beam will cross the cell without any change in its polarization state. Thus if a polarizer is placed just after the exit face with the polarization axis orthogonal to the scratch mark on the exit face, the laser beam will be available at the other side of the polarizer only when the electric field is applied across the cell. In the absence of the electric field, due to the polarization rotation of 90^o no laser beam will pass through the polarizer. This property is used in the implementation binary hologram in a NLCSLM. The binary amplitude "0" of a particular pixel in the hologram corresponds to an LC cell/pixel with no electric field applied across the cell. Similarly, the binary amplitude value "1" corresponds to an LC cell/pixel with an applied electric field across the cell.

In this thesis, we use two reflective type TNLCSLMs of HOLOEYE make namely "LC-R 720 Reflective LCOS SLM" and "LC-R 1080 Reflective LCOS SLM". The former one has Wide Extended Graphics Array (WXGA) pixel resolution (1280×768) with a pixel pitch of $20\mu m$ covering an active area equal to $25.6 \times 15.4mm$. The later one has a very high pixel resolution of 1920×1200, called Widescreen Ultra Extended Graphics Array (WUXGA) resolution, with a pixel pitch of $8.1\mu m$ covering an active area equal to $16.39 \times 10.56mm$. Both the devices can read input signals as 8-bit gray levels and can be refreshed at a rate of 60Hz via a digital visual

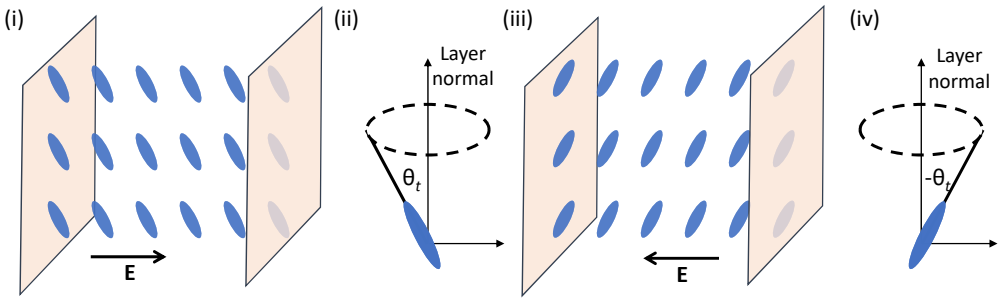

Figure 3.4: Illustration of the switching of the plane of inclination of the molecules from θ_t as in (i) and (ii), to $-\theta_t$ as in (iii) and (iv), on reversal of the polarity of the DC field applied across the ferroelectric liquid crystal cell.

interface (DVI) with a PC.

3.3.2 Ferroelectric liquid crystal spatial light modulator

As stated already the ferroelectric liquid crystal spatial light modulator (FELCSLM) comprises a two-dimensional array of a special class of smectic (called smectic C*) liquid crystal cells or pixels. As discussed earlier, the molecules in the smectic LC cell are aligned parallel to each other over the entire volume, with the long axes perpendicular to the layer. In the case of the smectic-C phase, the molecules are tilted, making an angle with the layer normal, whereas the molecules in smectic-C* phase are chiral as the long axes rotate as a helix from one layer to the other. In each layer, the molecules are aligned at an angle (say θ_t) with the layer normal. The plane of inclination of the molecules can be switched from θ_t to $-\theta_t$ by reversing the polarity of a DC field applied across the cell as shown in figure 3.4. It is also observed that the molecules retain their orientation even after the removal of the electric field. Such liquid crystals therefore are also termed as ferroelectric liquid crystals. The thickness of the LC cell is chosen in such a way that the cell for an incoming beam behaves as a half wave plate. The optical axis of the half wave plate is rotated by changing the DC field, thereby enabling the LC cell to provide binarized amplitude modulation to an incident beam. Thus similar to NLCSLM, FELCSLMs integrated with a PC can be used to write binary holograms computed. In the work presented in this thesis, we use an FELCSLM (Make: FORTH DIMENSION DISPLAY, Model: SXGA - R2) having a resolution of Super Extended Graphics Array (SXGA, 1280×1024) at $13.62\mu m$ pixel pitch. It can read the input signal as a color image (having 24-bit information) that can be refreshed at a rate of 60Hz

via DVI with a PC. Since a 24-bit color image can comprise 24 single-bit or binary images, thus the FELCSLM facilitates writing of binary holograms at a rate of 1440Hz (60×24). The FELCSLM has driver board that interprets the incoming video using a sequence file. The sequence file can be updated in such a way that the 24-bit color image is converted to a 3-bit image before displaying each bit as a binary image. The sequence file that displays 24 binary images per color image is called 24-bit sequence file and the sequence file that displays 3 binary images per color image is called 3-bit sequence file. As it is the permanent dipole moment of the ferroeletric molecules that responds to the applied DC field, it is important that a certain LC cell is not subjected to the field for long without changing the polarity. To ensure this the sequence file, implements the display of the corresponding negative binary image after the display of each binary image such that even for a fixed pattern sent by the PC, the display is altered periodically between the positive and the negative patterns.

Thus both the NLCSLM and the FELCSLM can be employed to implement binary holograms constructed using the computer generated holography technique, where the former allows a refresh rate of about 60 HZ while the later allows a refresh rate of more than 1000 Hz. The next section describes in detail the algorithm adopted to compute such binary holograms to generate the user-defined beams.

3.4 Generation of arbitrary scalar beam using computer generated holography

3.4.1 Beam with user-defined wavefront

The generation of an arbitrary scalar beam using binary holograms was demonstrated by Neil et al. in 1998 [44]. Here a binary hologram is illuminated by a plane wave and the user-defined scalar complex amplitude profile is realised in the pupil plane (of a lens or imaging system), which is optically conjugate to the hologram plane as seen in figure 3.5. Let us consider that $\phi(x, y)$ is the overall desired phase function of the scalar beam (i.e. the object beam) and x, y are the coordinates of the hologram plane. Assuming the object beam to have a uniform amplitude over the beam cross-sectional area (say unit amplitude), the complex amplitude profile of the object beam can be represented as $A(x, y) = e^{i\phi(x,y)}$. We may define

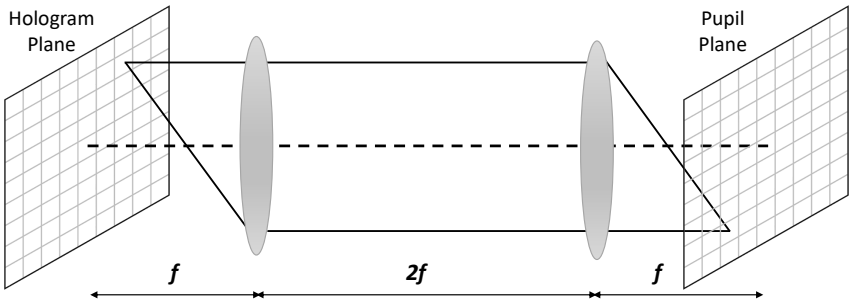

Figure 3.5: Use of $4f$ relay to make the pupil plane conjugate to the hologram plane.

$\phi(x,y) = \phi_b(x,y) + \tau(x,y)$, where $\phi_b(x,y)$ is the phase difference relative to a plane perpendicular to the propagation direction of the object beam and $\tau(x,y)$ is a linear tilt function describing the propagation direction of the object beam. Thus the tilt function $\tau(x,y) = \tau_x x + \tau_y y$ determines the deflection of the object beam with respect to the undiffracted 0 order beam, where, τ_x (termed as x-tilt) and τ_y (termed as y-tilt) describe the deflections along the horizontal and vertical directions, respectively. The values of x-tilt and y-tilt correspond to the angle β described in the section 3.2 as $\beta = \tan^{-1}(\tau_y/\tau_x)$. The transmittance function T_{bh} of the binary amplitude hologram can be written as [44, 71]

$$T_{bh}(x,y) = \begin{cases} 1 & \text{if } -\pi/2 \geq \phi(x,y) \geq \pi/2 \\ 0 & \text{other wise} \end{cases} \tag{3.1}$$

The binary hologram is usually described over a unit circle defined by the coordinate values satisfying $\sqrt{x^2+y^2} \leq 1$.

In order to understand the generation of the user-defined object beam profile in the +1 order beam we do a Fourier series analysis of the binary transmittance function. It is seen from Eq. 3.1 that T_{bh} vs ϕ gives rise to a square wave with a period of 2π [71, 72]. Therefore using the property of the square wave, the Fourier series expansion of $T_{bh}(x,y)$ can be written as

$$T_{bh}(x,y) = \frac{1}{2} + \frac{1}{\pi}\left[\left(e^{i\phi} + e^{-i\phi}\right) - \frac{1}{3}\left(e^{i3\phi}e^{-i3\phi}\right) + \frac{1}{5}\left(e^{i5\phi} + e^{-i5\phi}\right) + ...\right]. \tag{3.2}$$

Considering the hologram to be at the front focal plane of a lens, the diffraction pattern of $T_{bh}(x,y)$ at the back focal plane of the lens can be obtained by the

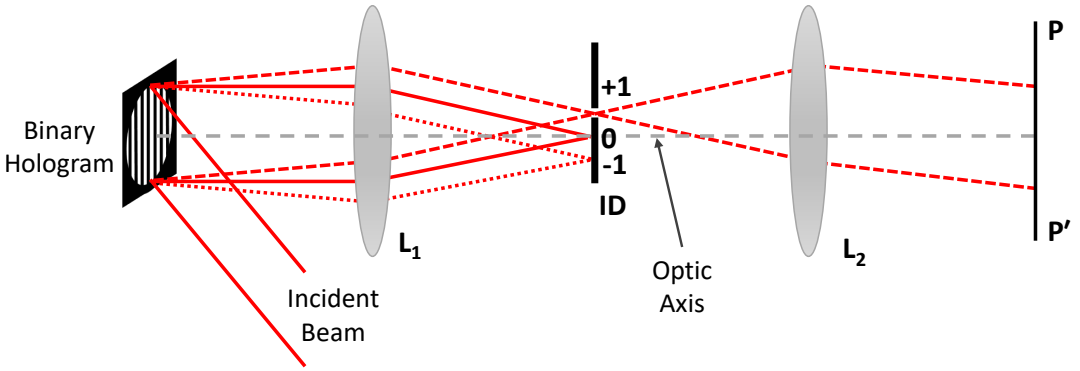

Figure 3.6: Illustration of a basic setup of binary hologram to realise a user-defined beam.

Fourier transform of $T_{bh}(x, y)$ given as

$$T(f_x, f_y) = \int\int T_{bh}(x, y) e^{-2\pi i(xf_x + yf_y)/\lambda f} dxdy \tag{3.3}$$

where $(k_x = {}^{f_x}/_{\lambda f}, k_y = {}^{f_y}/_{\lambda f})$ are the Fourier plane coordinates that are related to the spatial frequency coordinates (f_x, f_y). Here λ is the wavelength of the light beam used and f is the focal length of the lens that performs the Fourier transform. From equation 3.2 we can see that the Fourier plane comprises the diffracted orders $\pm1, \pm3, \pm5, \cdots$, positioned at relative distances of $(\pm1, \pm3, \pm5, \cdots)$ with respect to the undiffracted 0 order beam, with relative intensities $\frac{1}{\pi^2}\left(1, \frac{1}{9}, \frac{1}{25}, \cdots\right)$. Besides the diffracted orders carry phase profile $(\pm1, \pm3, \pm5, \cdots)\,\phi$ in addition to the incident beam phase profile. Since the $+1$ diffracted order retains the phase profile that was used to construct the hologram, the same reconstructs the object beam, and it can be isolated from other orders by performing an optical spatial filtering to realise an arbitrary user-defined scalar beam.

Figure 3.6 illustrates a simple setup of the binary hologram to realise an arbitrary scalar beam. The binary hologram constructed using the CGH technique diffracts an incident collimated laser beam into a number of orders (here, only $+1, -1$ and undiffracted 0 order beams are shown for clarity), which are then focused by the lens L_1 onto an iris diaphragm ID. The ID is used to isolate the $+1$ diffracted order from the other orders. The $+1$ diffracted order beam is then re-collimated using the lens L_2. In this way, one can realise an arbitrary scalar wavefront in the pupil plane PP', which is optically conjugate to the hologram plane.

In this thesis, we often use the phase function $\phi_b(x, y)$ to represent monochro-

Table 3.1: Single index Zernike circular polynomials representing a few optical aberrations

j	$Z_j(x,y)$	Common Name
4	$2\sqrt{3}\big(2(x^2+y^2)-1\big)$	Defocus
5	$2\sqrt{6}xy$	Primary astigmatism at $\pm 45^o$
6	$\sqrt{6}(x^2-y^2)$	Primary astigmatism at 0^o
7	$\sqrt{8}\big(3(x^2+y^2)-2\big)y$	Primary y-coma
8	$\sqrt{8}\big(3(x^2+y^2)-2\big)x$	Primary x-coma
9	$\sqrt{8}(3x^2y-y^3)$	y-trefoil
10	$\sqrt{8}(x^3-3y^2x)$	x-trefoil
11	$\sqrt{5}\big(6(x^2+y^2)^2-6(x^2+y^2)+1\big)x$	Primary spherical aberration

matic aberrations expressed as a linear combination of single index Zernike Polynomials [73, 74]. Table 3.1 shows a few Zernike polynomials $\big(Z_i(x,y)\big)$ corresponding to some common optical aberrations. Thus for a plane incident wave, the +1 diffracted order beam corresponding to a binary hologram with the phase function $\phi_b(x,y)=0$ will represent a plane wavefront, whose tilt in the pupil plane can be controlled via (τ_x,τ_y) employed in the construction of the binary hologram. Binary holograms computed using a MATLAB program with $\tau_x = 10\pi$, $\tau_y = 10\pi$, and, $\phi_b(x,y)$=0 and $\phi_b(x,y) = Z_8(x,y)$ are shown in figure 3.7(i) (a) and (b), respectively. The corresponding diffraction orders in the Fourier plane computed by performing Fourier transformation on the holograms using MATLAB's FFT (Fast Fourier Transform) tool are shown in figure 3.7(ii) (a) and (b), respectively. The focal spots of the +1 diffracted order beams retaining the desired complex amplitude profile are shown in the insets of figure 3.7(ii).

In the above, the generated scalar beams have a uniform unit amplitude over the entire cross-section with a user-defined phase profile. Below we discuss how to generate a scalar beam with user-defined amplitude as well as phase profile over the beam cross-section.

3.4.2 Beam with user-defined amplitude and wavefront

Figure 3.8(i) shows the transmittance function at a point in the binary hologram, described by equation 3.1 vs 2π modulo of the desired phase. Here $\phi(x,y)$ is compared with a fixed value $\alpha = \pi/2$ so that it results in the maximum amplitude at the corresponding location of the +1 order beam. However, choosing the value of

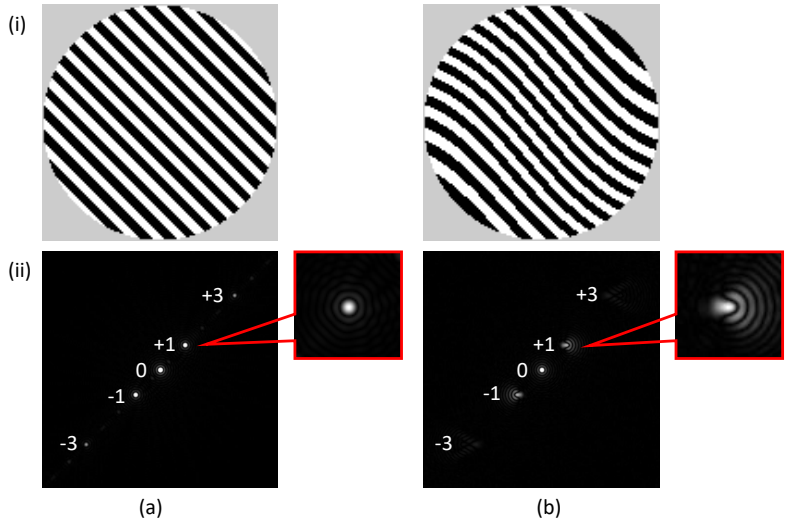

Figure 3.7: (i) Binary amplitude hologram with $\tau_x = 10\pi$, $\tau_y = 10\pi$ and (a) $\phi(x, y) = 0$ and (b) $\phi(x, y) = Z_8(x, y)$, (ii) resulting diffraction orders in the Fourier plane. The focal spots of the +1 diffracted order beams retaining the desired complex amplitude profile are shown in the insets of (ii).

α to be (x, y) dependent lying between 0 and π, one can design a binary hologram that has control on both the amplitude and phase in the diffracted order beam. Let us consider $A(x, y)e^{i\phi(x,y)}$ to be the complex amplitude profile of the +1 diffracted order beam. Assuming $A(x, y)$ to be normalised (to 1), the transmittance function $T_{bh}(x, y)$ of the binary hologram can be defined as shown in figure 3.8(ii) as

$$T_{bh}(x, y) = \begin{cases} 1 & \text{if } \phi(x, y) < \alpha(x, y), \\ 0 & \text{if } \phi(x, y) \geq \alpha(x, y). \end{cases} \tag{3.4}$$

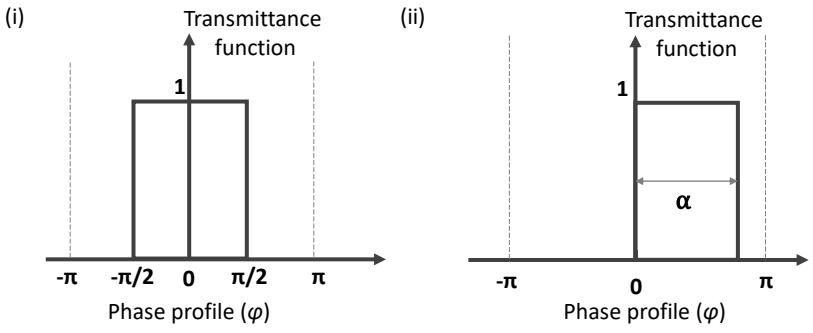

Figure 3.8: A plot of transmittance function vs 2π modulo of the desired phase for generation of a scalar beam with (i) the maximum amplitude and (ii) user-defined amplitude value.

On performing the Fourier series analysis [75] on the plot seen in figure 3.8(ii), the coefficients a_n of cosine and b_n of sine terms in the Fourier series are found to be

$$a_n = 0$$
$$b_n = \frac{2}{n\pi} \sin^2 \frac{n\alpha(x,y)}{2}$$

where, n is an integer. From the expression of b_n and using

$$\sin(n\phi) = \frac{e^{in\phi} - e^{-in\phi}}{2i},$$

one may write b_{+1}, the coefficient of $e^{i\phi(x,y)}$, as

$$b_{+1} = \frac{1}{i\pi} \sin^2 \frac{\alpha(x,y)}{2}. \tag{3.5}$$

The value of b_{+1} varies between 0 and $1/i\pi$ since α varies between 0 and π. Assuming the beam illuminating the binary hologram to have unit amplitude, the amplitude profile of the +1 diffracted order beam will be $b_{+1}(x,y)$. Thus, taking the normalization factor into account, the amplitude profile of the +1 diffracted order beam can be expressed as

$$A(x,y) = \sin^2 \frac{\alpha(x,y)}{2}. \tag{3.6}$$

Using the above equation, $\alpha(x,y)$ for the given amplitude profile can obtained as

$$\alpha(x,y) = 2\sin^{-1}\sqrt{A(x,y)}. \tag{3.7}$$

Therefore, the construction of binary hologram to achieve arbitrary scalar amplitude $A(x,y)$ and phase $\phi(x,y)$ in the +1 diffracted order beam, involves the following steps.

- Define the complex amplitude profile of the +1 diffracted order beam $A(x,y)e^{i\phi(x,y)}$ with normalized $A(x,y)$, where the phase $\phi(x,y)$ comprises the desired phase and the tilt function mentioned in section 3.4.1.
- Define the parameter $\alpha(x,y)$ as $\alpha(x,y) = 2\sin^{-1}\sqrt{A(x,y)}$.
- Define the transmittance function of the binary hologram by comparing $\phi(x,y)$ with $\alpha(x,y)$ as in equation 3.4.

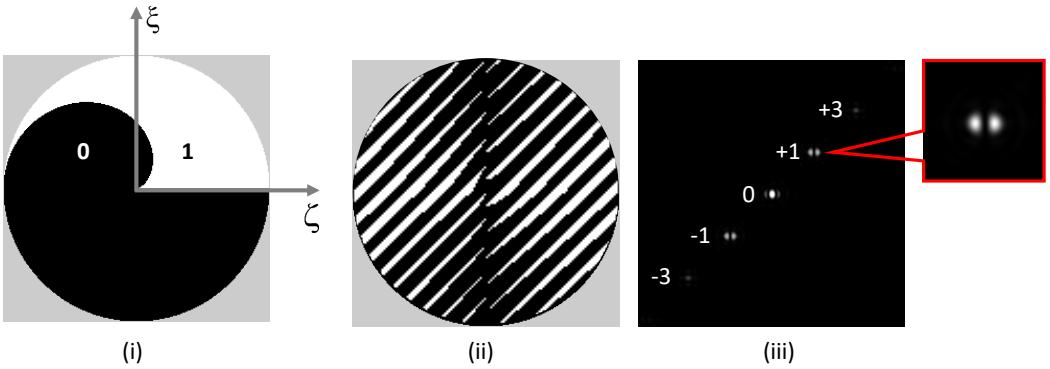

Figure 3.9: (i) Binary amplitude map representing the transmittance value of the binary hologram corresponding to the complex amplitude $(\zeta + i\xi)$ in the pupil plane. (ii) A binary hologram computed to generate a beam with an amplitude profile of $\cos\varphi(x, y)$, where $\varphi(x, y)$ represents the azimuthal angle in the beam cross-section. (iii) Resulting diffraction orders in the Fourier plane. The focal spot of the +1 diffracted order beam is shown in the inset of (iii).

Now writing

$$\begin{aligned} A(x,y)e^{i\phi(x,y)} &= A(x,y)\cos(x,y) + iA(x,y)\sin(x,y) \\ &= \zeta(x,y) + i\xi(x,y) \end{aligned}$$

we have

$$A(x,y) = \sqrt{\zeta^2(x,y) + \xi^2(x,y)} \quad \text{and} \quad \phi(x,y) = \tan^{-1}\frac{\xi(x,y)}{\zeta(x,y)}.$$

Therefore a given arbitrary complex amplitude profile $A(x, y)e^{i\phi(x,y)}$ is represented by a coordinate point inside a unit circle centered on the origin in the (ζ, ξ) plane. A binary amplitude map as seen in figure 3.9(i) can thus be constructed by painting each pixel of the unit circle as black or white based on whether the corresponding $T_{bh}(x, y)$ is 0 or 1. Figure 3.9(ii) shows a binary hologram to generate a +1 diffracted order beam with amplitude profile $\cos(\varphi(x, y))$, where $\varphi(x, y)$ represents the azimuthal angle in the beam cross-section. The binary hologram incorporates a net tilt of $10\sqrt{2}\pi$ across the hologram plane, with $\tau_x = 10\pi$, $\tau_y = 10\pi$ and uses $\phi_b(x, y) = 0$. The computed diffraction pattern in the Fourier plane is shown in figure 3.9(iii) and the focal spot of the +1 order beam is seen in the inset.

The quantity $|b_{+1}|^2$ represents the relative intensity in the +1 diffracted order beam. Considering the +1 order beam to have uniform amplitude the light efficiency

in the +1 order is $\left({}^{\sin^4(\frac{\alpha}{2})}/_{\pi^2}\right) \times 100\%$. Thus the maximum achievable light efficiency is ${}^{1}/_{\pi^2} \times 100\%$, which also represents the diffraction efficiency of the +1 order beam corresponding to the binary hologram discussed in section 3.4.1. The diffraction efficiency can be increased by implementing binary phase hologram, in which case $T_{bh}(x, y) \times \pi$ represents the binary phase delay to be introduced by the hologram at (x, y). The amplitude profile in the +1 diffracted order beam of the binary phase hologram, calculated by performing the Fourier series analysis in a similar manner, is found to be $b_{+1}(x, y) = \frac{2}{i\pi} \sin^2 \frac{\alpha^2(x,y)}{2}$. Thus, in the case of binary phase hologram, the diffraction efficiency for a uniform amplitude +1 diffracted order beam becomes $\left({}^{4\sin^4(\frac{\alpha}{2})}/_{\pi^2}\right) \times 100\%$. In this thesis, we use binary amplitude hologram for the generation of a beam with a user-defined complex amplitude profile. However, it will be routine practice to employ binary phase hologram in the same scheme.

The scheme above generates a beam with a user-defined complex amplitude profile for a given polarization state. One can coherently combine two such independently controllable complex amplitude profiles with orthogonal polarization states to realize an arbitrary vector beam.

3.5 Generation of arbitrary vector beam using computer generated holography

An arbitrary vector beam corresponds to a beam that has a user-defined complex amplitude as well as polarization profile over the cross-section of the beam. A

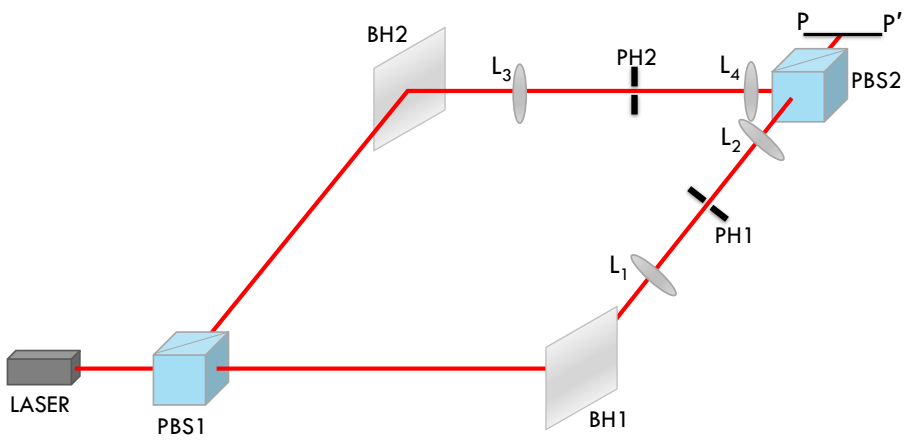

Figure 3.10: Schematic diagram of a basic optical arrangement to generate an arbitrary vector beam.

linearly polarized beam incident on the binary hologram, constructed using the methods described in the section 3.4, will give rise to a linearly polarized user-defined complex amplitude profile in the pupil plane. An optical arrangement, that performs the coherent addition of such two mutually orthogonally polarized beams, can be used to generate an arbitrary vector beam [34, 36, 76]. Figure 3.10 shows the schematic diagram of a basic optical arrangement to generate an arbitrary vector beam. A collimated laser beam is divided into two beams with mutually orthogonal polarization states using a polarizing beam splitter PBS1. Initial polarization of the laser beam is set to be at 45^o with respect to the plane of incidence at the PBS1, such that the reflected s-polarized or vertically polarized beam and the transmitted p-polarized or horizontally polarized beam have equal intensities. The p-polarized beam illuminates the display panel of an LCSLM, where a binary hologram BH1 is written. The binary hologram BH1 is computed in such a way that the +1 diffracted order beam represents the complex amplitude profile corresponding to the X polarized pupil plane (i.e. X component of the pupil plane) of the vector beam to be generated. The beam is then focused by a lens L_1 onto an iris diaphragm ID1 to isolate from other orders. The beam is again collimated using a lens L_2 to be incident on another polarizing beam splitter PBS2. Similarly, the s-polarized beam illuminates another LCSLM displaying a binary hologram BH2, where the respective +1 diffracted order beam represents the complex amplitude profile corresponding to Y polarized pupil plane (i.e. Y component of the pupil plane) of the said vector beam. The beam is then isolated from other orders using a lens L_3 and an iris diaphragm ID2. A lens L_4 is used to re-collimate the +1 diffracted order beam to be incident on PBS2. The LCSLMs are oriented in such a way that both the +1 diffracted order beams have polarizations same as that of the beams incident on the respective binary holograms. Therefore, the two +1 diffracted beams generate the X polarized and Y polarized pupil planes corresponding to the vector beam to be generated. The p-polarized +1 order beam is transmitted by PBS2 while the s-polarized +1 order beam is reflected by PBS2 so that the desired vector beam is realized in the pupil plane PP', which is optically conjugate to each of the hologram planes.

The similar scheme as above can also generate vector beams, where the LCSLMs are replaced by other devices that can implement binary holograms or by phase plates on which the patterns corresponding to the binary holograms can be etched.

3.6 Conclusion

In this chapter, we have introduced the computer generated holography technique. It has also provided a brief discussion on liquid crystal spatial light modulators and how they can be used to implement the computer generated holography technique. We have elaborated on the algorithms adopted to compute the transmittance function of the hologram in accordance with the interference between a reference beam and a user-defined object beam. The technique has been developed to generate scalar beams and vector beams with arbitrary and user-defined complex amplitude profiles, that can be implemented in real time using nematic or ferroelectric liquid crystal spatial light modulators.

* * *

Chapter 4

Development of a Division of Wavefront-based Setup for the Generation of Arbitrary Vector Beams

4.1 Introduction

In the chapter 2, we already discussed the importance of a robust and dynamic vector beam forming scheme. This chapter starts with a detailed discussion on the existing techniques for the generation of arbitrary vector beams followed by the introduction of our proposed liquid crystal spatial light modulator based scheme. It then presents the experimental results to demonstrate the working of the proposed vector beam forming setup. The chapter also describes the displacement theorem used to record the three-dimensional focal volume intensity distribution due to a user-defined beam without the use of any translation stage. It concludes presenting the three-dimensional focal volume intensity distributions to demonstrate the ability of the vector beam forming setup to have dynamic control over the phase as well as polarization profile of the beam.

4.2 Existing schemes for the Generation of Arbitrary Vector Beams

There has been an increasing interest in the last few decades on the vectors beams particularly on the cylindrical vector beams [77]. The cylindrical vector beams, as already mentioned, have spatially varying polarization profile with cylindrical symmetry with respect to the optical axis. The radially polarized beam and azimuthally

polarized beam are two most popular members of the cylindrical vector beam. A radially polarized beam is a beam with cylindrically symmetric polarization profile with the polarization at every point in the beam cross-section oriented in the radial direction. An azimuthally polarized beam on the other hand has cylindrically symmetric polarization profile with the polarization at every point in the beam cross-section oriented in the azimuthal direction. There are a number of ways how such vector beams can be generated. The Radially or azimuthally polarized beam can be generated by the coherent addition of the two orthogonally polarized TEM_{01} modes either inside the laser resonator [78], or outside the laser using an interferometric technique [79]. The two beams can also be generated by passing a linearly polarized beam through a liquid crystal based [80, 81] or multiple half-wave plates based [82] polarization converter. One can also produce a radially polarized beam by modifying the laser cavity using a conical Brewster prism (consisting of convex and concave conical prisms) [83]. Moreover the radially or azimuthally polarized beam can be generated by combining a left and a right circularly polarized beam passing through a helical phase mask [84]. However, these techniques are useful for the generation of only a specific type of vector beam. Thus, for applications involving switching between various vector beams or requiring the implementation of target-specific phase profiles into a vector beam, it is essential to have dynamic control over the amplitude, phase, and polarization profile of the light beam used. Most of the arbitrary vector beam forming schemes facilitating the dynamic control on the beam profile exploit the programmability of LCSLMs such as the setup described in the section 3.5 of the previous chapter. Several LCSLM based techniques to achieve dynamic control over the vector beam, requires the beam to incident on two [76], or three [85] LCSLMs. Some schemes also use single LCSLM by facilitating the light beam to incident on the same LCSLM twice [36, 86], using a grating in conjunction with the LCSLM [87], or making use of a Wollaston prism to split the beam incident on the LCSLM into two orthogonally polarized beams [34, 35].

Though the LCSLM based arbitrary vector beam forming schemes can very well exploit the flexibility offered by the LCSLM device, they are subjected to the limitation set by the damage threshold for maximum power that can be incident on the device [37]. Therefore, considering the availability of accessible high-power laser sources, the maximum power in the generated vector beam using an LCSLM based setup is rather decided by how efficiently the setup utilizes the damage threshold of the LCSLM device.

In this chapter, we introduce a division of a wavefront-based scheme to generate an arbitrary vector beam using a single LCSLM. In our proposed setup, the same wavefront is incident parallelly on the two holograms displayed on the LCSLM. The proposed scheme facilitates the generation of high average-power arbitrary vector beam by efficiently utilizing the LCSLM damage threshold. We demonstrate the working of the vector beam forming scheme by generating radially polarized, azimuthally polarized, and Bessel-Gauss beams.

4.3 Experimental arrangement of the vector beam forming scheme

The schematic diagram of the experimental arrangement to implement our scheme to generate an arbitrary vector beam is shown in figure 4.1. Here we use the twisted-nematic LCSLM to implement the binary hologram. The laser beam from a He-Ne laser ($\lambda = 632.8nm$) is focused by a lens L_1 onto a pinhole PH such that only central part of the focused beam is transmitted by the PH. The diverging beam is then collimated using the lens L_2 to produce an enlarged collimated beam. This beam then illuminates the TNLCSLM display panel on which two binary holograms computed using a LabVIEW program running in a PC are displayed. The two holograms written side by side on the display panel receive two spatially separated parts of the same incident wavefront, as shown in the inset of the figure 4.1. The hologram on the left (say Hologram-A) is designed using the steps described in the section 3.4.2 to generate the complex amplitude profile in the respective +1 diffracted order corresponding to the X polarized (also p-polarized or horizontally polarized) pupil plane of the vector beam. In a similar manner, the hologram on the right (say Hologram-B) is designed to generate the complex amplitude profile corresponding to the Y polarized (also s-polarized or vertically polarized) pupil plane of the said vector beam. The diffracted beams, including the +1 orders emerging from the two holograms, are focused by the lens L_3 onto the iris diaphragm ID. The polarization of the incident beam and the orientation of the LCSLM are arranged in such a way that both the diffracted beams are s-polarized. The iris diaphragm isolates the two +1 order beams from the other orders. The isolated +1 diffracted order beams are then recollimated using the lens L_4. A polarizer Pol is optionally placed in the beam path to ensure that the two +1 diffracted beams are indeed s-polarized. The two

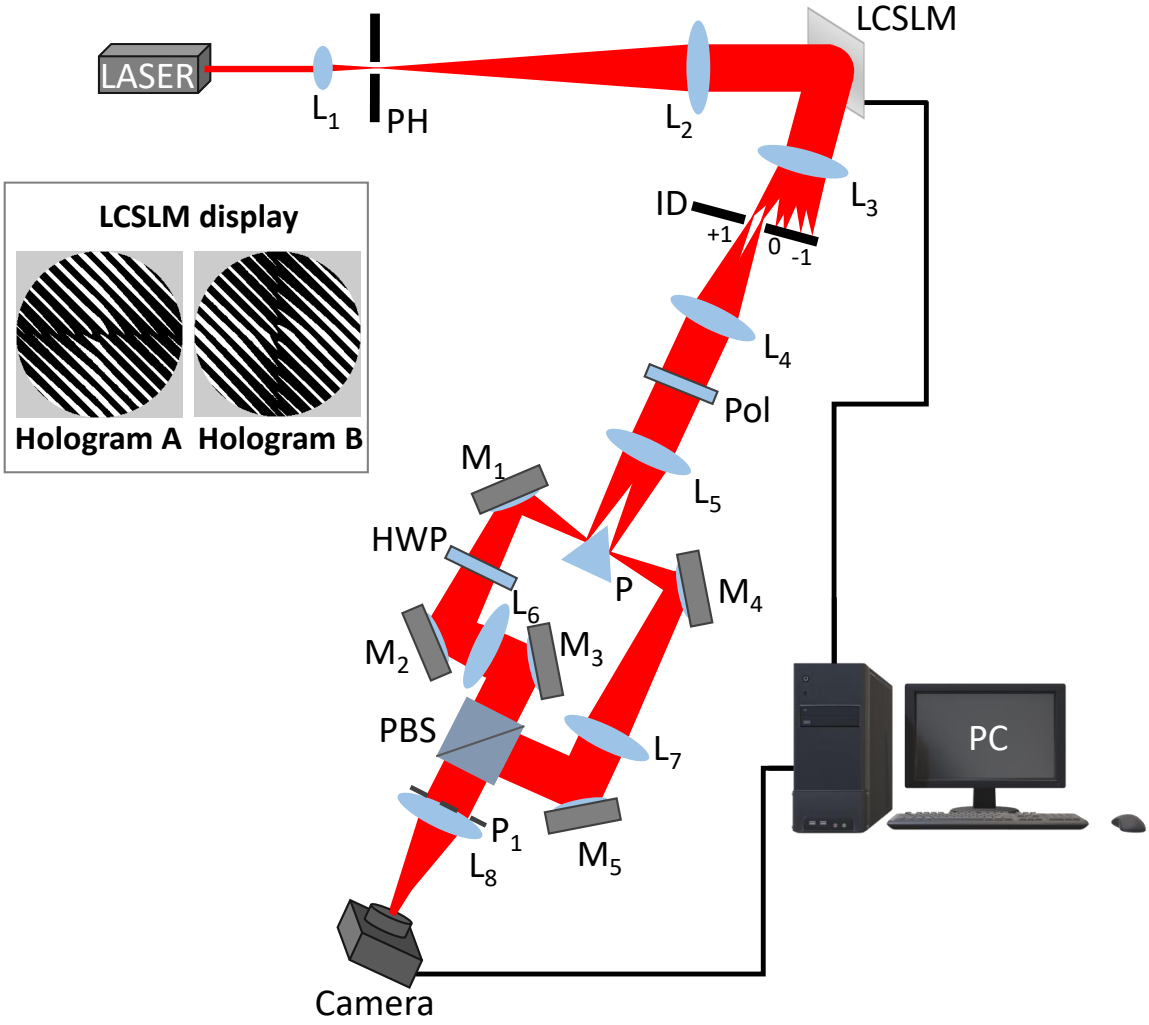

Figure 4.1: Schematic diagram of the experimental setup to implement arbitrary vector beam formation. The inset shows the two holograms displayed adjacent to one another on the LCSLM display panel.

collimated diffracted order beams are focused onto a right-angled prism P using the lens L_5. While designing the holograms, the tilt functions added to the phase profiles are so chosen that the +1 diffracted order beam from hologram-A, after reflection from P, travels towards the mirror M_1 and that from hologram-B travels towards the mirror M_4. The beam reflected from M_1 then passes through a half-wave plate HWP to undergo 90^o polarization rotation to p-polarization state, before getting reflected from the mirror M_2. The beam is then collimated by the lens L_6, and the collimated beam is reflected by the mirror M_3 to be incident on the polarizing beam-splitter PBS. The beam being p-polarized is transmitted by the PBS to enter the entrance pupil plane P_1 of the lens L_8. The other +1 diffracted order beam

reflected by the mirror M_2 is then collimated using the lens L_7 and is then reflected by the mirror M_5 to be incident on the PBS. As the beam remains as s-polarized, it gets reflected by the PBS to enter the pupil plane P_1. The optical paths traveled by the two +1 diffracted order beams till they reach the PBS are kept approximately equal so that both the beams remain mutually coherent. Lenses L_3 and L_4, L_5 and L_6, and L_5 and L_7 constitute three $4f$ relay systems, so that the LCSLM display panel and the entrance pupil P_1 are the conjugate planes. The distances PM_1 and PM_2 are kept as small as possible and approximately equal to one another, so that the respective beams are affected by external disturbances in a more or less similar manner. Further, the inclinations of the mirrors ($M_1 \rightarrow M_5$) and of the PBS are adjusted to ensure that the two +1 diffracted order beam cross-sections are parallel to the plane P_1. Therefore, the plane P_1 contains the X polarized and the Y polarized pupil realized in the +1 diffracted order beams from hologram-A and hologram-B, respectively, thereby constituting the pupil plane of the user-defined vector beam. To be noted that the two orthogonally polarized pupil planes correspond to two spatially separated parts of the same beam incident on the LCSLM. Thus, taking a cue from the two-beam interference phenomenon, the proposed scheme is referred to as the division of wavefront-based scheme. In order to record the focal spot, the generated vector beam is then focused onto the CMOS camera connected to the PC using the lens L_8.

4.3.1 Power of the generated vector beam

As already stated the proposed setup has the advantage of generating relatively high average-power vector beams compared to the other LCSLM based vector beam forming schemes. Considering a beam with uniform amplitude over the beam cross-section and of sufficient power incident on the LCSLM, each hologram can receive maximum possible power decided by the damage threshold of the LCSLM device. Let us consider that each hologram can receive a maximum of P number of photons and e_1 is the diffraction efficiency in the +1 diffracted order (that is e_1 fraction of the incident light on each hologram is diffracted into the corresponding +1 order). Thus the generated vector beam will have $2e_1P$ photons, assuming no further loss of light in the setup and the optical components, other than the LCSLM, have damage threshold high enough not to affect the maximum number of photons in the +1 order beams. In setups involving two consecutive LCSLMs or in a double-pass arrange-

ment of a single LCSLM displaying two holograms, the net number of photons in the resultant beam cannot reach the value of $2e_1P$ even if the area of each hologram is doubled (which may be possible when an LCSLM displays only one hologram). This is because here the resultant vector beam originates from a beam, incident on the second hologram, which itself is either the +1 or the 0 order beam diffracted by the first hologram. After each diffraction, if e_1 fraction of the incident beam goes to the +1 order, a fraction of $< (1 - 2e_1)$ goes to the 0 order, because of some light going into the other orders. Thus, the damage threshold of the second LCSLM or part of the LCSLM displaying the second hologram cannot be fully exploited. On the other hand the use of any beam-splitting device to obtain two incident beams on the LCSLM imposes additional complexities into the setup. For instance, the Wollaston prism in the case of references [34, 35] has a relatively low damage threshold, which is less than the typical damage threshold of the LCSLM. Another benefit of the proposed setup is that it does not utilize any beam-splitting element in front of the LCSLM plane, thereby avoiding any additional source of aberration introduced into the beam. Therefore, it is easier to ensure that two identical complex amplitude profiles are incident on the two holograms.

4.3.2 Results and discussions

We have demonstrated the working of our vector beam forming setup first by generating the azimuthally polarized and the radially polarized beams. As mentioned earlier, the desired vector beam is generated by overlapping an X polarized pupil and a Y polarized pupil of appropriate amplitude profiles. The amplitude profiles of the pupil planes represent the electric field vector components in the entrance pupil of the given vector beam. In case of an azimuthally polarized beam, the electric field vector in the pupil plane can be written using Jones matrix representation as

$$\begin{pmatrix} -\sin\varphi \\ \cos\varphi \end{pmatrix},$$

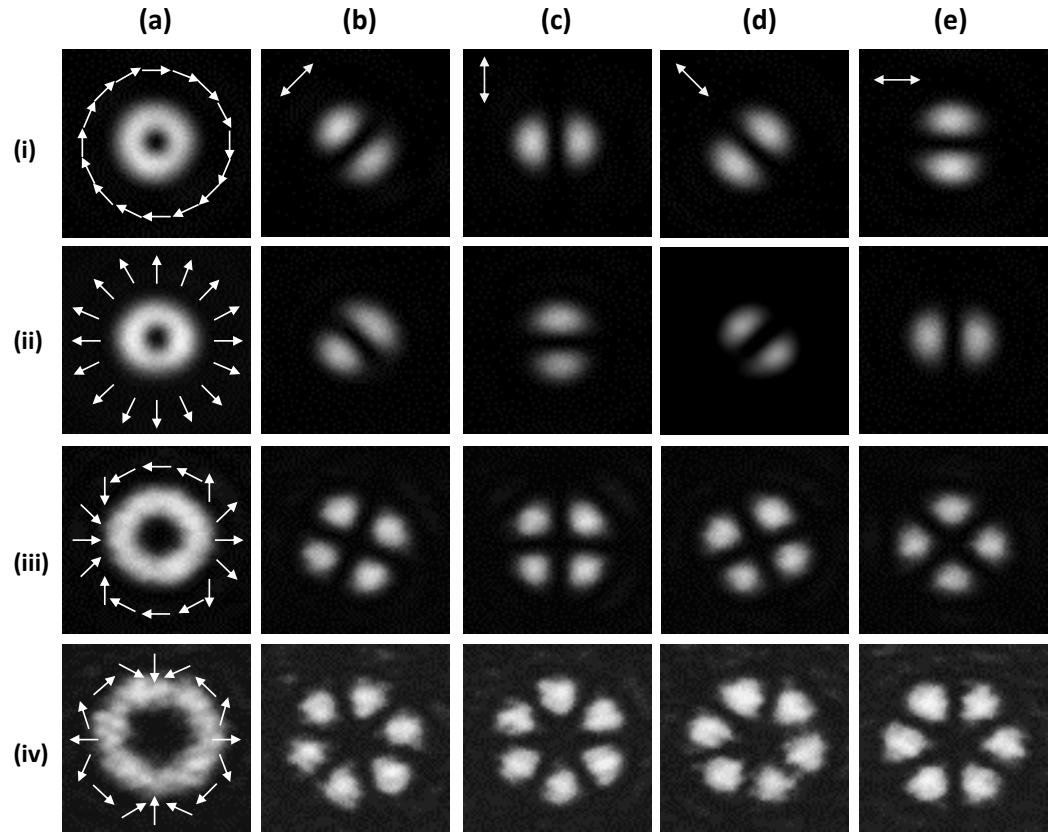

Figure 4.2: Experimental images representing the XY plane (at the nominal focus of the lens) intensity distribution of a focused (i) azimuthally polarized, (ii) radially polarized, vector-vortex Bessel-Gauss beam with topological charge (iii) $n = 2$ and (iv) $n = 3$, (a) without polarizer (the arrows over the images shows the spatially varying polarization profile corresponding to each beam), (b $\rightarrow$ e) with a polarizer whose axis of orientation is indicated by the double arrow shown at the top of each image in row (i). The intensity distribution is over an area of dimension $382\mu m \times 382\mu m$.

where, φ is the azimuthal angle in the pupil plane. The two holograms, such as shown in the inset of figure 4.1, are constructed using the scheme described in section 3.4.2. Each hologram is described over a circular area of a diameter equal to 512 LCSLM pixels. The arrangement of lenses in the beam path between the LCSLM plane and the lens L_8 provides a beam diameter of $3.4mm$ at the entrance pupil P_1 of L_8. The focal length of L_8 is taken to be $300mm$ so that the effective NA of the lens focusing the generated vector beam is 0.0056. Therefore, the experimental arrangement corresponds to low NA focusing of the beam. We record the intensity distribution in the nominal focal plane first for an unabberated azimuthally polarized beam. The intensity distribution, without any polarizer in front of the CMOS camera, has a doughnut-like structure. We then introduce a polarizer in front of the

camera and captured images for four different orientations of the polarizer. Figure 4.2(i)(a) shows the intensity distribution in the focal plane without the polarizer, while figures 4.2(i)(b→e) show the focal plane intensity distributions for four different polarizer orientations indicated by the double arrow at the top-left corner of each image. We then modify the two holograms to generate a radially polarized beam. The electric field vector orientation in the pupil plane for a radially polarized beam can be written using Jones matrix representation as

$$\begin{pmatrix} \cos\varphi \\ \sin\varphi \end{pmatrix}.$$

The two representative holograms used to generate the two pupil planes of a radially polarized beam are shown in figure 4.3(a). The recorded intensity distribution in the nominal focal plane for an unabberated radially polarized beam is shown in figure 4.2(ii)(a). It is to be noted that owing to the low NA focusing, the intensity patterns in the focal plane for both the radially and azimuthally polarized beams appear similar when no polarizer is used in front of the camera. Figures 4.2(ii)(b→e) show the focal plane intensity distributions of a radially polarized beam for four different orientations of the polarizer. To demonstrate the capability of the proposed vector beam forming setup, we also generate vector-vortex Bessel-Gauss beams [88, 89] with two different topological charges. The Jones matrix representation of a vector-

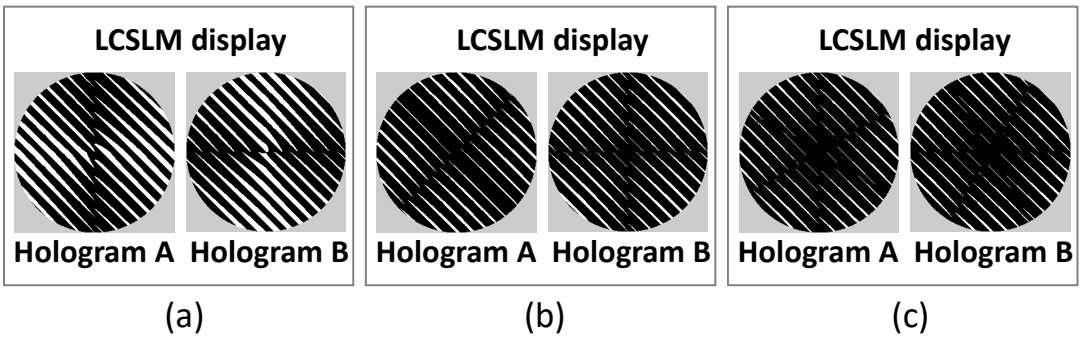

Figure 4.3: The two representative holograms displayed on the LCSLM to generate the two pupil planes for a (a) radially polarized beam, (b) vector-vortex Bessel-Gauss beam with topological charge $n = 2$, and (c) with topological charge $n = 3$.

vortex Bessel-Gauss beam with a topological charge of n is given as

$$J_n(\beta r)\begin{pmatrix}\cos\varphi\\ \sin\varphi\end{pmatrix},$$

where, J_n is the n-order Bessel function of the first kind and β is a constant that determines the beam profile. The two representative holograms constructed to generate the two pupil planes corresponding to the vector-vortex Bessel-Gauss beam with topological charge $n = 2$ and topological charge $n = 3$ are shown in figures 4.3(b) and 4.3(c), respectively. The recorded intensity distributions in the focal plane without and with the polarizer in front of the CMOS are shown in figure 4.2(iii) with topological charge $n = 2$ and in figure 4.2(iv) with topological charge $n = 3$. The orientation of the electric field vectors in the pupil plane of each of the vector beams considered is shown in figure 4.2 (a). The images in figures 4.2(i $\rightarrow$ iv) demonstrate the capability of the proposed scheme to generate various types of vector beams. However, owing to the limited number of pixels in the LCSLM to describe the holograms, the patterns in figure 4.2 (iii) and (iv)(a) do not appear to have a perfect circular symmetry.

4.4 Generation of vector beams with arbitrary phase profiles

The vector beam forming scheme is also capable of precise incorporation of a user-defined phase profile into the generated vector beam. To demonstrate this, we refer to the theoretical work [90] that predicted the generation of a boat-shaped intensity distribution near the focus of an azimuthally polarized beam aberrated with a moderate amount of coma. It is observed that the three-dimensional focal volume of the boat-shaped beam comprises a dark center surrounded by light from five directions. The beam is expected to be useful in manipulation of trapped particles.

In order to record the three dimensional intensity distribution near the focus we first need to record the intensity distributions in different planes along the axis. Therefore this requires a mechanism to move the camera plane. However owing to the low NA focusing condition, we make use of the displacement theorem to record axially shifted intensity distribution of the vector beam generated without the need to physically shift the camera plane. Below we discuss about the effective shift of

the focal plane using the displacement theorem.

4.4.1 Displacement theorem to record focal volume intensity distribution

Under paraxial approximation, the addition of a certain amount of defocus to an incident light beam results in no change in the focal intensity distribution other than an axial shift of the focal plane [50]. Let us consider that ϕ is the phase in a beam focused by a lens under paraxial approximation and $I(u, v, \Upsilon)$ is the normalized intensity at the location $P(u, v, \Upsilon)$ near the focus.

Considering f as the focal length of the lens, a as the radius of the lens aperture and λ as the wavelength of the incident light, the expression of the normalized optical coordinates (u, v) can be rewritten as

$$u = k\left(\frac{a}{f}\right)^2 z, \tag{4.1}$$

$$\text{and} \quad v = k\left(\frac{a}{f}\right) r, \tag{4.2}$$

where, $r = \sqrt{x^2 + y^2}$, (x, y, z) are the Cartesian coordinates with origin at the focus, Υ is the azimuthal angle, and $k = \frac{2\pi}{\lambda}$. The normalized intensity $I(u, v, \Upsilon)$ at point P using the diffraction integral [50] is given as

$$I(u, v, \Upsilon) = \frac{1}{\pi^2}\left|\int_0^1 \int_0^{2\pi} e^{if(u,v\Upsilon;\rho,\theta)} \rho \, d\rho \, d\theta\right|^2. \tag{4.3}$$

where,

$$f(u, v, \Upsilon; \rho, \theta) = k\phi - v\rho\cos(\theta - \Upsilon) - \frac{1}{2}u\rho^2 \tag{4.4}$$

Here (ρ, θ) are the polar coordinates in the lens aperture with ρ as the normalized radial coordinate. The intensity is normalized with respect to the intensity of a beam with $\phi = 0$. If we modify the phase profile of the incident beam by adding certain amount of defocus so that

$$\phi' = \phi + H\rho^2, \tag{4.5}$$

where, H is the coefficient of defocus (of the order of λ), then the new normalized

intensity is given as

$$I'(u', v', \Upsilon') = \frac{1}{\pi^2} \left| \int_0^1 \int_0^{2\pi} e^{if'(u', v'\Upsilon'; \rho, \theta)} \rho \, d\rho \, d\theta \right|^2, \tag{4.6}$$

where,

$$f'(u', v', \Upsilon'; \rho, \theta) = k\phi' - v'\rho\cos(\theta - \Upsilon') - \frac{1}{2}u'\rho^2. \tag{4.7}$$

Now using equation 4.5, the expression 4.4 can be written as

$$\begin{aligned} f(u, v, \Upsilon; \rho, \theta) &= k(\phi' - H\rho^2) - v\rho\cos(\theta - \Upsilon) - \frac{1}{2}u\rho^2 \\ &= k\phi' - v'\rho\cos(\theta - \Upsilon') - \frac{1}{2}u'\rho^2. \end{aligned} \tag{4.8}$$

Comparing equations 4.4, 4.7, and 4.8, we can write

$$u' = u + 2kH, \qquad v' = v, \qquad \text{and } \Upsilon' = \Upsilon. \tag{4.9}$$

Considering the equations 4.1 and 4.9, the normalized optical coordinate u' is related to the new axial coordinate z' as

$$z' = z + 2\left(\frac{f}{a}\right)^2 H. \tag{4.10}$$

From equations 4.4, 4.7, 4.8, and 4.10, we get

$$I(u, v, \Upsilon) = I'(u', v', \Upsilon') \tag{4.11}$$

Thus the addition of a certain amount of defocus (indicated by H) results in no change in the three-dimensional focal intensity distribution apart from an axial shift as a whole by a distance given as

$$\begin{aligned} \Delta z &= \mid z' - z \mid \\ &= 2\left(\frac{f}{a}\right)^2 H. \end{aligned} \tag{4.12}$$

The focal intensity distribution can be shifted in either direction about the nominal focal plane by an addition or subtraction of a defocus term to the phase profile. Let W be a wavefront incident on a low numerical aperture (NA) lens which is focused

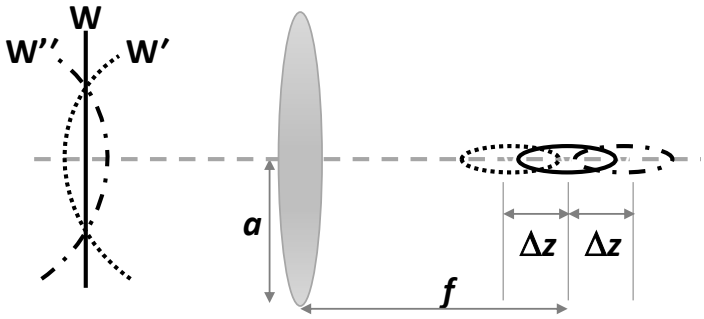

Figure 4.4: Schematic showing the axial shift of the focal volume intensity distribution around the focal plane using the displacement theorem.

to an ellipsoid as shown in figure 4.4. W gets modified to W' and W" after the addition and subtraction of the defocus term. According to displacement theorem, the focal intensity distributions in the case of W' and W" will get shifted axially towards the lens or away from the lens resulting in the ellipsoids with the dotted and the dash-dotted lines as seen in figure 4.4. Therefore, it is possible to record the transverse intensity distribution at a different plane of the focal volume even with a fixed detector plane.

4.4.2 Experimental demonstration of the boat shaped beam

Here we experimentally demonstrate the precise incorporation of a phase profile into the generated vector beam by generating the boat-shaped intensity distribution near the focus of an azimuthally polarized beam aberrated with a moderate amount of coma [90]. In order to generate the boat-shaped beam using the setup, the two holograms are modified to incorporate RMS 1 radian of Z_8 (i.e. primary x-coma) to each of the X polarized and Y polarized pupil planes of the azimuthally polarized beam. We use the displacement theorem described in section 4.4.1 to shift the focal intensity distribution axially with a reasonable accuracy. For our setup, we have found that the incorporation of Z_4 (i.e. defocus) of RMS amplitude equal to ± 0.0043 (say ΔZ_4) radian into the beam leads to an axial shift of the focal intensity distribution by a distance of $\pm 935 \mu m$. Thus, keeping the CMOS camera static at the nominal focus of L_8, as different amount of defocus is incorporated into the beam, the same camera will record different axial planes of the three-dimensional focal intensity distribution, relative to the beam with zero defocus. Here we use normalized optical coordinates $(v,\ u)$ to represent the distance r in

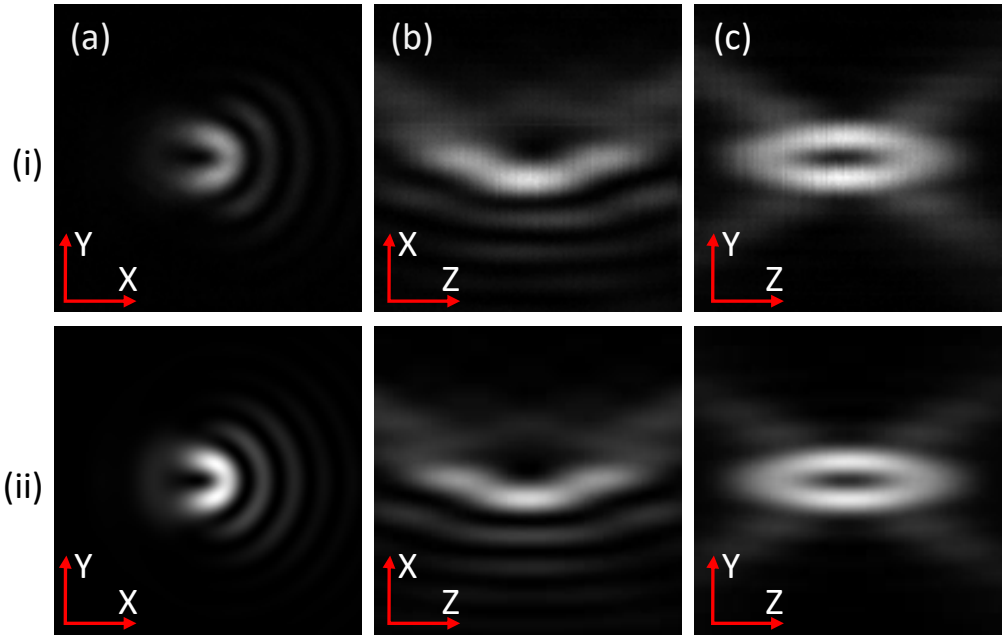

Figure 4.5: (i) Experimental images of the (a) XY, (b) XZ and (c) YZ plane intensity distributions, all passing through the nominal focus, due to azimuthally polarized beam aberrated with 1 radian RMS of primary x-coma. Images in (ii) (a), (b) and (c) show the corresponding intensity distributions obtained theoretically. The XY plane intensity distributions are over an area of dimension $(\Delta X, \Delta Y) = (38v, 38v)$, while the XZ and YZ planes are over an area of dimension $(\Delta v, \Delta u) = (38, 38)$.

the XY plane and the axial separation z. We then incorporate varying amounts of Z_4 into the comatically aberrated azimuthally polarized beam and for each value, capture the XY plane intensity using the CMOS camera. We thereby obtain a stack of XY planes corresponding to different axial distances. We choose the increment in Z_4 for two consecutive axial planes to be equal to $\Delta Z_4 = 0.0043$ radian, such that the distance between two adjacent camera pixels (equal to $5.3\mu m$) expressed in v unit becomes equal to the distance between two axial planes expressed in u unit. Figure 4.5(i) shows the experimentally obtained intensity distributions in the (a)XY, (b) XZ, and (c) YZ planes of an azimuthally polarized beam aberrated with primary x-coma of RMS 1 radian. All the planes shown pass through the nominal focus. The XY plane intensity distribution is over an area of dimension $(\Delta X, \Delta Y) = (38v, 38v)$, while the XZ and YZ plane intensity distributions are over an area of dimension $(\Delta v, \Delta u) = (38, 38)$, with each plane comprising 128×128 pixels. We also perform numerical simulations to generate the intensity distributions of the boat-shaped beam using the Fourier transform form of the vectorial diffraction

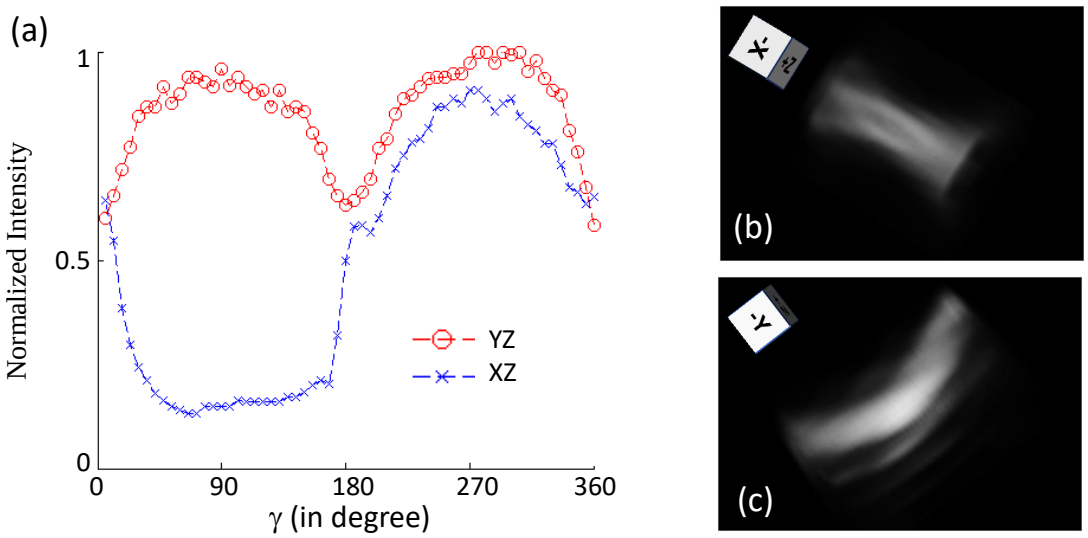

Figure 4.6: Plots of the maximum intensity along a radius making an angle γ with the horizontal axis versus the angle γ, for the XZ and YZ plane intensity distributions obtained experimentally. (b) and (c) show two different projections (as indicated in the top-left corner) of the three-dimensional rendering of the intensity distribution in the focal volume.

theory [91, 92]. Figure 4.5(ii) shows the numerically obtained intensity distributions in the (a)XY, (b) XZ, and (c) YZ planes, equivalent to the experimental images in figure 4.5(ii). It can thus be seen that the experimentally obtained images are very much agreement with the numerically obtained images. Figure 4.6(a) shows two overlapped plots corresponding to the experimentally obtained XZ plane and YZ plane intensity distributions (each normalized by the maximum of the two intensity distributions) as in figures 4.2(i) (b) and (c). Each plot shows the maximum intensity along a line making an angle γ with the horizontal direction. From figure 4.6(a) it can be seen that the dark center of the focal intensity distribution is effectively surrounded by intense light in all but one direction. We then make use of the stack of the XY planes captured by the camera to digitally construct a three-dimensional intensity distribution of the focal volume. Figures 4.6(b) and (c) show two different two-dimensional projections of a three-dimensional rendering of the focal intensity distribution which further confirm the experimental generation of the boat-shaped beam, where the projection directions are indicated at the top-left corner of each image.

4.5 Conclusion

In this chapter, we have introduced a division of wavefront-based scheme using a single liquid crystal spatial light modulator to generate an arbitrary vector beam. We have demonstrated the working of the proposed scheme by generating a few important vector beams, including the radially polarized beam and the azimuthally polarized beam. The generation of the specific vector beam has been confirmed from the focused intensity distributions for different orientations of the polarizer placed in front of the camera. We also had a brief discussion on the displacement theorem that enables the shifting of the focal volume intensity distribution in the axial direction under low NA focusing condition by incorporating defocus into the beam. We have demonstrated the successful implementation of the displacement theorem by recoding the three-dimensional intensity distribution of a boat-shaped beam. The generation of the boat-shaped beam has validated the capability of the proposed scheme for the incorporation of precise phase control of the generated vector beam.

* * *

Chapter 5

Development of a laser scanning microscope executing intraframe polarization switching of the illumination beam

5.1 Introduction

In chapter 2 we discussed the polarization switching mechanisms of conventional polarization microscopes and their limitations if a specimen is to be illuminated with two or more different polarizations in quick succession. We also introduced the LCSLM based vector beam forming scheme to generate an arbitrary vector beam. In this chapter we implement this scheme in a laser scanning microscope to modulate the polarization profile of the illumination beam in a dynamic fashion. The chapter begins with a description of the existing techniques used for the polarization modulation of the illumination beam. It then describes the design of the laser scanning microscope using the vector beam forming unit to achieve polarization switching of the illumination beam at the end of each line scanned. Polarization switching can be done via a number of schemes depending on the number of polarized profiles and the manner of switching of the polarization profile to scan the specimen. The chapter concludes by presenting a proof of principle experiment to demonstrate the working of the proposed microscope utilizing two of the schemes to switch the polarization of the illumination beam after each line scanned.

5.2 Existing techniques to switch the polarization of an illumination beam

As mentioned earlier several techniques have been proposed to achieve the polarization switching of the illumination beam in an optical microscope. In the most general case, the state of polarization of a linearly polarized beam can be rotated by changing the orientation of a half-wave plate ($\lambda/2$) placed in the beam path. However such a change in polarization is subjected to the mechanical disturbance owing to the movement of optical components. There are other techniques to switch the polarization state without causing any mechanical disturbance to the optical components, such as using an electro-optic modulator for example a Pockels cell [22, 23, 24], but the polarization modulation by Pockels cell depends on the stability of the voltage applied across the cell and the wavelength of light used. A magneto-optic modulator such as a Faraday rotator [25] can also switch the polarization of a light beam. However, a particular state of polarization achieved by the Faraday rotator depends on the stability of the external magnetic field applied across the rotator. An illumination beam with a two-dimensional polarization profile can also be produced in a microscope, using a universal compensator made up of liquid crystal variable retarders [26, 27, 28, 29]. To be noted that the methods discussed so far employ inter-frame polarization switching, that is, the polarization of the illumination beam is changed at the end of the acquisition of one complete image frame. Such methods thus lead to a delay of at least the acquisition time of one complete image frame in illuminating a particular portion of the specimen with two different polarizations. For accurate extraction of detail information on molecular organization in a specimen which is in a dynamic environment, such kind of delay may create an issue.

There exists a few schemes where the polarization of the illumination beam can be switched after every line scanned [23, 30, 31] such as in a differential polarization microscope [23] although the same is not a point scanning microscope. A photoelastic modulator (PEM) can also be used in a differential polarization microscope or a laser scanning confocal microscope to switch the polarization of the beam after every line [30, 31]. However this mechanism facilitates switching among linear, circular, and elliptical polarization states only and thus not capable of switching between arbitrary polarization states of the illumination beam. The LCSLM based

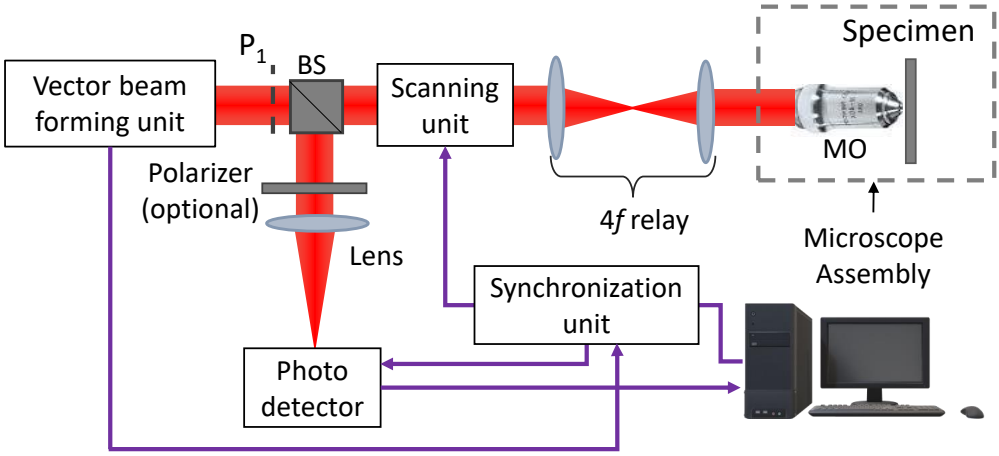

Figure 5.1: Schematic diagram of the laser scanning microscope comprising the vector beam forming unit for illumination beam generation.

schemes discussed in the previous chapter can generate arbitrary vector beams and therefore can permit switching between different vector beam states. However such switching also can take place at the end of each image frame only.

5.3 Experimental arrangement of the laser scanning microscope

The schematic of the proposed laser scanning microscope is shown in figure 5.1. Apart from the optics, it primarily comprises, (i) the division of wavefront-based arbitrary vector beam forming unit, (ii) the scanning unit, (iii) the microscope assembly, (iv) the photo-detector unit along with a DAQ card, and (v) the synchronization unit. For the purpose of quick generation of a particular polarization of a light beam as well as for fast switching between different polarizations, the nematic LCSLM in the vector beam forming setup is replaced with the ferroelectric LCSLM. Thus the two binary holograms, displayed on the FELCSLM, give rise to an illumination beam comprising two orthogonally polarized beams in the plane P_1, each with a user-defined complex amplitude profile as described in section 4.3. Plane P_1 is relayed using a $4f$ relay system via a beam splitter BS to the scanning unit. The scanning unit comprises two moving magnet closed loop galvanometer based scanning mirrors (X scan mirror and Y scan mirror). One $4f$ relay system is used in between the two scan mirrors such that plane P_1 is optically conjugate to each of the mirrors. The beam after the scanning unit is relayed, using another $4f$ system, onto

the entrance pupil of the microscope objective of a microscope assembly (Olympus IX51 inverted microscope). Thus the entrance pupil of the MO is conjugate to the planes of each scan mirrors. The MO focuses the illumination beam onto the specimen plane. The light emerging from the specimen plane is received by the same MO in an epi-illumination mode and which is then descanned by the scanning unit. The beam after the scanning unit is directed towards the BS, and the BS reflects the beam to be received by the photo-detector. A polarizer is optionally placed in front of the photo-detector such that light with only a certain polarization will be received by the photo-detector. A microprocessor based synchronization unit is used to synchronize the operations of the vector beam forming unit, scanning unit, and the DAQ card linked to the photo-detector. The FELCSLM displays the binary patterns derived from a color image in a sequential manner which is exploited to update the binary holograms so as to switch between the polarization states of the illumination beam at regular intervals. Below we discuss the display properties of binary patterns by the FELCSLM.

5.4 Sequential display of bit planes in a color image by FELCSLM

As mentioned in section 3.3.2, ferroelectric LCSLM is capable of reading color images containing 24-bit of information per pixel. The image written on the FELCSLM (often referred to as the color image in this thesis) can be refreshed at the standard video rate of 60Hz. Depending on the active sequence file in the FELCSLM driver board, any incoming color image is interpreted as 24 single-bit images (8 single-bit planes each from red, green, and blue color planes of the color image) in the case of 24-bit sequence file or as 3 single-bit images (where each 8 bit information represented by the colors red, green, and blue, is scaled down to single-bit information) in the case of 3-bit sequence file. These 24 or 3 single-bit images from each color image are then displayed sequentially. The first kind of display is termed 24sb mode, where the 24 single-bit planes corresponding to a color image are divided into three groups, namely, red (R_0, R_1, R_2, ..., R_7), green (G_0, G_1, G_2, ..., G_7), and blue (B_0, B_1, B_2, ..., B_7). The second kind of display is termed 3sb mode, where the three single-bit planes corresponding to a color image are represented by red (R), green (G), and blue (B). A single color image can be constructed in such a way that each

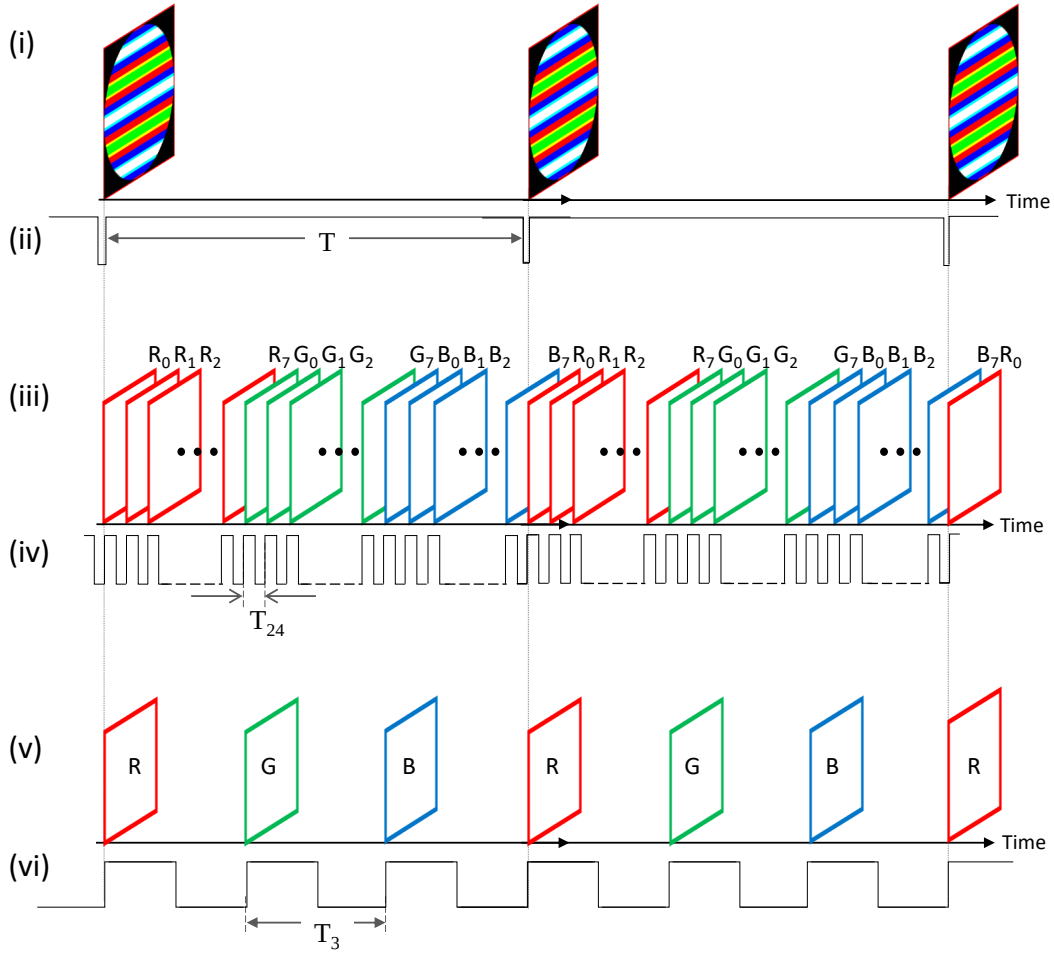

Figure 5.2: (i) A representative color image comprising 24 binary holograms displayed at an interval T and (ii) the display timing of the color image by the FELCSLM. Sequential display of (iii) 24 single-bit planes in the 24sb mode and (v) 3 single-bit planes in the 3sb mode of the FELCSM. The display timing of the single-bit planes are seen in (iv) and (vi) in the case of 24sb mode and 3sb mode, respectively.

of the single-bit planes represents a binary hologram or a pair of binary holograms such as hologram-A and hologram-B, as mentioned in the section 4.3. Depending on the display mode, 24sb mode or 3sb mode, each of the 24 single-bit images or the 3 single-bit images is displayed for a duration equal to $1/24$ or $1/3$ of the net display period (T) of a single color image, respectively. Figure 5.2(i) shows a color image comprising 24 single-bit planes, each representing a binary hologram or a pair of binary holograms, updated after an interval of T (as shown in figure 5.2(ii)). The value of T is $16.67ms$ considering the video rate of $60Hz$. Figure 5.2(iii) depicts the sequential display of bit planes in the 24sb mode of the FELCSLM, where figure 5.2(iv) shows the exact duration of display of individual single-bit planes in the

24sb mode. Figures 5.2(v) and (vi) show the sequential display of single-bit planes and the exact duration of display of individual single-bit planes, respectively, in the 3sb mode of the FELCSLM. Thus, for the color image refresh rate of $60Hz$, the single-bit planes are updated at an interval of $0.69ms$ (T_{24}), in the case of 24sb mode and at an interval of $5.56ms$ (T_3), in the case of 3sb mode. From the plots in figures 5.2(iv) and 5.2(vi), it is observed that in the FELCSLM the user-defined binary hologram and the corresponding negative binary hologram, as stated in section 3.3.2, each is displayed for about half the duration T_{24} in the case of the 24sb mode or T_3 in the case of the 3sb mode. Therefore, the effective display period of the user-defined binary hologram is $T_{24}/2$ or $T_3/2$. Hence, by constructing a sequence of appropriate binary holograms to be written onto the FELCSLM, it is feasible to generate light beams of different polarization states in a time sequential manner. The different user-defined profiles will be available in the plane P_1 at an interval T_{24} or T_3. The FELCSLM provides a reference transistor-transistor logic (TTL) signal that goes high when a given single-bit image is displayed and goes low when the negative of the single-bit image is displayed. This signal is fed to the microprocessor based synchronization unit to generate two trigger pulses for the synchronization of the scanning unit and the DAQ card linked to the photo-detector, with the display of the FELCSLM.

5.5 Schemes for polarization switching at the end of every line scanned

Depending on the number of different polarization profiles of the illumination beam, among which the switching can take place, we describe three schemes for polarization switching. Below we explain the working of the schemes considering the 3sb display mode of the FELCSLM.

5.5.1 Scheme-A

The first kind of polarization switching scheme is termed scheme-A, where the polarization of the illumination beam is switched between two different polarizations (say P1 and P2). These two illumination beam polarizations correspond to the display of the first two single-bit planes of the 3sb display mode of the FELCSLM. For this a color image is constructed such that the first single-bit plane of 3sb display

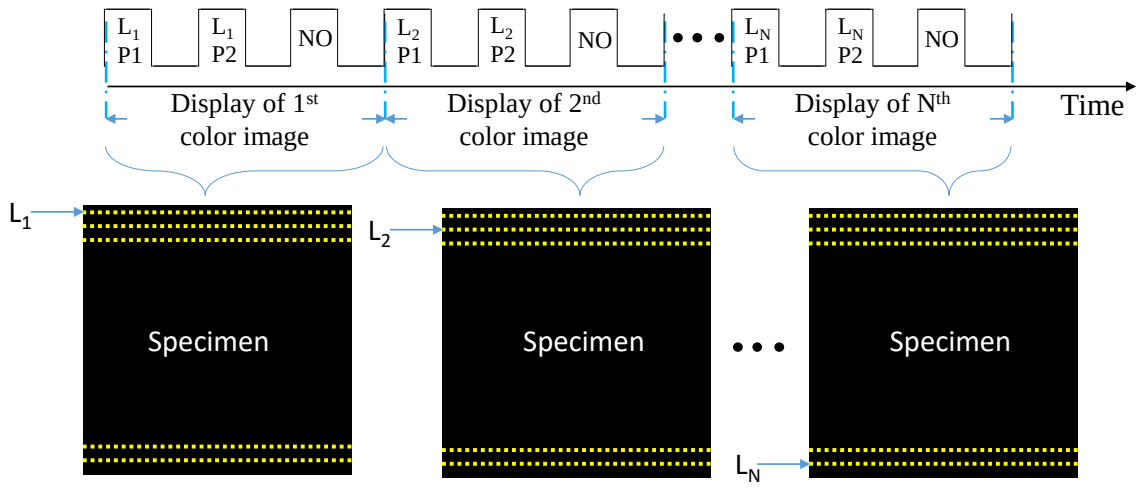

Figure 5.3: Illustratation of the operation of scheme-A to switch between two polarizations P1 and P2 of the illumination beam by displaying N color images to scan an equal number of lines in the image frame.

mode results in the display of a binary hologram or a pair of binary holograms on the FELCSLM that produces the illumination beam of one polarization (P1) in the plane P_1. During the display time, $T_3/2$, of the bit plane, a given line, say the first line of the specimen, is scanned and the resulting data (say comprising N pixel values) from the specimen is collected and stored in the PC. The second single-bit plane results in the illumination beam of another polarization (P2) in the plane P_1. During the display time of the second bit plane also, the X scan mirror scans the same line of the specimen, and the respective data is stored. The third single-bit plane comprises a black image (all pixels are made 0) that generates no illumination beam. At the end of display of the first color image, the scanning unit sets the mirrors to scan the second line and the second color image is displayed resulting in scanning the second line of the specimen using the illumination beam of polarization P1 and P2 corresponding to the display of first and second single-bit planes, respectively. The same color image is displayed repeatedly on the FELCSLM panel for the entire duration of the image frame comprising N rows and N columns. Figure 5.3 depicts the operation of scheme-A with respect to time, where the polarization profile of the illumination beam switches between P1 polarization and P2 polarization. As shown in the figure, during the display of the first color image on the FELCSLM, the scanning unit scans the first line (L_1) of the specimen, each with P1 polarized and P2 polarized illumination beam, that corresponds to the display of first and second bit plane, respectively. Similarly the second color image displayed

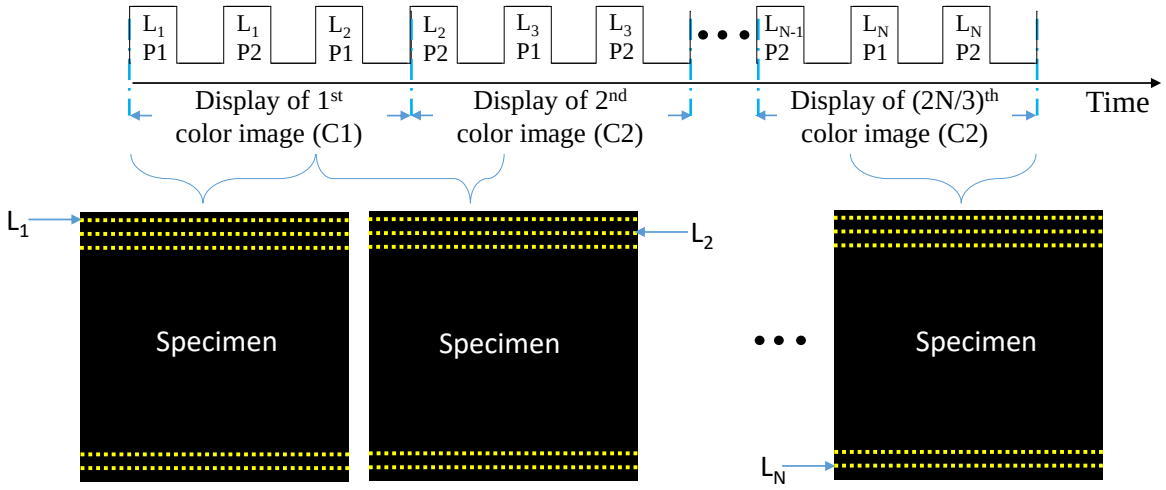

Figure 5.4: Illustratation of the operation of scheme-B to switch between two polarizations P1 and P2 of the illumination beam by displaying two color images C1 and C2 alternatively on the FELCSLM. Considering N to be multiple of 3, the FELCSLM displays 2N/3 color images, consisting of N/3 numbers of C1 and C2 each, to scan an equal number of lines in the image frame.

corresponds to the scanning of the second line (L_2), and the process continues till the display of N^{th} color image to scan the N^{th} line. After the end of the display of N^{th} color image, two digital images of the same specimen corresponding to the two polarization states are constructed simultaneously.

5.5.2 Scheme-B

The second kind of polarization switching scheme is termed scheme-B. Here the illumination beam with two different polarization profiles similar to scheme-A is generated to capture two images of the specimen utilizing all the three single-bit planes of the 3sb display mode of the FELCSLM. Two color images (say C1 and C2) are constructed such that the display of first and third single-bit planes of 3sb display mode corresponding to one color image (C1) and the display of the second single-bit plane corresponding to the color image (C2) produce the illumination beam of polarization P1 in the plane P_1. Similarly, the second single-bit plane corresponding to color image C1 and the first and third single-bit planes corresponding to color image C2 result in the illumination beam of polarization P2 in the plane P_1. These two color images are then displayed repeatedly on the FELCSLM for the entire duration of the image frame comprising N rows and N columns. To begin

with, during the display period of the first and second single-bit planes of one color image (C1) on the FELCSLM, the scanning unit scans the first line of the specimen with illumination beam of polarizations P1 and P2 and for each polarization the corresponding line data (comprising N pixel values each) is stored in the PC. At the end of the display of the second single-bit plane of C1, the scanning unit sets the mirrors to scan the second line of the specimen. During the display period of the third single-bit plane of C1 and the first single-bit plane of the image C2, the scanning unit scans the second line with the illumination beam of polarizations P1 and P2 and for each polarization the corresponding data is stored. The scanning unit then sets the mirrors to scan the third line of the specimen during the display period of second and third single-bit planes of C2. Thus, at the end of the display of two color images (each of C1 and C2), the scanning unit scans three lines of the specimen, each with the illumination beam of polarization P1 and P2. During the acquisition, the FELCSLM keeps displaying the two color images (C1 and C2) alternatively. At the end of the display of the $(2N/3)^{th}$ color image, the scanning unit scans the entire specimen (consisting N number of scan lines) using illumination beam with the two polarizations. The stored data is then used to generate two digital images of the specimen that correspond to two polarization profiles (P1 and P2) of the illumination beam. Figure 5.4 depicts the operation of scheme-B. As shown in the figure, the display of the first two consecutive single-bit planes of 3sb display mode on the FELCSLM corresponds to the scanning of the same line (L_1) of the specimen with P1 polarized and P2 polarized illumination beam. The display of the next two consecutive single-bit planes corresponds to the scanning of the line L_2 of the specimen with the two polarizations. The process continues till the display of $(2N/3)^{th}$ color images (display of N/3 numbers of C1 and C2 each, considering N to be a multiple of 3,) to scan the full image frame using the illumination beam with the two polarizations.

5.5.3 Scheme-C

In scheme-C, the third kind of polarization switching scheme, the polarization of the illumination beam is switched between three different polarization profiles (say P1, P2, and P3). These three illumination beam polarizations correspond to the display of the three single-bit planes of the 3sb display mode of the FELCSLM. A color image is constructed such that the first single-bit plane of 3sb display mode results

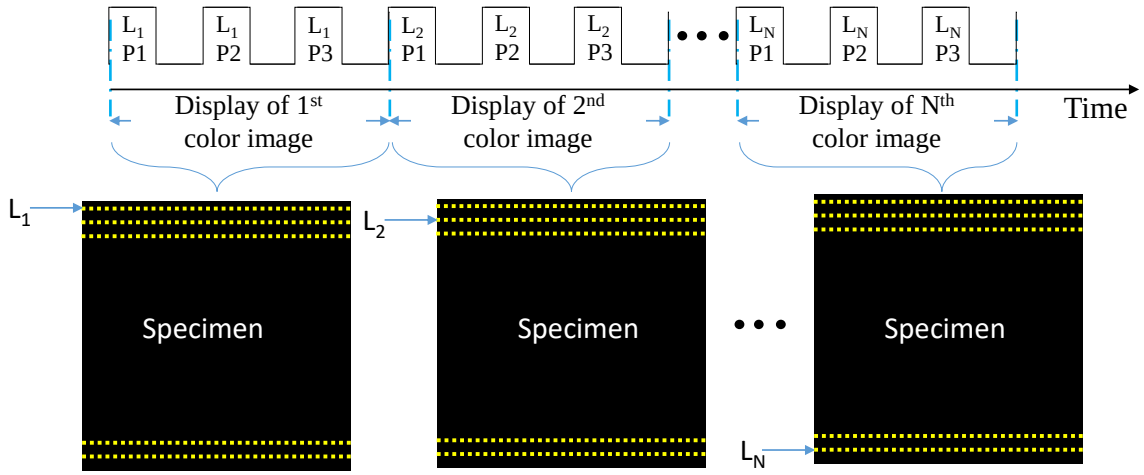

Figure 5.5: Illustratation of the operation of scheme-C to switch between three polarizations P1, P2, and P3 of the illumination beam by displaying N color images to scan an equal number of lines in the image frame.

in a binary hologram or a pair of binary holograms that produces the illumination beam of polarization (P1) in the plane P_1, the second single-bit plane results in the illumination beam of second polarization P2, and the third single-bit plane results in the illumination beam of third polarization P3. The color image is then displayed repeatedly on the FELCSLM for the entire duration of the image frame comprising N rows and N columns. During the display time of the first single-bit plane, the scanning unit scans the first line of the specimen with the P1 polarized illumination beam and the respective data (comprising N pixel values) is stored in the PC. During the display time of the second and third single-bit planes, the scanning unit scans the same line with illumination beam polarizations P2 and P3, respectively. At the end of the display of the first color image, the scanning unit sets the mirrors to scan the next line, and the second color image is displayed, giving rise to the scanning of the second line of the specimen using the illumination beam with three different polarizations. The process continues until the display of N^{th} color image. At the end of the display of the N^{th} color image, the stored data is used to generate three digital images of the specimen that correspond to three different polarization profiles (P1, P2, and P3) of the illumination beam. Figure 5.5 depicts the operation of scheme-C where L_1, L_2 and L_N indicate the first, second and the N^{th} lines scanned.

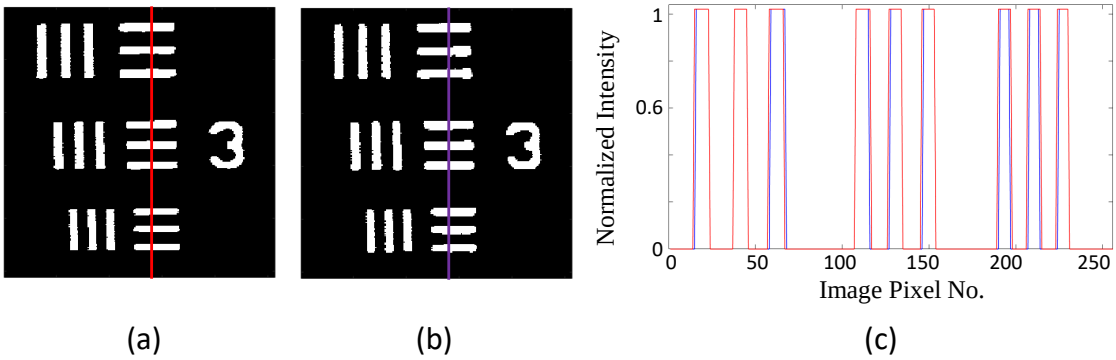

Figure 5.6: Experimental images of a portion of the USAF 1951 test target using (a) X polarized and (b) Y polarized illumination beam. (c) The line plot of normalized intensity against the image pixel number along the lines shown in (a) and (b).

5.6 Experimental results using reflected light and discussions

We demonstrate the implementation of the polarization switching of the illumination beam by employing the laser scanning microscope described in section 5.3. First, we capture images of a portion of the USAF 1951 resolution test target as the specimen using scheme-A to switch between an illumination beam with X and Y polarization states. We use a 0.3 NA and 10× microscope objective (UPLFLN10X2) and a single channel photomultiplier tube (H11462-032) as the photo-detector in conjunction with the NI 6133 DAQ card to perform analog-to-digital conversion of the PMT output. The FELCSLM is operated at the video rate of $60Hz$. Figures 5.6(a) and 5.6(b) show the recorded images of the specimen, illuminated with X polarized and Y polarized illumination beams, respectively. The specimen is scanned over 256×256 pixels covering an area equal to $90\mu m \times 90\mu m$. The plots of normalized intensities against the pixel number for each of the two images, along a line as indicated in the images, are shown in figure 5.6(c). The line plots demonstrate that the two orthogonally polarized beams cover the same regions on the specimen plane on a pixel to pixel basis.

In order to demonstrate the orthogonal polarization properties of the illumination beam for every line scanned, we prepare a polarization sensitive programmable target using the twisted nematic LCSLM. An image resembling the letters “IIT” is written in black on a white background on the TNLCSLM panel, and a square area surrounding the letters is taken as the target. The arrangement of liquid crystal

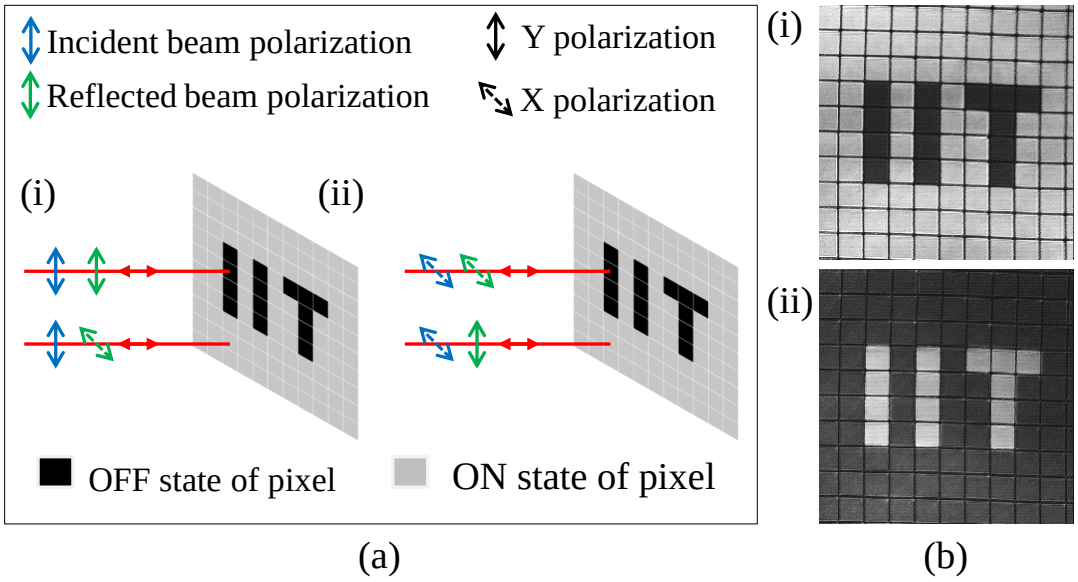

Figure 5.7: Illustration to show the polarization of the reflected beam (green double arrow) from both the ON and OFF state of pixels of a TNLCSLM, when illuminated (blue double arrow) with (i) a Y polarized beam or (ii) an X polarized beam. (b) Experimental images of the TNLCSLM display panel showing the letters "IIT" when the illumination beam is (i) X polarized and (ii) Y polarized. X polarization is represented by dashed double arrows, while the Y polarization is represented by solid double arrows.

molecules in the white or black pixel ensures that the polarization of the reflected light gets rotated by 90^o if the light is incident on the white pixel and the polarization of the reflected light remains unchanged if the light is incident on the black pixel. Therefore we refer to the white pixel as the ON state pixel and to the black pixel as the OFF state pixel. Considering the polarization of the illumination beam to be X polarized, the reflected light becomes Y polarized if the beam is incident on the ON state pixel and remains X polarized if incident on the OFF state pixel. Similarly, when the Y polarized beam is used as an illumination beam, the reflected beam becomes X polarized if the light is incident on the ON state pixel and remains Y polarized if incident on the OFF state pixel. Figures 5.7(a) (i) and (ii) show the polarization of the light reflected (indicated by the green double arrow) from both the ON state and OFF state of pixels, when the polarization of the incident beam (indicated by the blue double arrow) is X polarized and Y polarized, respectively. We insert the optional polarizer in the detection path between the beam splitter and the photo-detector so that the photo-detector receives the Y polarized light only. Therefore, if the illumination beam is X polarized, the letters "IIT" will appear black in white background, and the reverse if the illumination beam is Y polarized.

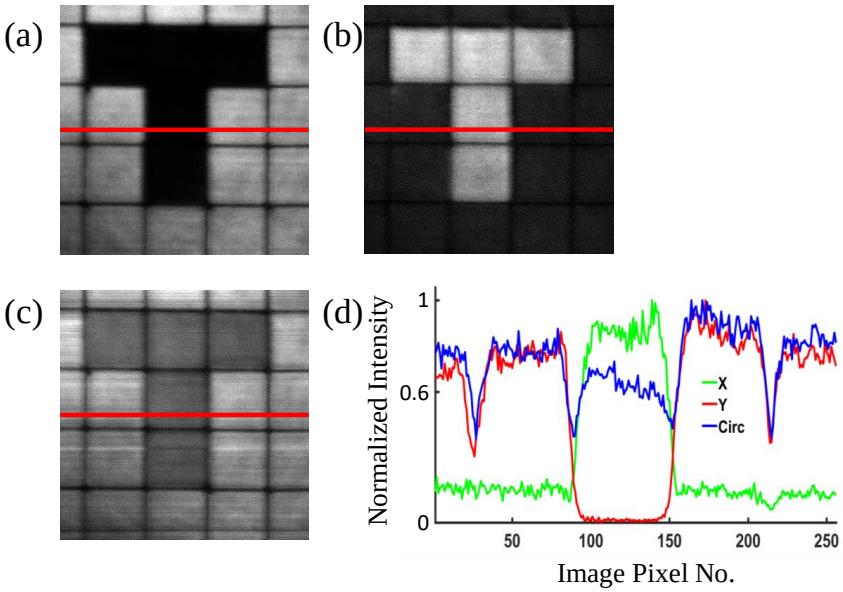

Figure 5.8: Experimental images of the TNLCSLM display panel showing the letter "T" with the illumination beam of (a) X polarization, (b) Y polarization, and, (c) circular polarization using scheme-C polarization switching scheme. (d) The line plot of intensity against the image pixel number along the lines shown in (a), (b), and (c).

Figures 5.7(b) (i) and (ii) show the recorded images of the test target captured when illuminated with the X polarized beam and Y polarized beam, respectively.

We also employ the laser scanning microscope to implement scheme-C of polarization switching between plane polarized along X, plane polarized along Y, and circular polarization states of the illumination beam. Figures 5.8 (a)→(c) show the recorded images of the TNLCSLM display panel showing the letter "T" when illuminated with X polarized beam, Y polarized beam, and circularly polarized beam, respectively. The letter "T" is written on the TNLCSLM display panel in a similar way as the letters "IIT". A line plot against the pixel number for each of the three images, along a line as indicated in the images, is shown in figure 5.8(d). From the line plot, it is seen that both the ON state and OFF state pixel values are nearly equal in magnitudes when the illumination beam is circularly polarized (i.e. the illumination beam has both X and Y polarized light with a phase difference of $\pi/2$ between the two) in contrast with when the beam X or Y polarized.

The results in figures 5.6, 5.7 (b) and 5.8 confirm the capability of the laser scanning microscope employing schemes A and C to perform intraframe polarization switching with a time interval of $5.56ms$ between the arrival of two different polarizations at each pixel. The images with two different polarizations or three

different polarizations are simultaneously available after $4.27s$ in case of scheme-A or scheme-C polarization switching, respectively.

5.7 Conclusion

In this chapter, we have introduced the development of a laser scanning microscope that also has the division of wavefront-based vector beam unit as a part of the illumination beam generation assembly. We have implemented polarization switching of the illumination beam at the end of each line scanned in contrast to at the end of every frame. The polarization modulation of the illumination beam is achieved exploiting the FELCSLM display properties. We have introduced three polarization switching schemes depending on the number of polarization states of the illumination beam and the switching manner. We have presented experimental results to demonstrate the capability of the scanning microscope as well as the implementation of polarization switching schemes to modulate the polarization profile of the illumination beam at the end of each line scanned.

* * *

Chapter 6

Polarization switching of the illumination beam in a scanning confocal microscope in the fluorescence mode

6.1 Introduction

In the previous chapter (i.e. chapter 5), we introduced a laser scanning confocal microscope executing polarization switching of the illumination beam at the end of each line scanned. Experiments were performed with a scanning microscope in the reflection mode. In chapter 2, we discussed the importance of polarization switching of the illumination beam in the field of biological and biomedical sciences where imaging is mostly done in the fluorescence mode. In this chapter, the intraframe polarization switching scheme is implemented in a laser scanning confocal microscope working in the fluorescence mode. The chapter begins with a discussion on the modification in the laser scanning confocal microscope described in the previous chapter to convert it to the fluorescence mode. We implement intraframe polarization switching in the scanning confocal microscope in the fluorescence mode and discuss some issues in the setup owing to the wobbles in the scanning mirrors. The chapter then describes a holographic scanning confocal microscope that can work both in the reflection and fluorescence modes, where the issue of wobbles is taken care of.

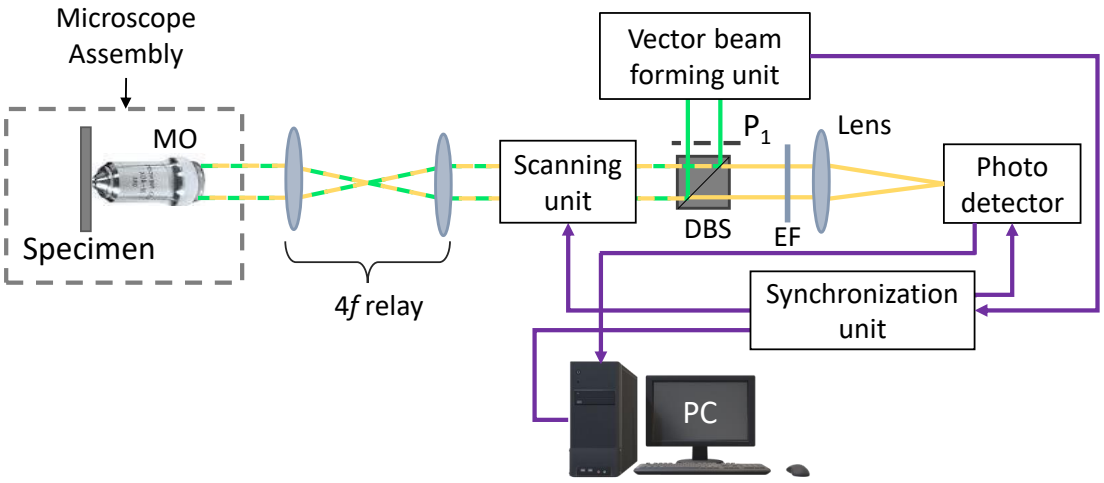

Figure 6.1: Schematic diagram of the laser scanning confocal microscope working in the fluorescence mode employing the intraframe polarization switching of the illumination beam.

6.2 Laser scanning confocal microscope in the fluorescence mode

The schematic diagram of the experimental arrangement used for the implementation of the intraframe polarization switching in a laser scanning confocal microscope working in fluorescence mode is shown in figure 6.1. The optical components of the microscope setup are the same as the one working in reflectance mode (5.3) except the dichroic beam splitter (DBS), in combination with a long-pass emission filter EF placed in between the DBS and the photo-detector, that replaces the beam splitter BS. As already discussed in section 2.3, the DBS reflects the beam of shorter wavelength (relative to the cut off wavelength) towards the specimen and transmits light of longer wavelength (relative to the cut off wavelength) towards the detector, while the EF blocks any shorter wavelength light coming from the specimen towards the detector.

Laser scanning confocal microscope in the fluorescence mode often uses sub-wavelength diameter fluorescent beads for routine checking and calibration [93]. Fluorescence beads are available in different sizes ranging from $0.1\mu m$ to about $15\mu m$ and having different excitation and emission spectra. Here we use $0.2\mu m$ diameter FluoSpheres beads (Carboxylate-Modified Microspheres, Make: Thermo Fisher Scientific) having peak excitation/ emission wavelengths $540/560nm$. The

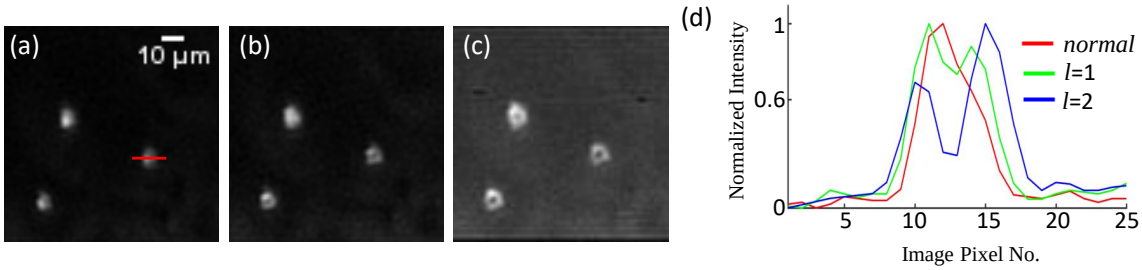

Figure 6.2: Experimental images (86×86 pixels, using $10X$, 0.3 NA Olympus MO lens, and confocal pinhole size $\simeq 4\times$ airy disc) of beads (200 nm FluoSpheres) with X polarized (a) normal (Gaussian) beam, (b) helical beam of topological charge $l = 1$, and, (c) helical beam of topological charge $l = 2$. (d) Line plots of normalized intensity against the image pixel number for the images (a)→(c) across an isolated bead as shown in (a), taking the coordinate of left most pixel as 1.

bead solution is first diluted by mixing $50\mu L$ of concentrated bead solution with $450\mu L$ distilled water for a 1:100 dilution. The solution is further diluted by taking a $50\mu L$ solution of 1:100 dilution to $450\mu L$ distilled water for a 1:10,000 dilution. The above steps are necessary to dilute the concentrated bead solution such that the beads are well sparse on the microscope slide. The final solution is well mixed using a vortex mixer before preparing it for imaging using the microscope slide and a coverslip as per protocol. The green DPSS laser ($\lambda = 532nm$) is used in the vector beam forming unit to realize the illumination beam and a $552nm$ single-edge (i.e. cut off) standard epi-fluorescence dichroic beamsplitter (Make: Semrock, Model: FF552-Di02-25x36) is used as the DBS. A $532nm$ long-pass emission filter (Make:Semrock, Model: BLP01-532R-25) is used as the EF to further ensure the transmission of light with a wavelength greater than $546nm$ that is focused on the photo-detector.

6.2.1 Results and discussions

We first image the beads using a fixed polarization state of the illumination beam for the entire image frame using a $10\times$ microscope objective. We use a $100\mu m$ pinhole, which is $\simeq 4\times$ the corresponding Airy disc at the detector plane, in front of the photo-detector. Figure 6.2(a) shows the recorded image of the beads using an X polarized illumination beam. Since the diameter of the bead is much smaller than the FWHM of the point spread function, which in the present case is $\simeq 900nm$, the image of an isolated bead will be a representative of the PSF of the microscope.

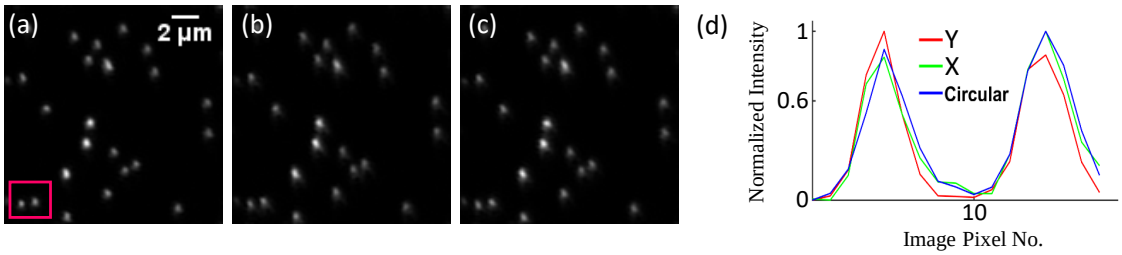

Figure 6.3: Experimental images (128 × 128 pixels, using $100X$, 1.4 NA Olympus oil immersion MO lens and confocal pinhole size $\simeq 2\times$ airy disc), using scheme-C, of $200nm$ FluoSpheres beads with (a) Y polarized beam, (b) X polarized beam, (c) circularly polarized beam. (d) The line plot of normalized intensity against the image pixel number for the images (a)→(c) across two isolated bead enclosed by the square box in red as shown in (a), taking the coordinate of left most pixel as 1.

We then modify the hologram to incorporate helical phase profiles [94] of different topological charges into the illumination beam. A helical beam when focused gives rise to a ring-line intensity distribution with the diameter of the ring increasing as the topological charge increases. Figures 6.2(b) and 6.2(c) show the recorded images of the beads using an X polarized helical beam of topological charge $l = 1$ and $l = 2$, respectively, as the illumination beam. Line plots of normalized intensities against the image pixel number, along a line across an isolated bead as shown in figure 6.2(a), for the images 6.2(a)→(c) are shown in figure 6.2(d). The image and the line plots demonstrate proper working of the scanning confocal microscope in the fluorescence mode. However the contrast and signal levels in the images are observed to be low compared to the same in the case of the reflectance mode. This is due to limited number of photons emitted by each bead which undergo further loss in each transmission through an optical element till they reach the detector. Unlike the reflectance mode amount of light reaching the detector is not directly proportional to the illumination beam intensity beyond a certain threshold value. Moreover owing to the finite size of the beads the centres of the bead images do not have zero intensities.

The FluoSpheres beads are then imaged using a $100X$, 1.4 NA lens employing scheme-C with the illumination beam switched between X, Y and circular polarization states. Figures 6.3(a), (b), and (c) show the images (pinhole size $\simeq 2\times$ Airy disc) of the beads when illuminated with Y polarized, X polarized and circularly polarized beams respectively. We observe that images of two beads corresponding to the red box in figure 6.3(a) show some significant variations under different po-

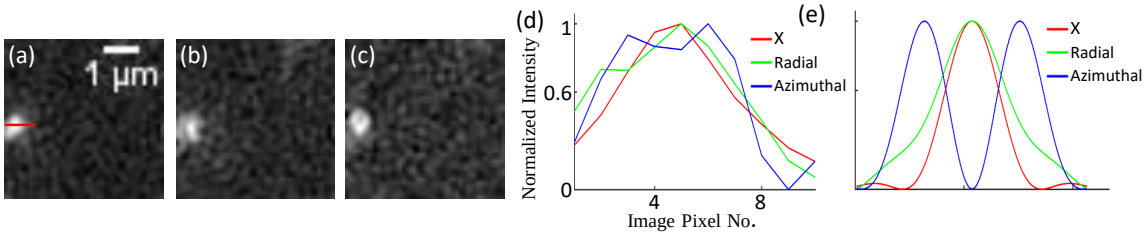

Figure 6.4: Experimental images (45×45 pixels, using $100X$, 1.4NA Olympus oil immersion MO lens and confocal pinhole size $\simeq$ 2 airy disc), using scheme-C, of FluoSpheres beads with (a) X polarized beam, (b) radially polarized beam, (c) azimuthally polarized beam. (d) The plot of normalized intensity against the image pixel number for the images (a)→(c) along a line as shown in (a). (e) normalized intensity plots through the center of the numerically obtained PSFs due to X, radially and azimuthally polarized beams.

larizations. As seen in line plots in figure 6.3(d) along a line passing through the centres of the two beads, it found that when illuminated with Y polarized light, the bead on left has higher peak value than the bead on the right, which reverses when the polarization is changed to X or circular polarizations. This indicates that the bead on the right has a dominant population of molecular dipoles oriented along X and the bead on the left has a dominant population of dipoles oriented along Y. Also the population of X oriented dipoles in the bead on R.H.S. is more than the population of Y oriented dipoles in the bead on L.H.S. because even with the circularly polarized illumination beam, that has equal amount of X and Y polarized light, the peak intensity in the bead on the right is more than the peak in intensity in the beam on the left. We then update the color holograms to implement scheme-C using X, radially and azimuthally polarized beams. Figures 6.4(a), (b), and (c) show the recorded images of the fluorescent beads when illuminated with X, radially and azimuthally polarized beams, respectively. Figure 6.4(d) shows the plot of normalized intensity against the image pixel number for images 6.4(a)→(c) along a line passing through the bead as shown in figure 6.4(a). Figure 6.4(e) shows the normalized intensity line plots through the center of the simulated PSFs due to X polarized (solid line in red), radially polarized (solid line in green) and azimuthally polarized (solid line in blue) beams. Comparison of figures 6.4(d) and (e) indicate that as in the simulated plots, the PSF with azimuthal polarization tends to show a dip at the centre even in the experimental plot. Such clear dip at the centre is not seen in the case of linear and radial polarizations. In the case of the X polarized beam mostly the X oriented molecular dipoles and in the case of the radially polarized beam mostly the axially oriented dipoles contribute to the PSFs. The

experimental plot with the azimuthally polarized beam does not have a zero minimum at the centre owing to the finite diameter of the bead which is not negligible compared to the width of the dark centre as seen in the simulation. The results in figures 6.3 and 6.4 demonstrate that our setup is able to implement scheme-C to switch the illumination beam between various arbitrary polarization states after each line scanned.

6.2.2 The issue of wobble in the scan mirrors

As already discussed in the previous chapter, the polarization switching scheme enables one to illuminate each pixel in the specimen plane with two different polarizations at a time interval of $5.56ms$. However, the galvanometer scanner based beam scanning adopted in the proposed microscope has a limited beam positioning accuracy and stability [40]. This leads to wobbles in the scan mirrors which may have both short term and long term manifestation. One reason for such wobble is that the high-speed operation of the scanners leads to temperature variations. Figure 6.5 shows the image of element 6 group 7 of the USAF 1951 resolution test target using $100X$, 1.4NA MO lens, and an X polarized illumination beam recorded by the our confocal system in the reflection mode. The magnified view of the central portion of the image indicated by a square in red is shown as the inset, which clearly shows the variation at the edges of a strip in the target, caused by the wobble. The affect of such wobble is also evident in figures 6.3 and 6.4, highlighting the limitation of the present scanning unit in precise scanning of the specimen.

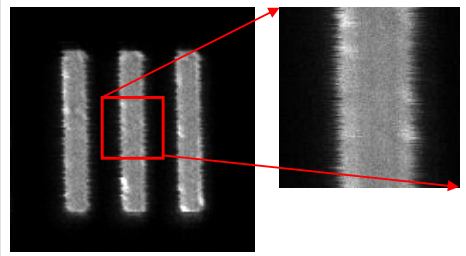

Figure 6.5: Reflected light image of a portion of the USAF 1951 test target using $100X$, 1.4NA Olympus oil immersion MO lens.

Fortunately the beam scanning in a microscope can also be achieved holographically in the +1 order diffracted beam, by writing a sequence of computer generated holograms on the LCSLM with gradually varying tilts and displaying in a sequence manner [44, 46, 95]. Such holographic beam scanning offers superior stability and repeatability [45, 96] of the illumination beam in a scanning microscope.

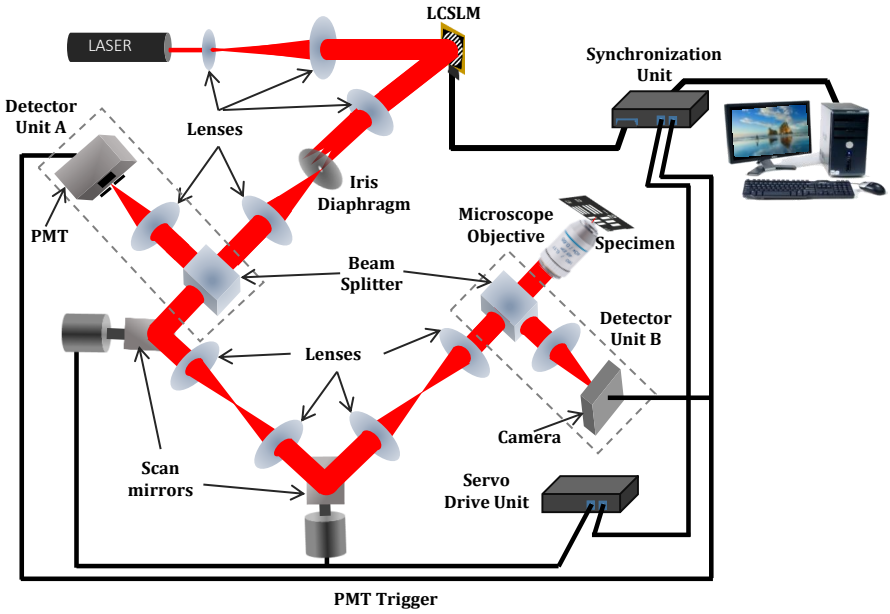

Figure 6.6: Schematic diagram of the beam scanning microscope with galvanometer based as well as CGH based beam scanning mechanism.

6.3 Scanning microscope with both scan mirror based and holographic beam scanning

In order to investigate the performance in regards to beam positioning accuracy of the galvanometer scanner based as well as holographic beam scanning, we develop a beam scanning microscope equipped with both the beam scanning mechanisms.

6.3.1 Experimental arrangement

The schematic of the beam scanning microscope with galvanometer based and CGH based beam scanning mechanisms is shown in figure 6.6. The beam from a He-Ne laser is expanded and collimated using a combination of two lenses. The collimated beam illuminates the LCSLM panel, where a binary hologram is written. The +1 order beam diffracted by the binary hologram is then isolated from the other orders using a lens and an iris diaphragm (ID) and which then travels towards the galvo scanning unit via a beam splitter. The two scan mirrors are separated using a $4f$ relay system. The beam then enters the microscope objective after passing through another beam splitter. The reflected light from the specimen is collected by the same MO and which then travels towards the detector unit A or B, depending on

the choice of the beam scanning mechanism.

During the operation of the galvanometer based beam scanning, a static binary hologram is written on the LCSLM. Here, the light from the specimen is de-scanned by the scanning unit before it enters into the detector A (i.e. PMT) via a beam splitter. An iris diaphragm, ID, is placed in front of the PMT as the confocal pinhole. The microprocessor based synchronization unit synchronizes the operation of the scanning unit with the analog-to-digital conversion of the DAQ card linked to the PMT.

When the CGH based beam scanning is in operation, the galvanometer scanners are set at zero deflection position. The light from the specimen collected by the MO moves towards the camera (detector B) after getting reflected by the beam splitter. A lens is used to focus the beam onto the camera. A detector window (a square area of the camera image) is defined in the camera plane surrounding the image of the +1 order focal spot, to act as the confocal detector. The net signal in this detector window constitutes the detector signal for a given scan position. As a series of holograms with appropriate tilt values are written on the LCSLM, the +1 diffracted order beam scans the desired area in the specimen plane. In synchronization with the movement of the illumination spot, the detector window is also moved programmably to each scan position, and the net signal corresponding to each location is stored in the PC. Finally, the stored data is used to construct the electronic image of the specimen. Optical sectioning capability of the microscope can be increased by decreasing the size of the detector window.

6.3.2 Study on beam stability and repeatability

We first capture images of element 1 group 7 of the USAF 1951 resolution test target using both the beam scanning mechanisms. Figures 6.7(a) and (b) show the images of the test target using the galvanometer scanner based beam scanning and CGH based beam scanning mechanism, respectively. The specimen is scanned over 256×256 positions covering an area of about $21\mu m \times 21\mu m$. A line plot against the image pixel number for the two images, drawn along a line as indicated in the images, is shown in figure 6.7(c). The line plot demonstrates that both the beam scanning mechanisms cover almost the same area on the specimen plane. We then study the repeatability of both the beam scanning methods by scanning a particular line of the specimen (i.e. the central line of the images 6.7(a) and (b)) repeatedly for 20

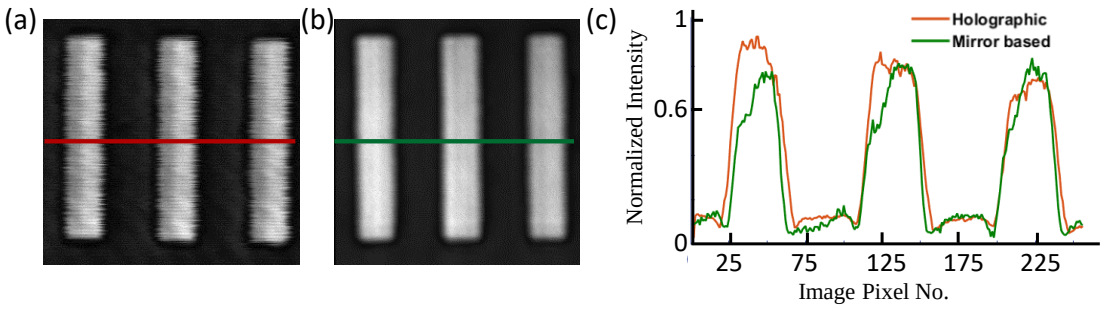

Figure 6.7: Images (256 × 256 pixels) using 40X, 0.6NA Olympus MO lens of element 1 group 7 of the USAF resolution test target with (a) galvanometer based and (b) binary hologram based beam scanning mechanism. (c) intensity plots against image pixel number along a line as indicated in (a) and (b).

times. Figures 6.8(a) and (b) show the plots of pixel values against the pixel number along the given line for each scan, corresponding to the two scanning mechanisms. A histogram of the number of occurrences of the pixel numbers coinciding with half the maximum value for the line against the pixel number is plotted. Figures 6.8(c) and (d) show the histograms for the galvanometer based scanning and holographic scanning, respectively. From the histogram plots, it is evident that the CGH based beam scanning mechanism has better beam positioning accuracy and repeatability than that of the galvanometer based beam scanning mechanism.

6.4 Holographic scanning confocal microscopy for both reflected light and fluorescence light imaging

In the above, we have observed that a scanning microscope with holographic beam scanning provides superior beam stability and repeatability. In order to test the ability of such a system for fluorescence light imaging as well, we develop a holographic scanning confocal microscope that can work both in the reflection and florescence mode.

6.4.1 Experimental arrangement

In order to image the desired area of a specimen, the fluorescence imaging is often preceded by reflected light imaging, such that the correct imaging area can be

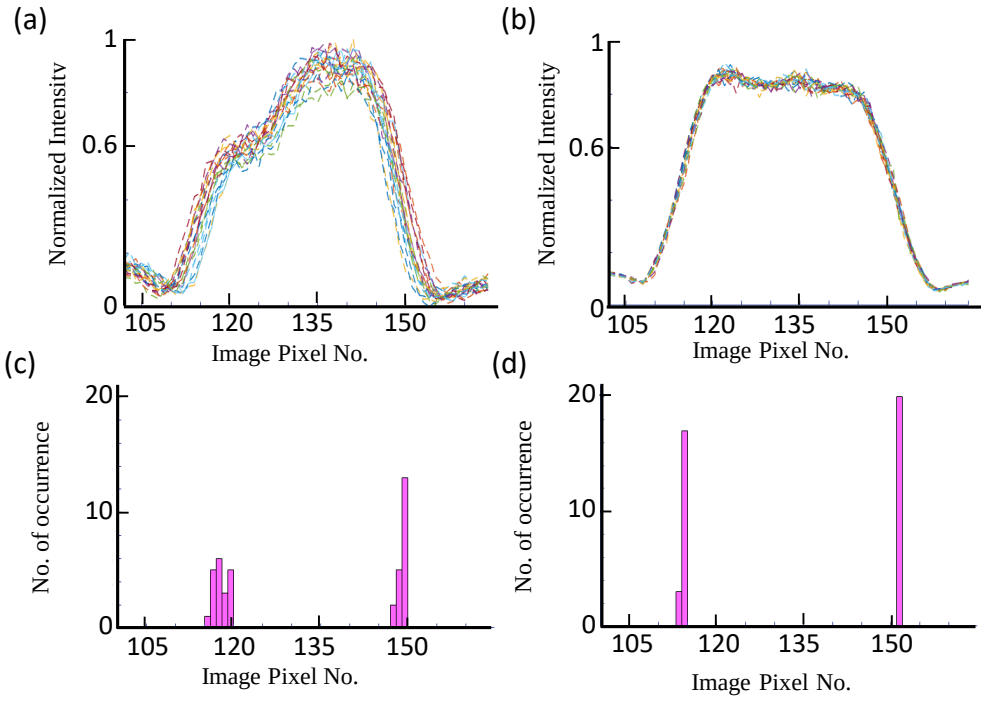

Figure 6.8: Experimentally obtained intensity plots across the central strip of element 1 group 7 of USAF 1951 test target (scanned repeatedly over 20 times with different scans indicated by different colors) with (a) galvanometer based and (b) CGH based beam scanning mechanism. (c) and (d) are the histogram plot showing the number of occurrences when the intensity value crosses the half of the maximum value of (a) and (b) against the image pixel number.

identified by examining the reflected light image. However, if the same laser is used for both reflected light and fluorescence light imaging, the illumination during the reflected light imaging may lead to photobleaching of the interested region [38], thereby resulting in reduced contrast of the fluorescent images. Here we use two lasers, a red laser for reflected light imaging and a green laser for fluorescence light imaging. For a fluorescent dye with peak absorption at green, there will be very little absorption at red and hence there will be very little photobleaching even if fluorescence imaging is preceded by reflected light imaging. We also use the same set of the dichroic beam splitter and emission filter for both the modes so that in between the two modes, there is no disturbance to the microscope stage.

The schematic diagram of the holographic scanning confocal microscope is shown in figure 6.9(a). The microscope setup primarily comprises the Olympus Inverted IX51 microscope assembly, two lasers, the FELCSLM for quick display of binary holograms, and the Basler CCD camera as the detector. The DPSS green laser

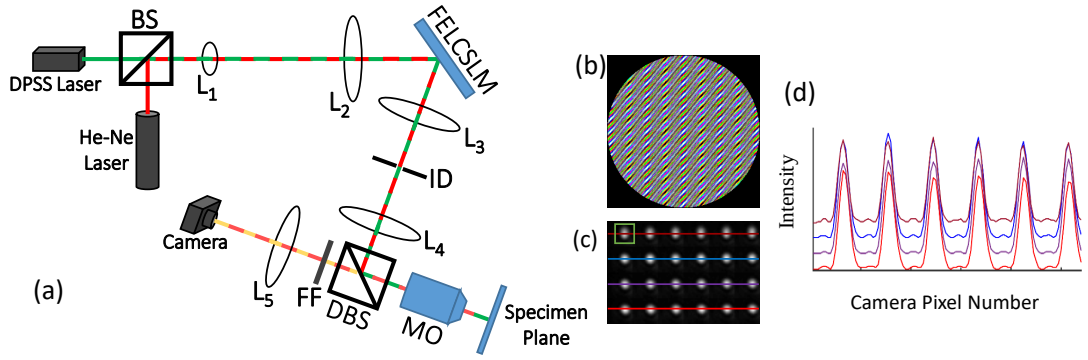

Figure 6.9: (a) Schematic diagram of the holographic scanning confocal microscope, (b) a color image comprising 24 binary holograms, (c) an experimental image of the focal spots generated by one color image displayed on the FELCSLM, and (d) intensity plots along the lines shown in figure (c) with different offsets (in the vertical direction) applied to the different rows, indicating precise overlap of the focal spots in the horizontal direction.

for fluorescence light imaging and the He-Ne red laser for reflectance light imaging, are combined using a beam-splitter BS so that they follow a common path. The collimated laser beams illuminate the FELCSLM display panel which displays each 24 single-bit planes of a color image at a rate of 1440 Hz using 24sb display mode. The display of each color image on the FELCSLM results in a +1 order diffracted beam traveling along each of the 24 user-defined directions. The +1 order beam after getting reflected by the DBS is eventually focused by a $10X$ MO lens onto the specimen. The DBS used has an edge wavelength of $552nm$ so that $\simeq$98% of the green light and about $\simeq$7% of the red light is reflected. The two lenses L_3 and L_4 constitute a $4f$ relay system such that the FELCSLM panel and the entrance pupil of the MO are conjugate to one another. Reflected or fluorescence light from the specimen is collected by the same MO lens and after transmission through the DBS and the emission filter EF is focused by a lens (L_5) onto the camera. A microprocessor based synchronization unit is used to generate trigger pulses to expose the camera for a duration equal to the display period of 24 single-bit images (equal to $16.67ms$) corresponding to a single color image. Figure 6.9(b) shows a representative color image comprising 24 binary holograms, while figure 6.9(b) shows the resulting 24 focal spots (arranged in 4 rows) corresponding to 24 different scan positions of the illumination beam captured in a single camera frame (using an exposure time of $16.7ms$). Figure 6.9(d) shows the normalized intensity plots along the lines shown in figure 6.9(c). The horizontal pixel coordinates of the six intensity maxima in each row are found to be 13, 31, 49, 67, 85, and 103,

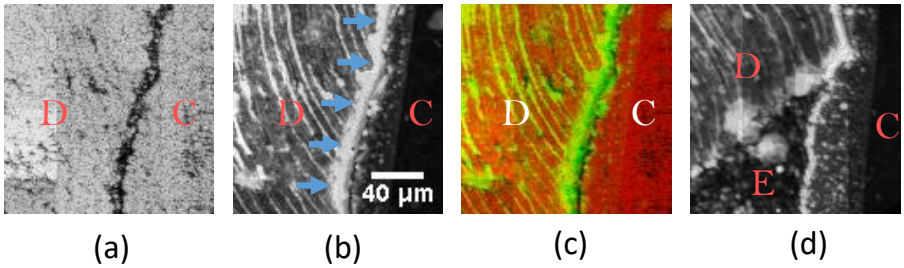

Figure 6.10: Images (120 × 120 pixels) of a tooth section using (a) reflected light and (b) fluorescence light. (c) False color image combining the reflected image and the corresponding fluorescence image. (d) A fluorescent image of the tooth section showing the interface among dentin (D), enamel (E), and composite (C).

taking the coordinate of the left most pixel as 1, which indicates the precise overlap of the focal spots in the horizontal direction. Therefore, considering the specimen is to be scanned over $n \times n$ pixels, a sequential display of $(n \times n)/24$ numbers of appropriately constructed color images will make the illumination beam scan the specific area. Confocal image is constructed by defining a digital detector window as described in section 6.3.1.

Depending on the imaging mode (fluorescence or reflection), only one laser beam is operated at a time. We use two sets of binary holograms for the two lasers. Each set, along with the tilts, also incorporates aberration and defocus correction (to compensate for chromatic aberration) by using an appropriate expression of the phase function $\phi_b(x, y)$ as discussed in chapter 3.

6.4.2 Results with the reflection and fluorescence modes together

We have use a section of an extracted human premolar tooth as the specimen for the experiment. The tooth goes through Class II cavity preparation as per protocol after which it is restored with resin based composite. The tooth specimen is then immersed in 0.5 % Rhodamine B fluorescent dye and a longitudinal buccolingual section of the tooth is prepared.

We first obtain the reflected light image followed by the fluorescence image of the tooth section using a detector window area of 4 × 4 pixels. The full width at half maxima of the illumination spot in the camera plane is around 6 pixels. The scanning is performed over a specimen area of $156\mu m \times 156\mu m$ using 120 × 120 scan positions with an acquisition time of about 18 seconds per image. Figures

6.10 (a) and (b) show the reflected light and fluorescence light images of the tooth section. The reflected light image shows the interface between the dentin (D) and the composite (C) in the cavity as a dark line, while the fluorescence image shows strong fluorescence coming from the interface gap (marked by the arrows) and leakage of the composite into dentinal tubules. Figure 6.10 (c) shows a false color image constructed using the reflected light image in the red channel and the corresponding fluorescence light image in the green channel. The overlap of the two images showing a green line at the interface gap indicates that both lasers are imaging the same area of the specimen. Figure 6.10 (d) shows the fluorescence image of another area of the tooth section revealing the interface among dentin (D), enamel (E) and the composite (C) which confirms that other than the interface there is no fluorescence emission from the enamel or composite.

6.5 Implementation of polarization switching in the holographic scanning confocal microscope in the fluorescence mode

In the above section we have demonstrated that a holographic scanning confocal microscope can not only work in the reflection mode but also in the fluorescence mode. In this section we implement polarization switching of the illumination beam in a holographic scanning confocal microscope and record images of fluorescent beads with different polarizations of the illumination beam. The schematic diagram of the optical arrangement to implement polarization switching of the illumination in the holographic scanning confocal microscope is shown in figure 6.11. The setup is almost the same as that of the galvanometer based beam scanning microscope as described in section 6.2.1 with a modification where a mirror is used in the place of the DBS, and the DBS in combination with the EF, lens and the camera is placed just before the MO as in the setup in figure 6.9. Although the scan mirrors are in the beam path they are not used for scanning and the mirrors are kept at their 0 positions. The FELCSLM displays binary holograms using the 24sb display mode as in section 6.4.1 so that the +1 order beam goes to 24 location of the specimen plane and a single capture with the camera records the images of the illumination spots for all the 24 scan positions. A color image (say C1) is constructed in such

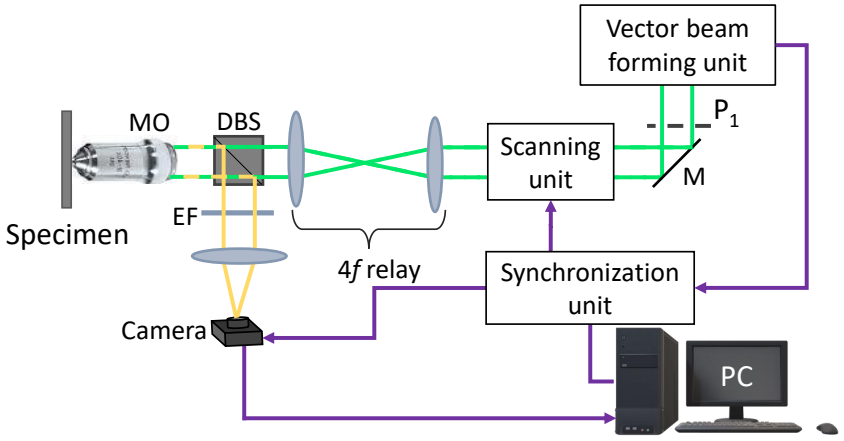

Figure 6.11: Schematic diagram of the holographic scanning confocal microscope implementing polarization switching of the illumination beam.

a way that all the 24 constituent single-bit images are binary holograms or pairs of binary holograms that result in an illumination beam in the specimen plane with a particular polarization (say P1). After the recording of the images of the 24 illumination spots corresponding to polarization P1 another color image (say C2) is constructed such that the corresponding 24 single-bit images are binary holograms or pairs of binary holograms that result in illumination beam of polarization P2. After the recording of the illumination spot images, the illumination beam can be switched to another polarization, say P3, using another color image C3. Thus another set of three color images (C1, C2, C3) can be constructed to scan the next set of 24 locations of the specimen. At the end of the scanning, the data stored in the PC can be used by defining a detector window as described in section 6.4.1, to construct three confocal images corresponding to three different polarizations of the illumination beam.

In order to achieve the polarization switching of the illumination beam between m number of polarized profiles, m color images are constructed and displayed on the FELCSLM.

A proof of principle experiment is carried out to demonstrate the proposed polarization switching scheme in the holographic scanning confocal microscope, where the illumination beam is switched between plane polarized along X, plane polarized along Y, and circular polarization states. Figures 6.12(a), (b), and (c) show the images (using $100X$ MO lens, detector window area of 8×8 pixels, where FWHM of the illumination spot in the camera plane is around 12 pixels) of the $200nm$

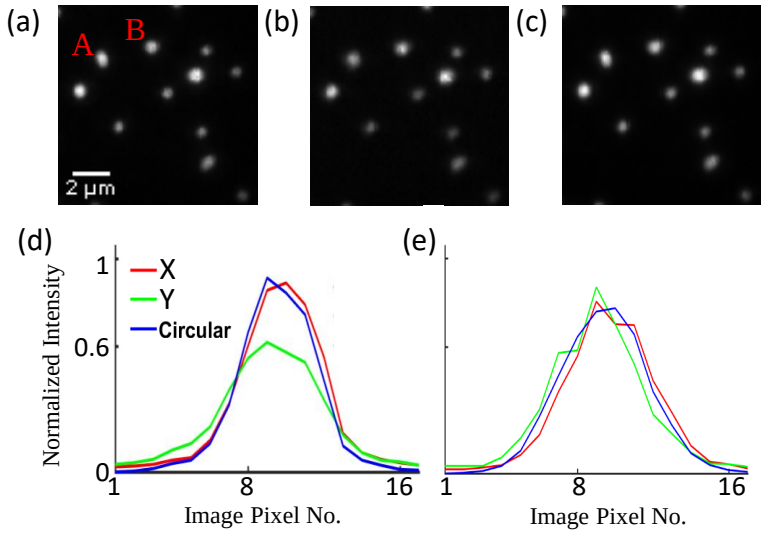

Figure 6.12: Images (96×96 pixels) using $100X$, 1.4NA Olympus oil immersion MO lens of $200nm$ FluoSpheres beads with (a) X polarized beam, (b) Y polarized beam, and (c) circularly polarized beam. (d) and (e) are the plots of normalized intensities against the image pixel number across the bead A and B shown in (a), respectively. The coordinate of left most pixel of each plot is taken as 1.

FluoSpheres beads when illuminated with X polarized, Y polarized and circularly polarized beams respectively. We identify two beads denoted as A and B (shown in figure 6.12(a)), which appear to have a differential response to different polarizations. Figures 6.12(d) and (e) are the plots of intensity against the image pixel number, along a line passing through the beads A and B. From the line plots, it is seen that, when illuminated with Y polarized light, the bead A has lower maximum than that of the bead B but has a nearly equal maximum value when illuminated with X polarized and circularly polarized beams. This indicates that in bead A the number of molecular dipoles oriented along Y is relatively less.

Thus we have seen that programmable polarization switching can be implemented even in the holographic scanning confocal microscope in the fluorescence mode. It provides scanning with superior accuracy in comparison with the scan mirror based setup. However a price is to paid in terms of the image frame rate. To construct an image over $N \times N$ pixels with just one polarization, a holographic scanning confocal microscope takes atleast $\frac{N \times N}{1440}$ sec (=45.51 sec for N=256), which is much more than the same using the scan mirrors. Therefore such a polarization switching scheme will be useful if the number of scan positions are less.

6.6 Conclusion

In this chapter, we have described the development of a laser scanning confocal microscope in the fluorescence mode employing polarization switching of the illumination beam at the end of each line scanned. We have presented experimental results to demonstrate the implementation of the polarization switching scheme to modulate the illumination beam among different scalar as well as vector beam profiles. We then highlighted the issue of wobble associated with the scan mirror setup that limits beam repeatability and described how the computer generated hologram based beam scanning can address this issue. We have demonstrated the implementation of the computer generated hologram based beam scanning in a confocal imaging system working in both reflection and fluorescence mode. We have then implemented polarization switching between three different polarizations in a holographic scanning confocal microscope by imaging fluorescent beads.

* * *

Chapter 7

Conclusion and future prospects

7.1 Conclusion

The laser scanning confocal microscope (LSCM) is a powerful tool to obtain high contrast optically sectioned images of a specimen. It finds diverse applications, in particular areas, such as in biological science and biomedical science. Use of polarization in an LSCM can extract more information from the specimen, for instance, information on molecular orientation, which is otherwise not possible. Polarization based applications of LSCM require the system to have a capability to generate illumination beams with different polarization profiles and to quickly switch between different polarization profiles. However the conventional LSCMs do not have a robust mechanism to generate and switch between, various user-defined polarization profiles of the illumination beam. In this thesis we propose a robust and flexible scheme using a single computer controlled liquid crystal spatial light modulator (LCSLM) to generate arbitrary and user-defined vector beams with the highest average-power possible with a LCSLM based method. We then employ this scheme in a scan mirror based confocal system where the polarization of the illumination beam is switched after every line scanned. We implement the polarization switching in both reflectance and fluorescence modes of the scan mirror based LSCM constructed and also in a holographic scanning confocal microscope.

Below we provide a chapter-wise summary of the thesis.

In chapter 1, we have provided a brief description of the basic research problem and its proposed solution followed by a chapter-wise overview.

In chapter 2, we have discussed on the working principle of a laser scanning confocal microscope and the polarization in a LSCM. We have the discussed about

some of the issues with the present state of the art and briefly described the main building blocks of the basic LSCM built in the thesis.

In chapter 3, we have introduced the basic principle of the computer generated holography technique, followed by a discussion on liquid crystal spatial light modulators and how they can be used to write computer generated holograms. We have elaborated on the algorithms adopted to compute binary holograms to generate scalar beams and vector beams with arbitrary and user-defined complex amplitude profiles and how they can be implemented using nematic or ferroelectric LCSLMs.

In chapter 4, we have introduced a division of wavefront-based scheme using a single liquid crystal spatial light modulator to generate an arbitrary user-defined vector beam. We have demonstrated the working of the proposed scheme by generating a few important vector beams. We have shown how the displacement theorem enables the shifting of the focal volume intensity distribution in the axial direction under low NA focusing condition by incorporating defocus into the beam and how the same can used to record the three-dimensional focal intensity distribution. We have generated a coma aberrated azimuthally polarized beam and recorded the resulting boat-shaped three-dimensional focal intensity distribution as a demonstration of the capability of the proposed scheme to incorporate precise phase control of the generated vector beam.

In chapter 5, we have built a laser scanning microscope with the division of wavefront-based vector beam forming unit as a part of the illumination beam generation assembly. We have implemented polarization switching of the illumination beam at the end of each line scanned, exploiting the ferroelectric LCSLM display properties. We have introduced three polarization switching schemes depending on the number of polarization states between which the illumination beam is to be switched. We have implemented the polarization switching schemes in the reflection mode of the LSCM.

In chapter 6, we have described the development of the LSCM in the fluorescence mode employing polarization switching of the illumination beam at the end of each line scanned. We have presented experimental results to demonstrate the implementation of the polarization switching scheme to modulate the illumination beam among different scalar as well as vector beam profiles. We have then highlighted the issue of wobble associated with the scan mirror setup that limits beam repeatability and have described how the computer generated hologram based beam scanning can address this issue. We have implemented holographic beam scanning

in a confocal microscope working in both reflection and fluorescence modes, where the illumination beam is scanned holographically without the scan mirrors. We have also implemented a polarization switching scheme in the fluorescence mode of a holographic scanning confocal microscope.

7.2 Future prospects

1. In this thesis we allow an expanded TEM_{00} mode to incident simultaneously on the two holograms displayed on the LCSLM of the division of wavefront-based vector beam forming unit. This results in a significant loss of light which do not incident on the two holograms. Instead of one beam, the optics can be modified, such as using a combination of beam splitters and mirrors so that two mutually coherent beams each in TEM_{00} mode, derived from the same laser, are simultaneously incident on the two holograms. This arrangement will significantly enhance the overall light efficiency of the unit.

2. We have used 3sb display mode of the ferroelectric LCSLM to implement the polarization switching after every line scanned in a scanning microscope. The polarization switching can also be implemented using 24sb display mode of the ferroelectric LCSLM to enhance the image frame rate or to include more than three polarization profiles. The image frame rate of the line wise polarization switching scheme can further be increased by using multiple vectors beams generated by multiplex binary holograms and resonant mirror scanners.

3. We have implemented the polarization switching scheme on a steady specimen. Instead, the scheme can be employed in a moving specimen such as when imaging of biological specimen in a microscopic flow, imaging of live specimens such as mouse brain and so on. In the same study, the advantage of the line wise polarization switching relative to polarization switching after each image frame can be investigated.

4. The use of quick polarization switching as proposed in our scheme can also be exploited in non microscopic imaging applications such as in the field of optical data storage, optical image encryption, material processing and so on.

* * *

References

[1] Tony Wilson. Confocal microscopy. *Academic Press: London, etc*, 426:1–64, 1990. 1, 8

[2] CJR Sheppard and T Wilson. Depth of field in the scanning microscope. *Optics letters*, 3(3):115–117, 1978. 1, 8

[3] Denis Semwogerere and Eric R Weeks. Confocal microscopy. *Encyclopedia of Biomaterials and Biomedical Engineering*, pages 1–10, 2005. 1

[4] Emmanuel Donnadieu, Yvonne Michel, and Martin-Leo Hansmann. Live imaging of resident t-cell migration in human lymphoid tissue slices using confocal microscopy. In *T-Cell Motility*, pages 75–82. Springer, 2019. 1

[5] Pinnita Prabhasawat, Angkoon Luangaram, Pattama Ekpo, Kaevalin Lekhanont, Wimolwan Tangpagasit, Chawikan Boonwong, Naharuthai Inthasin, and Chareenun Chirapapaisan. Epithelial analysis of simple limbal epithelial transplantation in limbal stem cell deficiency by in vivo confocal microscopy and impression cytology. *Cell and tissue banking*, 20(1):95–108, 2019. 1

[6] Takeshi Yoneyama, Tetsuyo Watanabe, Hiroyuki Kagawa, Yutaka Hayashi, and Mitsutoshi Nakada. Fluorescence intensity and bright spot analyses using a confocal microscope for photodynamic diagnosis of brain tumors. *Photodiagnosis and photodynamic therapy*, 17:13–21, 2017. 1

[7] Mathias W Seeliger, Susanne C Beck, Naira Pereyra-Muñoz, Susann Dangel, Jen-Yue Tsai, Ulrich FO Luhmann, Serge A van de Pavert, Jan Wijnholds, Marijana Samardzija, Andreas Wenzel, et al. In vivo confocal imaging of the retina in animal models using scanning laser ophthalmoscopy. *Vision research*, 45(28):3512–3519, 2005. 1

[8] Elizabeth Yang, Toby S Al-Mugheiry, Eduardo M Normando, and Maria F Cordeiro. Real-time imaging of retinal cell apoptosis by confocal scanning laser ophthalmoscopy and its role in glaucoma. *Frontiers in neurology*, 9:338, 2018. 1

[9] Meenesh R Singh, Jayanta Chakraborty, Nandkishor Nere, Hsien-Hsin Tung, Shailendra Bordawekar, and Doraiswami Ramkrishna. Image-analysis-based method for 3d crystal morphology measurement and polymorph identification using confocal microscopy. *Crystal Growth & Design*, 12(7):3735–3748, 2012. 1

[10] JH Liu, N Vanderesse, J-C Stinville, TM Pollock, P Bocher, and Damien Texier. In-plane and out-of-plane deformation at the sub-grain scale in polycrystalline materials assessed by confocal microscopy. *Acta Materialia*, 169:260–274, 2019. 1

[11] Cian D Hickey, Jeremiah J Sheehan, Martin G Wilkinson, and Mark AE Auty. Growth and location of bacterial colonies within dairy foods using microscopy techniques: a review. *Frontiers in microbiology*, 6:99, 2015. 1

[12] Bin Zhou, Yaguang Luo, Gary R Bauchan, Hao Feng, and John R Stommel. Visualizing pathogen internalization pathways in fresh tomatoes using microct and confocal laser scanning microscopy. *Food control*, 85:276–282, 2018. 1

[13] Michael Prummer, Beate Sick, Bert Hecht, and Urs P Wild. Three-dimensional optical polarization tomography of single molecules. *The Journal of chemical physics*, 118(21):9824–9829, 2003. 1

[14] Mamoru Hashimoto, Kazuaki Yamada, and Tsutomu Araki. Proposition of single molecular orientation determination using polarization controlled beam by liquid crystal spatial light modulators. *Opt. Rev.*, 12(1):37–41, 2005. 2

[15] L Novotny, MR Beversluis, KS Youngworth, and TG Brown. Longitudinal field modes probed by single molecules. *Physical Review Letters*, 86(23):5251, 2001. 2, 15

[16] Karl Zhanghao, Juntao Gao, Dayong Jin, Xuedian Zhang, and Peng Xi. Super-resolution fluorescence polarization microscopy. *Journal of Innovative Optical Health Sciences*, 11(01):1730002, 2018. 2

[17] Ning-Jiun Jan, Jonathan L Grimm, Huong Tran, Kira L Lathrop, Gadi Wollstein, Richard A Bilonick, Hiroshi Ishikawa, Larry Kagemann, Joel S Schuman, and Ian A Sigal. Polarization microscopy for characterizing fiber orientation of ocular tissues. *Biomedical optics express*, 6(12):4705–4718, 2015. 2

[18] Josef Lazar, Alexey Bondar, Stepan Timr, and Stuart J Firestein. Two-photon polarization microscopy reveals protein structure and function. *Nature methods*, 8(8):684, 2011. 2

[19] Stefano Vezzoli, Mathieu Manceau, Godefroy Leménager, Quentin Glorieux, Elisabeth Giacobino, Luigi Carbone, Massimo De Vittorio, and Alberto Bramati. Exciton fine structure of CdSe/CdS nanocrystals determined by polarization microscopy at room temperature. *ACS nano*, 9(8):7992–8003, 2015. 2

[20] Lean L Dasallas, Rafael B Jaculbia, Maria Vanessa Balois, Wilson O Garcia, and Norihiko Hayazawa. Position, orientation, and relative quantum yield ratio determination of fluorescent nanoemitters via combined laser scanning microscopy and polarization measurements. *Optical Materials Express*, 8(5): 1290–1304, 2018. 2

[21] Jin-Kun Guo and Jang-Kun Song. Three-dimensional reconstruction of topological deformation in chiral nematic microspheres using fluorescence confocal polarizing microscopy. *Optics express*, 24(07):7381–7386, 2016. 2

[22] Robert D Allen, James Brault, and Robert D Moore. A new method of polarization microscopic analysis: I. scanning with a birefringence detection system. *The J. Cell Biol.*, 18(2):223–235, 1963. 2, 58

[23] William Mickols, Ignacio Tinoco, Joseph E Katz, Marcos F Maestre, and Carlos Bustamante. Imaging differential polarization microscope with electronic readout. *Rev. Sci. Instrum.*, 56(12):2228–2236, 1985. 2, 58

[24] Xiao Wang, Alla Kress, Sophie Brasselet, and Patrick Ferrand. High framerate fluorescence confocal angle-resolved linear dichroism microscopy. *Rev. Sci. Instrum.*, 84(5):053708, 2013. 2, 58

[25] Jeffrey R Kuhn, Zhuoru Wu, and Martin Poenie. Modulated polarization microscopy: a promising new approach to visualizing cytoskeletal dynamics in living cells. *Biophysical journal*, 80(2):972–985, 2001. 2, 58

[26] Rudolf Oldenbourg and Guang Mei. Polarized light microscopy, May 28 1996. U.S. Patent No. 5,521,705. 2, 58

[27] Blandine Laude-Boulesteix, Antonello De Martino, Bernard Drévillon, and Laurent Schwartz. Mueller polarimetric imaging system with liquid crystals. *Appl. Opt.*, 43(14):2824–2832, 2004. 2, 58

[28] Michael Shribak. Complete polarization state generator with one variable retarder and its application for fast and sensitive measuring of two-dimensional birefringence distribution. *J. Opt. Soc. Am. A*, 28(3):410–419, 2011. 2, 58

[29] Shalin B Mehta, Michael Shribak, and Rudolf Oldenbourg. Polarized light imaging of birefringence and diattenuation at high resolution and high sensitivity. *Journal of Optics*, 15(9):094007, 2013. 2, 14, 58

[30] Ching-Bo Juang, Laura Finzi, and Carlos J Bustamante. Design and application of a computer-controlled confocal scanning differential polarization microscope. *Review of scientific instruments*, 59(11):2399–2408, 1988. 2, 14, 58

[31] Gábor Steinbach, István Pomozi, Ottó Zsiros, László Menczel, and Győző Garab. Imaging anisotropy using differential polarization laser scanning confocal microscopy. *Acta histochemica*, 111(4):317–326, 2009. 2, 58

[32] Zhen-Yu Rong, Yu-Jing Han, Shu-Zhen Wang, and Cheng-Shan Guo. Generation of arbitrary vector beams with cascaded liquid crystal spatial light modulators. *Opt. Express*, 22(2):1636–1644, 2014. 3

[33] F Kenny, D Lara, OG Rodríguez-Herrera, and C Dainty. Complete polarization and phase control for focus-shaping in high-na microscopy. *Opt. Express*, 20 (13):14015–14029, 2012. 3

[34] Mark A A Neil, Farnaz Massoumian, Rimvydas Juškaitis, and Tony Wilson. Method for the generation of arbitrary complex vector wave fronts. *Optics letters*, 27(21):1929–1931, 2002. 3, 38, 42, 46

[35] Christian Maurer, Alexander Jesacher, Severin Fürhapter, Stefan Bernet, and Monika Ritsch-Marte. Tailoring of arbitrary optical vector beams. *New Journal of Physics*, 9(3):78, 2007. 3, 42, 46

[36] Ignacio Moreno, Jeffrey A Davis, Travis M Hernandez, Don M Cottrell, and David Sand. Complete polarization control of light from a liquid crystal spatial light modulator. *Optics Express*, 20(1):364–376, 2012. 3, 38, 42

[37] Rainer J Beck, Jonathan P Parry, William N MacPherson, Andrew Waddie, Nick J Weston, Jonathan D Shephard, and Duncan P Hand. Application of cooled spatial light modulator for high power nanosecond laser micromachining. *Optics express*, 18(16):17059–17065, 2010. 3, 42

[38] James Pawley. *Handbook of biological confocal microscopy*. Springer Science & Business Media, 2010. 3, 80

[39] Daisuke Matsuka, Tsubasa Tanaka, and Makoto Iwasaki. Thermal demagnetization compensation for fast and precise positioning in galvanometer scanners. *IEEE Transactions on Industrial Electronics*, 63(9):5514–5522, 2016. 3

[40] Arkadiusz Kuś. Illumination-related errors in limited-angle optical diffraction tomography. *Applied optics*, 56(33):9247–9256, 2017. 3, 76

[41] Yinyin Bao, Elise Guégain, Valérie Nicolas, and Julien Nicolas. Fluorescent polymer prodrug nanoparticles with aggregation-induced emission (aie) properties from nitroxide-mediated polymerization. *Chemical Communications*, 53 (32):4489–4492, 2017. 3

[42] Flavie Sarrazin, Jean-Baptiste Salmon, David Talaga, and Laurent Servant. Chemical reaction imaging within microfluidic devices using confocal raman spectroscopy: the case of water and deuterium oxide as a model system. *Analytical chemistry*, 80(5):1689–1695, 2008. 3

[43] Thomas V Johnson, Ericka N Oglesby, Matthew R Steinhart, Elizabeth Cone-Kimball, Joan Jefferys, and Harry A Quigley. Time-lapse retinal ganglion cell dendritic field degeneration imaged in organotypic retinal explant culture. *Investigative ophthalmology & visual science*, 57(1):253–264, 2016. 3

[44] Mark A A Neil, M J Booth, and T Wilson. Dynamic wave-front generation for the characterization and testing of optical systems. *Optics letters*, 23(23): 1849–1851, 1998. 4, 30, 31, 76

[45] Abhijit Das and B R Boruah. Optical sectioning microscope with a binary hologram based beam scanning. *Review of Scientific Instruments*, 82(4):043702, 2011. 4, 76

[46] Tobias Haist and Wolfgang Osten. Holography using pixelated spatial light modulators—part 2: applications. *Journal of Micro/Nanolithography, MEMS, and MOEMS*, 14(4):041311, 2015. 4, 76

[47] Minsky Marvin. Microscopy apparatus, December 19 1961. US Patent 3,013,467. 7

[48] Paul Davidovits and M David Egger. Scanning laser microscope. *Nature*, 223 (5208):831–831, 1969. 8

[49] Joseph W Goodman. *Introduction to Fourier optics*. Roberts and Company Publishers, 2005. 9, 26

[50] Max Born and Emil Wolf. Principles of optics. *Pergamon Press*, 6:188, 1980. 9, 50

[51] Tony Wilson and Colin Sheppard. *Theory and practice of scanning optical microscopy*, volume 180. Academic Press London, 1984. 10

[52] GJ Brakenhoff, P Blom, and P Barends. Confocal scanning light microscopy with high aperture immersion lenses. *Journal of Microscopy*, 117(2):219–232, 1979. 10

[53] James B Pawley. *Handbook of biological confocal microscopy*. Springer, 1995. 12

[54] Gábor Steinbach, István Pomozi, Otto Zsiros, Anikó Páy, Gábor V Horváth, and Győző Garab. Imaging fluorescence detected linear dichroism of plant cell walls in laser scanning confocal microscope. *Cytometry Part A*, 73(3):202–208, 2008. 14

[55] Sandra Rocha, Maxim Kogan, Tama´s Beke-Somfai, and Bengt Nordén. Probing microscopic orientation in membranes by linear dichroism. *Langmuir*, 32 (12):2841–2846, 2016. 14

[56] Gábor Steinbach, István Pomozi, Dávid Péter Jánosa, Josef Makovitzky, and Győző Garab. Confocal fluorescence detected linear dichroism imaging of isolated human amyloid fibrils. role of supercoiling. *Journal of fluorescence*, 21(3): 983–989, 2011. 14

[57] Christopher R Carey, Trevor LeBel, David Crisostomo, Jay Giblin, Masaru Kuno, and Gregory V Hartland. Imaging and absolute extinction cross-section measurements of nanorods and nanowires through polarization modulation microscopy. *The Journal of Physical Chemistry C*, 114(38):16029–16036, 2010. 14

[58] David P Biss, Kathleen S Youngworth, and Thomas G Brown. Dark-field imaging with cylindrical-vector beams. *Applied optics*, 45(3):470–479, 2006. 15

[59] Zihao Rong, Cuifang Kuang, Yue Fang, Guangyuan Zhao, Yingke Xu, and Xu Liu. Super-resolution microscopy based on fluorescence emission difference of cylindrical vector beams. *Optics Communications*, 354:71–78, 2015. 15

[60] Yuichi Kozawa and Shunichi Sato. Enhanced detection of longitudinal field of a radially polarized beam in confocal laser microscopy. In *CLEO: Science and Innovations*, pages STh3K–2. Optical Society of America, 2015. 15

[61] Yuichi Kozawa, Daichi Matsunaga, and Shunichi Sato. Superresolution imaging via superoscillation focusing of a radially polarized beam. *Optica*, 5(2):86–92, 2018. 15

[62] Yi Xue, Cuifang Kuang, Shuai Li, Zhaotai Gu, and Xu Liu. Sharper fluorescent super-resolution spot generated by azimuthally polarized beam in sted microscopy. *Optics express*, 20(16):17653–17666, 2012. 15

[63] Robert Goldstein. Pockels cell primer. *Laser Focus*, 34:21, 1968. 16

[64] Masataka Shirasaki. Faraday rotator assembly, September 2 1986. US Patent 4,609,257. 16

[65] Alison Rodger, Bengt Nordén, et al. *Circular dichroism and linear dichroism*, volume 1. Oxford University Press, USA, 1997. 16

[66] Martin J Booth, MAA Neil, and T Wilson. Aberration correction for confocal imaging in refractive-index-mismatched media. *Journal of microscopy*, 192(2): 90–98, 1998. 16

[67] Gavin DM Jeffries, J Scott Edgar, Yiqiong Zhao, J Patrick Shelby, Christine Fong, and Daniel T Chiu. Using polarization-shaped optical vortex traps for single-cell nanosurgery. *Nano letters*, 7(2):415–420, 2007. 17

[68] Redmond P Aylward. Advanced galvanometer-based optical scanner design. *Sensor review*, 23(3):216–222, 2003. 19

[69] Dennis Gabor. A new microscopic principle, 1948. 23

[70] B R Brown and A W Lohmann. Computer-generated binary holograms. *IBM Journal of research and Development*, 13(2):160–168, 1969. 25

[71] Bosanta R Boruah. Dynamic manipulation of a laser beam using a liquid crystal spatial light modulator. *American Journal of Physics*, 77:331, 2009. 25, 31

[72] M A A Neil, T Wilson, and R Juskaitis. A wavefront generator for complex pupil function synthesis and point spread function engineering. *Journal of Microscopy*, 197(3):219–223, 2000. 31

[73] Virendra N Mahajan. Zernike circle polynomials and optical aberrations of systems with circular pupils. *Applied optics*, 33(34):8121–8121, 1994. 33

[74] Robert J Noll. Zernike polynomials and atmospheric turbulence. *JOsA*, 66(3): 207–211, 1976. 33

[75] George B Arfken and Hans J Weber. Mathematical methods for physicists, 1999. 35

[76] Zhen-Yu Rong, Yu-Jing Han, Shu-Zhen Wang, and Cheng-Shan Guo. Generation of arbitrary vector beams with cascaded liquid crystal spatial light modulators. *Optics Express*, 22(2):1636–1644, 2014. 38, 42

[77] Kathleen S Youngworth and Thomas G Brown. Focusing of high numerical aperture cylindrical-vector beams. *Optics Express*, 7(2):77–87, 2000. 41

[78] Ram Oron, Shmuel Blit, Nir Davidson, Asher A Friesem, Zeev Bomzon, and Erez Hasman. The formation of laser beams with pure azimuthal or radial polarization. *Applied Physics Letters*, 77(21):3322–3324, 2000. 42

[79] Steve C Tidwell, Dennis H Ford, and Wayne D Kimura. Generating radially polarized beams interferometrically. *Applied Optics*, 29(15):2234–2239, 1990. 42

[80] M Stalder and M Schadt. Linearly polarized light with axial symmetry generated by liquid-crystal polarization converters. *Optics letters*, 21(23):1948–1950, 1996. 42

[81] Shugo Matsusaka, Yuichi Kozawa, and Shunichi Sato. Micro-hole drilling by tightly focused vector beams. *Optics letters*, 43(7):1542–1545, 2018. 42

[82] Susanne Quabis, Ralf Dorn, and Gerd Leuchs. Generation of a radially polarized doughnut mode of high quality. *Applied Physics B*, 81(5):597–600, 2005. 42

[83] Yuichi Kozawa and Shunichi Sato. Generation of a radially polarized laser beam by use of a conical brewster prism. *Optics Letters*, 30(22):3063–3065, 2005. 42

[84] EG Churin, J Hoβfeld, and T Tschudi. Polarization configurations with singular point formed by computer generated holograms. *Optics communications*, 99(1-2):13–17, 1993. 42

[85] F Kenny, D Lara, OG Rodríguez-Herrera, and C Dainty. Complete polarization and phase control for focus-shaping in high-na microscopy. *Optics express*, 20 (13):14015–14029, 2012. 42

[86] James H Clegg and Mark A A Neil. Double pass, common path method for arbitrary polarization control using a ferroelectric liquid crystal spatial light modulator. *Optics letters*, 38(7):1043–1045, 2013. 42

[87] Xi-Lin Wang, Jianping Ding, Wei-Jiang Ni, Cheng-Shan Guo, and Hui-Tian Wang. Generation of arbitrary vector beams with a spatial light modulator and a common path interferometric arrangement. *Optics letters*, 32(24):3549–3551, 2007. 42

[88] Kun Huang, Peng Shi, GW Cao, Ke Li, XB Zhang, and YP Li. Vector-vortex bessel–gauss beams and their tightly focusing properties. *Optics Letters*, 36(6): 888–890, 2011. 48

[89] Avi Niv, Gabriel Biener, Vladimir Kleiner, and Erez Hasman. Propagation-invariant vectorial bessel beams obtained by use of quantized pancharatnam–berry phase optical elements. *Optics letters*, 29(3):238–240, 2004. 48

[90] Md Gaffar and Bosanta R Boruah. Generation of a boat-shaped beam due to a tightly focused comatically aberrated azimuthally polarized beam. *Journal of Optics*, 16(10):105709, 2014. 49, 52

[91] B Richards and E Wolf. Electromagnetic diffraction in optical systems, ii. structure of the image field in an aplanatic system. *Proceedings of the Royal Society of London. Series A. Mathematical and Physical Sciences*, 253(1274): 358–379, 1959. 54

[92] BR Boruah and MAA Neil. Focal field computation of an arbitrarily polarized beam using fast fourier transforms. *Optics Communications*, 282(24):4660–4667, 2009. 54

[93] Robert M Zucker. Evaluating confocal microscopy system performance. In *Confocal Microscopy*, pages 321–374. Springer, 2014. 72

[94] MW Beijersbergen, RPC Coerwinkel, M Kristensen, and JP Woerdman. Helical-wavefront laser beams produced with a spiral phaseplate. *Optics communications*, 112(5-6):321–327, 1994. 74

[95] Hans Dieter Tholl. Novel laser beam steering techniques. *Proc. SPIE*, 6397: 639708, 2006. 76

[96] Arkadiusz Kuś, Wojciech Krauze, and Małgorzata Kujawińska. Active limited-angle tomographic phase microscope. *Journal of biomedical optics*, 20(11): 111216, 2015. 76

Publications/Achievements/Conferences/Schools

List of Publications

I. **Patents**

(1) **Ranjan Kalita**, S S Goutam Buddha and Bosanta R Boruah, " A system and method for laser beam scanning with periodic switching of polarization of the beam", *Patent Application No.*:**201831006652**, dated 21 Feb 2018, Publication dated 23 Aug 2019.

II. **Journals and Proceedings**

(1) **Ranjan Kalita**, A Saikia, A C Bhuyan and Bosanta R Boruah, " Holographic scanning microscopy for both reflected and fluorescence light imaging", *Rev Sci Instrum*, **90** (10), 106103 (2019).

(2) **Ranjan Kalita**, S S Goutam Buddha and Bosanta R Boruah, "A laser scanning microscope executing intraframe polarization switching of the illumination beam", *Rev Sci Instrum*, **89** (9), 093705 (2018).

(3) **Ranjan Kalita**, S S Goutam Buddha and Bosanta R Boruah, "Laser scanning confocal microscopy using illumination beams with different polarization's in quick succession", *Proc SPIE*, **10772**, 10772I (2018).

(4) **Ranjan Kalita**, S S Goutam Buddha and Bosanta R Boruah, "Suitability of holographic beam scanning in high resolution applications", *Proc SPIE*, **10499**, 104991P (2018).

(5) **Ranjan Kalita** and Bosanta R Boruah, "Confocal imaging with orthogonally polarized illumination beams", *Proc SPIE*, **9713**, 971316 (2016).

(6) **Ranjan Kalita**, Md Gaffar and Bosanta R Boruah, " The generation of arbitrary vector beams using a division of a wavefront-based setup", *J Opt*, **18** (7), 075604 (2016).

III. **Other relevant publications (Not directly related to the thesis)**

(1) S S Goutam Buddha, **Ranjan Kalita** and Bosanta R Boruah, "Array detection in a holographic scanning microscope", *Opt Commun*, **462**, 125339 (2020).

(2) **Ranjan Kalita** and Bosanta R Boruah, "Effect of aberration on the electric field orientation around the focus of a polarized light beam", *Proc SPIE*, **10772**, 10772Y (2018).

(3) S S Goutam Buddha, **Ranjan Kalita** and Bosanta R Boruah, "Estimation of point spread function of an imaging system using a programmable target", *Proc SPIE*, **10499**, 104991O (2018).

(4) Md Gaffar, **Ranjan Kalita** and Bosanta R Boruah, "Experimental observation of the aberration effects on a radially polarized beam", *JOSA A*, **33** (11), 2178 - 2187 (2016).

(5) Md Gaffar, **Ranjan Kalita** and Bosanta R Boruah, "Experimental demonstration of a light beam with superior aberration resilience", *Opt Lett*, **41** (19), 4425 - 4428 (2016).

Academic achievements

(1) Awarded SPIE Student Travel Grant to attend SPIE Optics + Photonics - 2018, held at San Diego, California, USA. (August 19 - 23, 2018)

(2) Received International Travel Support from SERB, DST, Govt. of India to attend SPIE Optics + Photonics - 2018, held at San Diego, California, USA. (August 19 - 23, 2018)

(3) Presented the second prize in the poster presentation at the Research Conclave'18, organized by Students' Academic Board, IIT Guwahati. (March 8 - 11, 2018)

(4) Certificate of merit in the poster competition organized by IIT Patna OSA Student Chapter (during the DST-SERB School on "Modern Optics & Its Applications") held at the Department of Physics, IIT Patna. (December 16, 2015)

(5) Presented best poster award (3rd position, IITG category) in the TEQIP Symposium to celebrate the 2015 International Year of Light held at the Department of Physics, IIT Guwahati. (October 31, 2015)

Conference Presentation

(1) "Laser scanning confocal microscopy using illumination beams with different polarization's in quick succession", SPIE Optical Engineering + Applications, San Diego, California, USA, August 19 - 23, 2018.

(2) "Effect of aberration on the electric field orientation around the focus of a polarized light beam", SPIE Optical Engineering + Applications, San Diego, California, USA, August 19 - 23, 2018.

(3) "Development of a standalone confocal imaging system with CGH based as well as galvanometer scanner based beam scanning mechanism", Research Conclave - 2018, Indian Institute of Technology Guwahati, Assam, India, March 08 - 11, 2018.

(4) "Spatially varying aberration corretion in a beam scanning confocal microscope", International conference on advances in optics and photonics (ICAOP – 2017), Hisar, Harayana, India, November 23 - 26, 2017.

(5) "Confocal microscopy and its applications", Research Conclave – 2017, Indian Institute of Technology Guwahati, Assam, India, March 17 - 19, 2017.

(6) "Confocal imaging with pixel based aberration correction of the illumination beam", International conference on light and light based technologies (ICLLT – 2016)", Tezpur University, Assam, India, November 26 - 28, 2016.

(7) "Imaging linear dichroism in a laser scanning confocal microscope", Research Conclave – 2016, Indian Institute of Technology Guwahati, Assam, India, March 18 - 20, 2016.

(8) "Generation of boat-shaped beam using an arbitrary vector beam forming setup", TEQIP symposium to celebrate the 2015 International Year of Light (IYL – 2015), Indian Institute of Technology Guwahati, Assam, India, October 31, 2015.

(9) "Optical sectioning microscopy using binary multiplex hologram based beam scanning", International conference in optics and photonics (ICOP – 2015), University of Calcutta, West Bengal, India, February 20 - 22, 2015.

School/Workshop attended

(1) "One-Day workshop on vacuum technology and its application in optical Science" Indian Institute of Technology Guwahati, Assam, India, August 19, 2017.

(2) "Advanced microscopy and imaging techniques" Indian Institute of Technology Guwahati, Assam, India, April 18 - 20, 2017.

(3) "3rd IEEE workshop on Advanced MATLAB Applications – ADMAT 2016" Indian Institute of Technology Guwahati, Assam, India, October 01 - 02, 2016.

(4) DST-SERB School on "Modern Optics & Its Applications", Indian Institute of Technology Patna, Bihar, India, November 30 - December 18, 2015.

(5) Presented a paper "A scheme to record 3-dimensional intensity distribution around the focus of a lens under low NA focusing condition", in "South Asian Workshop on Optics & Photonics (SAWOP – 2015)", Indian Institute of Technology Guwahati, Assam, India, November 17 - 18, 2015.

* * *